Copyright Warning & Restrictions

The copyright law of the United States (Title 17, United States Code) governs the making of photocopies or other reproductions of copyrighted material.

Under certain conditions specified in the law, libraries and archives are authorized to furnish a photocopy or other reproduction. One of these specified conditions is that the photocopy or reproduction is not to be "used for any purpose other than private study, scholarship, or research." If a, user makes a request for, or later uses, a photocopy or reproduction for purposes in excess of "fair use" that user may be liable for copyright infringement,

This institution reserves the right to refuse to accept a copying order if, in its judgment, fulfillment of the order would involve violation of copyright law.

Please Note: The author retains the copyright while the New Jersey Institute of Technology reserves the right to distribute this thesis or dissertation

Printing note: If you do not wish to print this page, then select "Pages from: first page # to: last page #" on the print dialog screen

NJIT New Jersey's Science & Technology University

The Van Houten library has removed some of the personal information and all signatures from the approval page and biographical sketches of theses and dissertations in order to protect the identity of NJIT graduates and faculty.

ABSTRACT

TERAHERTZ WIRELESS COMMUNICATION THROUGH ATMOSPHERIC TURBULENCE AND RAIN

by
Jianjun Ma

This dissertation focusses on terahertz (THz) wireless communication technology in different weather conditions. The performance of the communication links is mainly studied under propagation through atmospheric turbulence and rain. However, as real outdoor weather conditions are temporally and spatially varying, it is difficult to obtain reproducible atmospheric conditions to verify results of independent measurements making it a challenge to measure and analyze the impact of outdoor atmospheric weather on communication links. Consequently, dedicated indoor weather chambers are designed to produce controllable weather conditions to emulate the real outdoor weather as closely as possible. To emulate turbulent air conditions, an enclosed chamber is developed into which air with controllable airspeeds and temperatures are introduced to generate a variety of atmospheric turbulence for beam propagation. To emulate varying rain conditions, an enclosed chamber is built in which pressurized air forces drops of water through an array of 30 gauge needles.

In order to study and compare propagation features of THz links with infrared (IR) links under identical weather conditions, a THz and IR communications lab setup with a maximum data rate of 2.5 Gb/s at 625 GHz carrier frequency and 1.5 μm wavelength, are developed. A usual non return-to-zero (NRZ) format is applied to modulate the IR channel but a duobinary coding technique is used for driving the multiplier chain-based 625 GHz source, which enables signaling at high data rate and higher output power. The

power and bit-error rate (BER) on the receiver side are measured, which can be used to analyze the signal performance. To analyze the phase change in the turbulence chamber due to the refractive index change induced by turbulence, a Mach-Zehnder Interferometer with He-Ne laser at 632.8nm is developed.

In the same weather conditions, the impact on THz in comparison with IR link is not equivalent due to the spectral dependence on atmospheric turbulence and rain. In the experiment, after THz (625 GHz) and IR (1.5 μm) beams propagate through the same condition, performance of both channels is analyzed and compared. Kolmogrov theory is employed to simulate the atmospheric turbulence which leads to attenuation of THz and IR signals. Mie scattering theory is employed to simulate the attenuation of THz and IR beams due to rain.

Under identical turbulence conditions, THz links are superior to IR links. However, the performance of THz and IR links are comparable under identical rain conditions.

TERAHERTZ WIRELESS COMMUNICATION THROUGH ATMOSPHERIC TURBULENCE AND RAIN

by
Jianjun Ma

A Dissertation
Submitted to the Faculty of
New Jersey Institute of Technology and
Rutgers, The State University of New Jersey-Newark,
in Partial Fulfillment of the Requirements for the Degree of
Doctor of Philosophy in Applied Physics

Department of Physics

January 2016

Copyright © 2016 by Jianjun Ma

ALL RIGHTS RESERVED

.

APPROVAL PAGE

TERAHERTZ WIRELESS COMMUNICATION THROUGH ATMOSPHERIC TURBULENCE AND RAIN

Jianjun Ma

Dr. John F. Federici, Dissertation Advisor — Date
Distinguished Professor of Physics, NJIT

Dr. Lothar Moeller, Committee Member — Date
Principal Engineer, TE Connectivity, Eatontown, NJ

Dr. Tao Zhou, Committee Member — Date
Associate Professor of Physics, NJIT

Dr. Andrei Sirenko, Committee Member — Date
Professor of Physics, NJIT

Dr. Zhen Wu, Committee Member — Date
Professor of Physics, Rutgers University, Newark, NJ

BIOGRAPHICAL SKETCH

Author: Jianjun Ma

Degree: Doctor of Philosophy

Date: January 2016

Undergraduate and Graduate Education:

- Doctor of Philosophy in Applied Physics,
  New Jersey Institute of Technology, Newark, NJ, 2016

- Master of Engineering in Electrical Engineering,
  Shandong University of Science and Technology, Qingdao, P. R. China, 2012

- Bachelor of Science in Physics,
  Weifang University, Weifang, P. R. China, 2008

Major: Applied Physics

Presentations and Publications:

J. Ma, F. Vorrius, L. Lamb, *et al.* "Comparison of Experimental and Theoretical Determined Terahertz Attenuation in Controlled Rain." *Journal of Infrared, Millimeter, and Terahertz Waves* 36, no. 12 (2015): 1195-1202.

J. Ma, F. Vorrius, L. Lamb, *et al.* "Experimental Comparison of Terahertz and Infrared Signaling in Laboratory-Controlled Rain." *Journal of Infrared, Millimeter, and Terahertz Waves* 36, no. 9 (2015): 856-865.

J. Ma, L. Moeller, J. F. Federici. "Experimental comparison of terahertz and infrared signaling in controlled atmospheric turbulence." *Journal of Infrared, Millimeter, and Terahertz Waves* 36, no. 2 (2015): 130-143.

J. F. Federici, J. Ma, L. Moeller. "Weather Impact on Outdoor Terahertz Wireless Links." *2nd ACM International Conference on Nanoscale Computing and Communication* (2015).

J. Ma, L. Moeller, J. F. Federici. "Terahertz performance in atmospheric turbulence." *39th International Conference on Infrared, Millimeter, and Terahertz waves* (2014).

J. F. Federici, J. Ma. “Comparison of terahertz versus infrared free-space communications under identical weather conditions.” *39th International Conference on Infrared, Millimeter, and Terahertz waves* (2014).

D. Li, J. Ma, W. Zhou, *et al*. “Terahertz pulse manipulation based on difference frequency generation.” *Terahertz Science and Technology* 7, no. 3 (2014): 128-138.

D. Li, J. Ma, W. Zhou, *et al*. “Phase matching condition of THz pulse shaping in difference frequency mixing.” *6th UK, Europe, China Millimeter Waves and THz Technology Workshop* (2013).

To my beloved family members

谨献给我亲爱的家人

ACKNOWLEDGMENT

First and foremost, I would like to thank my dissertation advisor, Dr. John F. Federici, for his inspiring guidance, valuable suggestions in my research and his constant support during my study here. Without his stimulating and engaging discussions and feedback, which gave me many valuable experimental and theoretical ideas, this research work could not have been completed.

My special appreciation is given to Dr. Lothar Moeller at TE Connectivity for his patience, valuable ideas, insightful suggestions and comments both in my PhD study and research. I am proud of the work we did together and believe all of the training and help will always inspire me in my future career.

I would also thank Dr. Andrei Sirenko, Dr. Tao Zhou, and Dr. Zhen Wu for serving of my dissertation committee.

It is my pleasure to thank my lab mates, Ke Su, Francis Vorrius, Lucas Lamb, and Carley Nicoletti in NJIT for their selfless help.

This research is supported by the National Science Foundation under Grant No. ECCS-1102222.

Finally, I wish to give the utmost appreciation to my beloved family members for their understanding, support and encouragement when pursuing my doctoral degree.

TABLE OF CONTENTS

(Continued)

(Continued)

(Continued)

LIST OF TABLES

LIST OF FIGURES

(Continued)

(Continued)

(Continued)

Figure **Page**

(Continued)

Figure **Page**

LIST OF SYMBOLS

©	Copyright
E_p	Photon energy
N	Photon frequency
H	Planck constant
A	Geometrical cross-section area
R	Radius of a spherical particle
P_a	Absorbed power
P_s	Scattered power
S_i	Incident power density
Q_a	Absorption cross section
Q_s	Scattering cross section
Q_e	Extinction cross section
ξ_a	Absorption efficiency
ξ_s	Scattering efficiency
ξ_e	Extinction efficiency
X	Normalized circumference
N	Relative index of refraction
λ_b	Wavelengths in background medium
λ_0	Wavelengths in vacuum
$\varepsilon_b^{'}$	Real part of relative dielectric constant

(Continued)

n_p	Complex indices of refraction of particle
n_b	Complex indices of refraction of background medium
ε_p	Complex dielectric constants of particle
ε_b	Complex dielectric constants of background medium
a_l, b_l	Mie coefficients
ϕ_0	Initial phase delay
K	Wavenumber
s_1, s_2	Path length
Δ	Path difference
Δn	Refractive index difference
L	Chamber length
C_v^2	Velocity structure constant
D_v	Longitudinal structure function of wind velocity
v_i , v_j	Velocity components at point i and j
C_T^2	Temperature structure constant
T_i , T_j	Temperature at point i and j

(Continued)

$\bar{E}(\mathbf{r})$	Electric field of a monochromatic wave
$n(\mathbf{r})$	Random refractive index
$E_0(\mathbf{r})$	Unperturbed incident field
$\chi(\mathbf{r})$	Log-amplitude fluctuation in Gaussian distribution
$\delta(\mathbf{r})$	Log-phase fluctuation Gaussian distribution
$p_\chi(\chi)$	Gaussian distribution of $\chi(\mathbf{r})$
$E[\chi]$	Mean of the log-amplitude
σ_χ^2	Log-amplitude variance
σ_R^2	Rytov variance
C_n^2	Refractive index structure parameter
R_F	Fresnel zone
ρ_0	Coherence radius of the light
α , β	Effective number of large and small scale cells
$\Gamma(\cdot)$	Gamma function
$K_{\alpha-\beta}(\cdot)$	Modified Bessel function of the 2nd order of $\alpha-\beta$
D	Receiving lens aperture diameter

(Continued)

$f_K(I)$	Distribution function for K-distributed model
$f_{NE}(I)$	Distribution function for negative exponential model
n_{mmW}	Refractive index of air in the millimeter wave band
n_{IR}	Refractive index of air in the IR wave band
C_T^2	Temperature structure function
σ_I^2	Scintillation index
W_0	Beam radius
W_e	Effective long-term averaged beam radius in free space
Λ	Fresnel ratio of beam
$N(D)$	Number density of raindrops of diameter D in a unit volume
R	Rain rate
N_t	Total raindrop number in a unit volume
σ	Standard geometric deviation
$\bar{D}$	Geometric mean diameter
$v(D)$	Rain fall velocity

(Continued)

ε_0	Permittivity of free space
$\tau_{W1},\ \tau_{W2}$	Relaxation time constant
ϕ_N	Poisson distribution function

LIST OF DEFINITIONS

Absorption	The energy of a laser beam is transformed into internal energy of absorbers.
Scattering	The radiation is deviated from its previous trajectory by scatters due to their interactions.
Scintillation	The phase front of the laser beam is distorted due to the variation of the index of refraction, thus leading to the irradiation fluctuation or scintillation.
Aperture averaging	The receiver can average fluctuations of the received waveform over the aperture area, leading to reduced signal fluctuations.
Beam spreading	The laser beam if spread by diffraction in the propagation path, thus resulting in the beam spreading.
Bit error ratio	The number of bit errors divided by the total number of transferred bits during a studied time interval

CHAPTER 1

INTRODUCTION

Next Ray? T-Rays!

X.-C. Zhang

The THz spectrum region, consists of electromagnetic waves within the ITU (International Telecommunication Union)-designated band of frequencies from 0.3 THz (wavelength 1 mm) to 10 THz (wavelength 30μm), is located in the gap between millimeter waves and the infrared as shown in Figure 1.1. The THz region, bridges the gap between the electronics and photonics response, has seen rapid progress by adapting the techniques from both neighboring fields. However, neither optical nor electronics device could fully meet the application requirements because of the unavailability of convenient and inexpensive sources, sensitive detectors, and fast speed modulators.

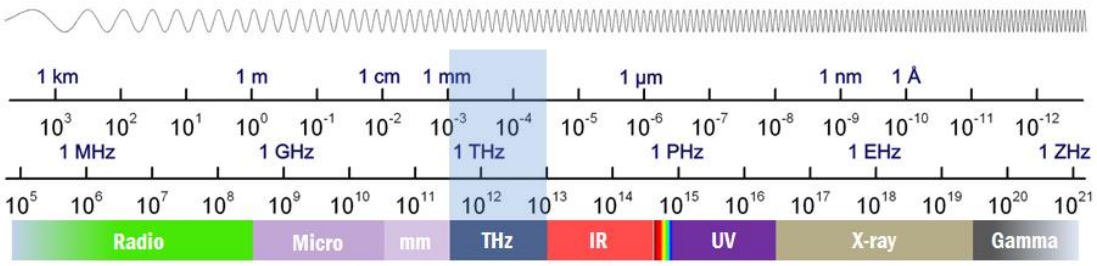

Figure 1.1 The electromagnetic spectrum. Micro: Microwave, mm: millimeter wave, IR: infrared, UV: ultraviolet.
Source: [1]

Over the past two decades, the field of science and technology has been significantly changed and revolutionized in THz region due to so many new advances for THz generators and detectors [2, 3, 4]. Many applications can be benefit from THz

systems, ranging from medicine and biology [5, 6], testing and sensing [7, 8], security [9, 10, 11], to next generation wireless communication systems.

In this chapter, a brief introduction to Terahertz spectrum and technology is presented from its comparison with millimeter and infrared waves. Motivation, objectives, and organization of the research are also presented.

1.1 Research Motivation

Over the past three decades, wireless data rates have doubled every 18 months and will quickly reach the capacity of wired communication systems [12]. So it is obvious that the data rates around 100 Gb/s will be achieved in 2020 from Edholm's Law [13]. Following this trend, communication links in THz region, envisioned as a key wireless technology to satisfy this high demand, are expected to come in the near future [14-20]. THz links owns inherently larger accessible bandwidth compared to millimeter waves [21], which will alleviate the spectrum scarcity and capacity limitations of current wireless systems. For example, during the 2008 Olympic Games in Beijing, Osaka University and NTT Corp. deployed a 120 GHz data link with 10Gb/s to transmit uncompressed high-definition (HD) images of the game stadiums over a distance of 1 km from the International Broadcasting Center to the Beijing Media Center [22], and now they are trying to move to a 100Gb/s data rate by 2020 which will allow the download of 3 HD movies in one second by a smartphone user [23].

Why is THz wireless communication so urgently needed? That is because it owns many advantages over its counterparts - millimeter wave and infrared waves. Compared to millimeter wave (30 GHz – 300 GHz) systems, THz wireless communication links present:

(1) Unregulated frequencies: Frequencies above 300 GHz are currently unallocated by the Federal communications Commission (FCC) as shown in the U.S. Frequency Allocation chart in [24, 25].

(2) Ultra-high bandwidth: THz spectrum, ranging from 0.3THz to 10THz, can be divided into many narrower communication bands [16]. Besides, THz spectrum bandwidth is 1000 times as wide as the total bandwidth of long wave (LW), medium wave (MW), short wave (SW) and microwave (30GHz). So this determines that THz communications have the potential for increased bandwidth capacity.

(3) High security: THz communication can be implemented as a "secure" short range communication link [16]. THz spectrum suffers very high attenuation from the vapor in the atmosphere, so it is opaque to atmosphere, which makes it only suitable for short range communication. Besides, THz can support ultrahigh bandwidth spread spectrum systems, which can enable secure communication, large capacity networks, and protection against channel jamming attacks. For an example, if one do not know the exact spectrum band used in communication, it is difficult to steal the signal from such a wideband spectrum, which makes it a secure communication method.

(4) Directional beam: THz communications are inherently more directional at the same transmitter aperture than millimeter (MMW) links since THz waves have less free-space diffraction due to its shorter wavelength. Such small antennas with good directivity can be used in THz communications, which can reduce the transmitted power and signal interference of different antennas.

Compared to infrared frequencies (300 GHz – 430 THz), THz also owns some advantages:

(1) Lower attenuation of THz radiation compared to IR under certain weather conditions (e.g., fog, dust, and air turbulence).

(2) Scintillation effects of THz radiation are significant smaller than IR radiation due to its significant longer wavelength, which leads to smaller signal power fluctuations in THz receiver side, and then allows THz to provide longer links compared to wireless IR link.

(3) Intensity modulation and detection with IR photo detectors is not as sensitive as THz heterodyne detectors.

(4) There is more ambient IR light noise typically present compared to ambient THz noise. In many indoor and outdoor environments, there are intense ambient infrared noise induced by sunlight, incandescent lighting and fluorescent lighting.

(5) There is an eye safety concerns with IR wavelengths requiring that IR transmitted power be limited to eye-safe emission power levels, however, THz is safe for human health.

Based on all these advantages, it is the right time now to prepare for the future of this THz communication technique. Recently, IEEE 802.15 Wireless Personal Area Networks (WPAN) Study Group 100 Gbit/s Wireless (SG100G) has been established to work towards the first standard for THz communication links and various proposals have been made [26].

However, performance of the THz wireless channel suffers abrupt degradation in the atmosphere when propagates in outdoor. Therefore, it is desirable to experimentally characterize and simulate different weather conditions such as humidity, rain, fog, dust, and turbulence, and analyze the communication performance under these weathers. Many experiments have been done to investigate the impact of different weather conditions on the THz communication link.

Attenuation due to water vapor from 0.2-2 THz was characterized by Grischkowsky's group using THz time domain spectroscopy and they found higher attenuation in these THz transmission windows than previously demonstrations (Yang, 2011) [27, 28]. They confirmed 4 THz transparent windows at 0.41 THz, 0.46 THz, 0.68 THz and 0.85 THz [29].

Broadband THz pulse propagation through dense fog was presented by them also and the experimental results agree well with the predicted attenuation due to fog [30, 31]. This further confirms that the broadband THz waves can be a promising illumination source for many applications in fog.

Recently, they measured THz pulse and corresponding spectra up to 1 THz under the atmospheric weather conditions of rain, clouds and snow between two buildings [32]. In the rain measurements, a larger attenuation was observed compared with theoretical

prediction.

The effect of scintillations due to wind effects on a propagating 125 GHz data signal was investigated by Yamaguchi's group [33]. Power attenuation due to rain for 120 GHz and 355.2 GHz communication links was presented by Hirata and Ishii respectively [34, 35]. However, it is still a challenge to measure the effect of the weather conditions on THz wireless links due to required long observation times and the difficulty to obtain some reoccurrence of similar atmospheric conditions to verify results of independent measurements.

In this research work, the experimental results of THz attenuation due to atmospheric turbulence and rain from weak to strong strengths are reported. Weather emulating chambers are designed and demonstrated to emulate and control the turbulence and rain strength and to determine the equivalence between the outdoor and laboratory communication links. One method is employed to measure and track the phase fluctuation caused by the scintillation effect. The effect of weather conditions on THz communication links is experimentally investigated and evaluated. The experimental results are compared with IR signal performance under the same weather conditions as a comparison of two competing technologies for high data rate wireless communication links. Theoretical models for atmospheric turbulence and rain weather conditions are proposed to characterize the degradation of both links and used to predict its outdoor performance.

1.2 Research Objectives

The prime objective of this dissertation is to experimentally characterize and investigate atmospheric weather conditions, mainly atmospheric turbulence and rain, on the

performance of a THz communication link. It is very difficult to measure the effect of the weather conditions due to required long observation times and the difficulty to obtain some reoccurrence of similar atmospheric conditions. So, laboratory chambers are designed to emulate and analyze the performance of THz communication links in different weather conditions. Such laboratory chambers can realize the controllable effects of weather effects on the THz channels. Some wavelength dependent models for attenuation prediction in atmospheric turbulence and rain channel are conducted, which are checked based on our measurements.

1.3 Dissertation Organization

The dissertation has been organized as follows:

Chapter 1 - Introduction: A brief introduction of Terahertz spectrum is given. Research motivations and objectives of this dissertation are presented also.

Chapter 2 - Terahertz and Infrared Wireless Communication Systems: A complete review of THz wireless communication technology above 300GHz is presented. Fundamentals of IR wireless communication technology are briefly summarized. The main degradation effects of THz and IR channels due to outdoor weather conditions are introduced, and the present studies of these effects are shown briefly.

Chapter 3 - Experimental Setup of Wireless Communication Channels: The detailed description of the setup of THz and IR communication channels is presented, with duobinary modulation technique used. The method of phase change measurement by Mach-Zehnder Interferometer is explained.

Chapter 4 - Atmospheric Turbulence Theories: Atmospheric turbulence in introduced briefly in this chapter. Many theoretical models for the characterization of atmospheric

turbulence are shown and compared. The effect of aperture averaging is explained also.

Chapter 5 - Rain Theories: A brief introduction of rain is given. The present studies of rain drop size distribution are summarized. Theory of attenuation from rain caused by absorption and scattering is shown, with Double-debye model employed for computing of the dielectric constant of water.

Chapter 6 - Experimental and Theoretical Results in Atmospheric Turbulence: Experimental characterization and theoretical modeling of the atmospheric turbulence effect on THz and IR wireless links are reported under different and controlled turbulence conditions. The design of atmospheric turbulence chamber is detailed here. Scintillation effect on the signal performance caused by turbulence is confirmed in this chapter by designing a measurement method.

Chapter 7 - Experimental and Theoretical Results in Rain: A rain chamber which can generate the rain with different rain rates is detailed. A THz time domain spectrum system (THz-TDS) is introduced in this chapter to study the attenuation spectrum of THz wave due to rain. And the rain drop distribution from the rain chamber is measured and presented. Theoretical attenuation due to rain is calculated by using Mie scattering model, and is compared with the experimental measurements under different rain rates.

Chapter 8 - Conclusion and Future Work: All the results of the research are summarized and presented in this chapter. Future work is outlined.

CHAPTER 2

TERAHERTZ AND INFRARED WIRELESS COMMUNICATION SYSTEMS

THz communications exhibit many advantages as introduced in Chapter 1, such as high transmission rate, high security, better directionality, low scattering and good penetrability, that it has seen rapid progress over the past few years and many kinds of communication systems have been investigated. Besides, the spectrum beyond 300 GHz has not been allocated to any other radio service, so it is a feasible and prosperous candidate for future wireless communication.

2.1 Fundamentals of Terahertz (THz) Communication Systems

At present, there are three kinds of approaches employed for THz transmitter and two methods for THz receiver:

(1) Electronics based transmitter: The THz transmitter is comprised of an RF signal generator, a data modulator and a post-amplifier [36]. The generated THz signal is usually synthesized by millimeter wave generator at 30 - 100 GHz or by multiplying the amplified output of a Gunn diode oscillator. Integrated-circuit (IC) oscillators, such as resonant tunneling diode (RTD) [37], have attracted a lot attention as a new promising THz generator.

(2) Photonics based transmitter: The THz generation and modulation are realized by using photonic techniques [38-43]. For example, THz signal can be converted from two far-infrared lasers by employing optical heterodyne technique and uni-traveling-carrier photo-detector (UTC-PD) and then emitted by antennas. Such method is mainly based on 1.55um telecom components, such as Er-doped fiber amplifiers (EDFAs), optical fibers and semiconductor laser amplifiers (SOAs).

(3) THz lasers based transmitter: Quantum cascade lasers (QCLs), as a kinds of THz lasers, can generated THz signals above 1THz and realized direct modulation for frequencies above 10 GHz [43-46].

(4) Electronics based direct detection: It can be easily realized by employing commercially available Schottky barrier diodes (SBD) with a cut-off frequency of 1-10THz [36, 38-41, 42, 43].

(5) Electronics based heterodyne detection: It is more complex and sensitive than direct detection, and can detect frequency modulation and phase modulation [48, 49].

The recent developments of ultrahigh-speed wireless communication links using carrier frequencies of over 300 GHz are reviewed as shown in Table 2.1. Wireless links with data rate above 100Gb/s has been analyzed and predicted by Tadao Nagatsuma's group and Leif K. Oxenløwe's group recently [39, 50, 51].

Table 2.1 Summary of THz Communication Links over 300 GHz. UTC-PD stands for Uni-traveling carrier photodetector. SBD: Schottky barrier detector; QWP: quantum well photo-detector; HEB: hot electron bolometer; RTD: resonant tunneling diode detector.

Carrier Frequency	Transceiver		Distance	Modulation rate or bandwidth	Reference
	Transmitter	Receiver			
0.1-3 THz	THz TDS		48 cm	6 kHz	[52]
1 THz	THz TDS		1 m	1 MHz	[39]
237.5 GHz					
300 GHz	Discrete Component	Discrete Component	52 m	96 Mb/s	[48]
	RTD	Discrete Component	0.3 m	1.5 Gb/s	[49]
	UTC-PD	SBD	0.5 m	12.5 Gb/s	[43]
	UTC-PD	SBD	0.5 m	24 Gb/s	[41]
	Discrete Component	Discrete Component	10 m	30 Gb/s	[29]
	UTC-PD	SBD	0.5~1m	50 Gb/s	[38-40]
300-400GHz	UTC-PD	SBD	0.5m	1 Gb/s	[42]
542 GHz	RTD	SBD	1 cm	2 Gb/s	[36]
625 GHz	Discrete Component	Schottky Diode	3 m	2.5 Gb/s	[54]
2.5 THz	THz QCL	HEB	3 m	1 MHz	[46]
3.8 THz	THz-QCL	THz QWP	2 m	500 Hz	[45]
4.1 THz	THz-QCL	THz QWP	2 m	580 Hz	[47]

2.1.1 24 Gb/s THz Wireless Communication Link at 300 GHz

NTT Corporation demonstrated a 300 GHz wireless communication system as shown in

Figure 2.1 [41], which uses a UTC-PD (Uni-traveling carrier photodetector) as transmitter and a SBD (Schottky barrier detector) as receiver. In the transmitter side, photonic technologies are employed for generating and modulating the terahertz waves by using an EOM (electro-optic intensity modulator) and the UTC-PD. The THz waves were radiated via a 25 dBi horn antenna. In the receiver side, the transmitted signal was received with the SBD, which was integrated with a planar antenna on InP substrate and assembled with a high resistivity silicon lens, and amplified with a LNA (low-noise amplifier). For 200μW output power and 9.5mA output current for the UTC-PD, an ASK (Amplitude-shift keying) signal with 24 Gb/s data rate was successfully transmitted over a distance of 50 cm with 2×10^{-9} BER (bit error rate).

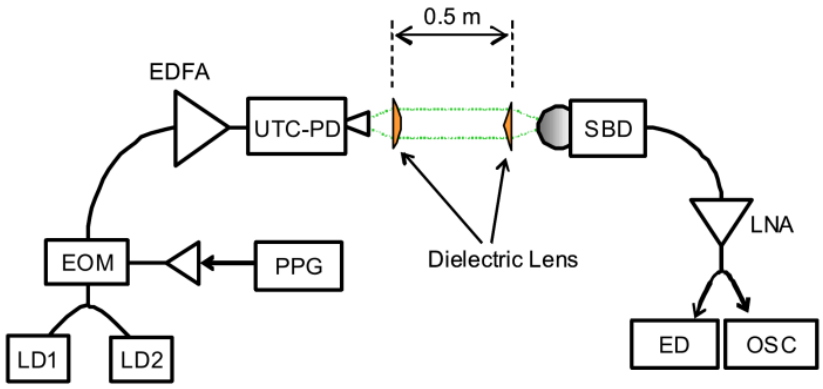

Figure 2.1 Experiment setup of 24 Gb/s THz Wireless Communication Link at 300 GHz. LD: laser diode, EOM: Electro-optic modulator, PPG: pulse pattern generator EDFA: Erbium doped fiber amplifier, UTC-PD: Uni-travelling photodiode, SBD: Schottky barrier diode, LNA: low noise amplifier, ED: error detector, OSC: Oscilloscope.
Source: [41]

2.1.2 300 GHz Video Signal Transmission System

C. Jastrow's group from Germany realize a video signal transmitting over 22m distance by using a versatile 300 GHz transmission system with a bandwidth of up to 10 GHz in 2008 [55]. In their system, autarkic transmitter and receiver units were employed. In 2010,

they modified their system, which consists of autarkic transmitter and receiver units based on Schottky mixers and Metal waveguide technology as shown in Figure 2.2, to transmit a 96 Mb/s Digital Video Broadcasting - Satellite (DVB-S2) signal over a distance of 52 m [48]. The local oscillator is provided by a 16.66 GHz phase-locked dielectric resonator oscillator (DPRO with 10 MHz reference crystal oscillator), which is first amplified and tripled two times. Then sub-harmonic mixer is used to up-convert the 150 GHz signal (DC - 10 GHz, delivered by a signal generator) to 300 GHz, which is radiated from a horn antenna directly attached to the mixer block with 300 GHz carrier and 50μW power. To suppress noise, the receiver and transmitter are identical in construction aside from different frequencies used as input to the local oscillator chains. In the system 16.40 GHz at the transmitter against 16.38 GHz at the receiver results in an intermediate frequency of 360 MHz at the receiver output of the super-heterodyne system.

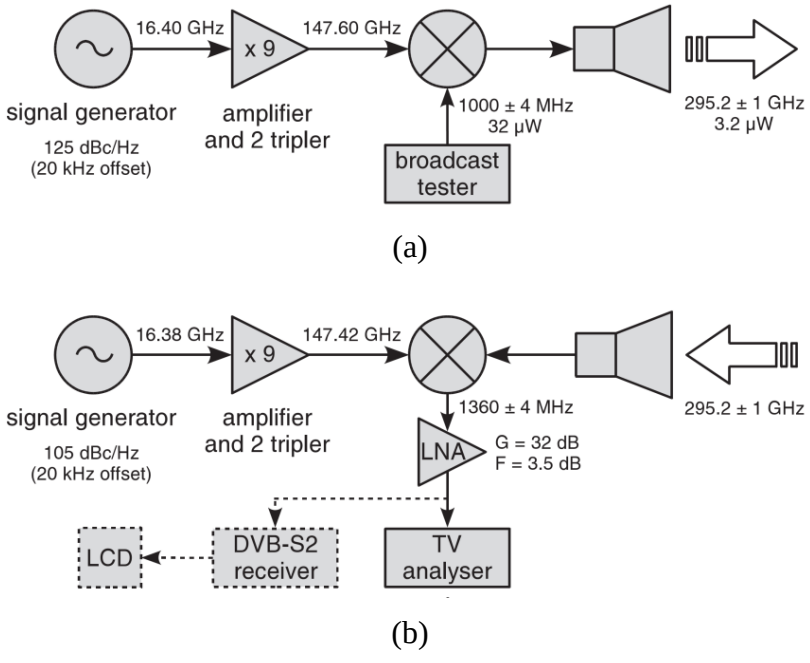

Figure 2.2 Block diagram of digital transmission setup. LNA stands for low noise amplifier.
Source: [48]

2.1.3 542 GHz Digital Signal Transmission System Based on RTD

K. Ishigaki's group demonstrated a terahertz wireless data transmission system by using the RTD (resonant tunneling diode) oscillator integrated with a slot antenna as transmitter and SBD with a horn antenna as receiver as shown in Figure 2.3 [36]. A modulation signal of -30dBm was superimposed with DC bias by a bias tee to realize amplitude modulation. At the receiver side, a bias tee was also used for the DC bias supply of SBD to detect THz wave. Eye pattern and BER of up to 3.25 Gbit/s were measured in their research. The measured BERs were 2×10^{-8} and 3×10^{-5} for 2 and 3 Gbit/s, respectively. The RTD oscillates at 542 GHz with a cutoff frequency of 1.1 GHz. Due to the low output power of 210μW from RTD and the received output power of the SBD around 10μW, the transmission distance was only ~1 cm.

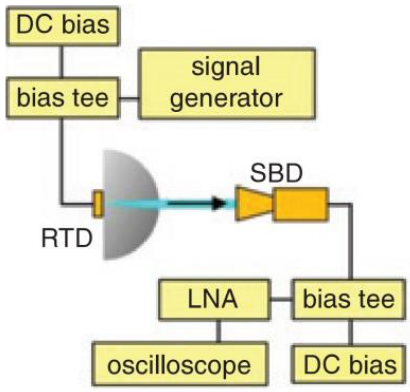

Figure 2.3 Block diagram of 542GHz transmission system. LNA stands for low noise amplifier. SBD: Schottky barrier detector; RTD: resonant tunneling diode detector.
Source: [36]

2.1.4 THz Wireless Communication Link Based on QCL

Liu's group in Canada introduced a QCL (quantum cascade laser) THz free space

communication system based on a 3.8 THz QCL laser and a cryogenically cooled (12K) QWP (quantum well photodetector) as shown in Figure 2.4 [45]. A QCL housed in a vacuum Dewar radiates THz frequency, which is first collected and collimated by a parabolic mirror labeled M1 and then reflected by M2, and finally coupled through the semi-insulating substrate to the mesa at 45 ° angle as is done in quantum well infrared photodetector (QWIP).

At the transmitter side, a pulse series with 8ns pulse width at a repetition rate of 455 kHz were generated by a custom-made pulse generator with maximum voltage of 17V, is modulated by an audio frequency and then used to modulate the QCL electronically. At the receiver side, the electronic output of the QWP is first amplified and then filtered by a 10 kHz low pass filter. Finally, the signal is coupled onto the antenna of AM radio and recovered to the original audio signal.

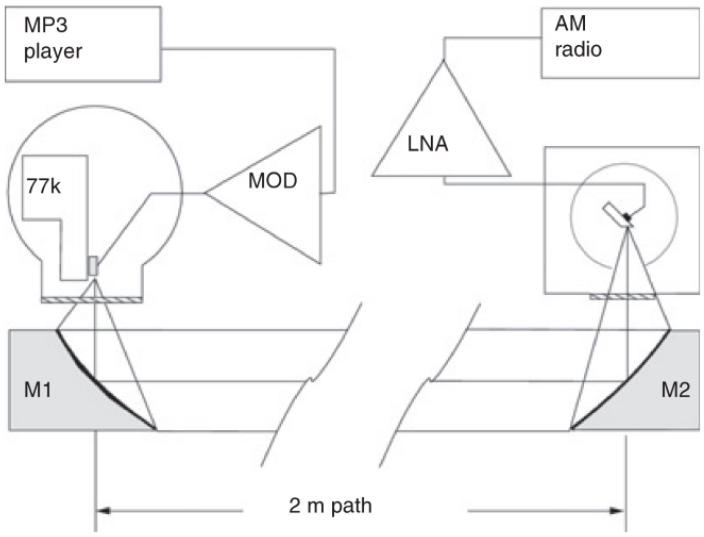

Figure 2.4 Schematic of link showing quantum cascade laser at left and quantum well photodetector [45]. LNA stands for Low-Noise Amplifier.
Source: [45]

In 2010, Cao's group in China reported a wireless THz link using a QCL operates in CW mode as the transmitter, a QWP as the receiver, employed a directly voltage modulation scheme as shown in Figure2.5 [47]. They transmitted audio signals through the link over a distance of 2m with 580 kHz bandwidth and 4.1 THz carrier frequency. In 2012, they optimized the THZ QCL drive circuit and realize a transmission distance of 2.4m with 5 Mb/s date rate.

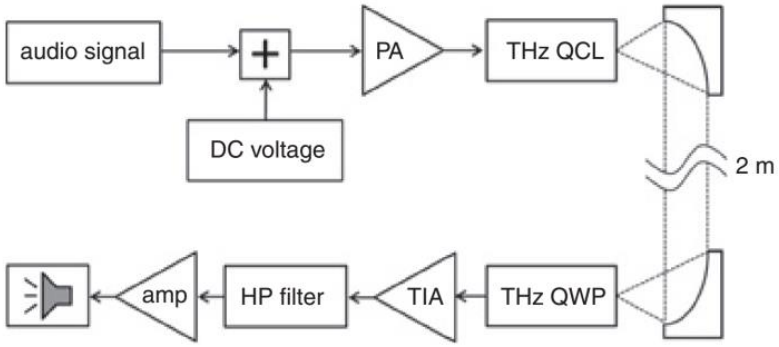

Figure 2.5 Scheme of THz transmission setup based on QCL. QCL stands for quantum cascade laser. QWP stands for quantum well photodector.
Source: [47]

2.2 Fundamentals of Infrared (IR) Communication Systems

The infrared radiation is in the wavelength range from 0.7μm to 1000μm, with corresponding frequency ranging from 300GHz to 430 THz. The whole infrared band can be further divided to three sub-regions: the near infrared region (0.7-3μm), middle infrared region (3-50μm) and far infrared region (50-1000 μm) as shown in Table 2.2.

As a medium for short-range, indoor communication, infrared technology owns several significant advantages over radio [57, 58].

(1) Low cost for infrared emitters and detectors on high speed operation.

(2) Low power requirements: ideal for telephones, laptops, and personal digital assistants

(3) Low circuitry costs: $2 - $5 for the entire coding/decoding circuitry

(4) Virtually unlimited bandwidth.

(5) Quantitatively similar behavior with visible light.

(6) Simple circuitry: no special or proprietary hardware is required. It can be incorporated into the integrated circuit of a product.

(7) Higher security: Cannot penetrate through walls or other opaque barriers. This signal confinement over short distance makes it easy to secure transmissions against casual eavesdropping.

(8) Immunity to electromagnetic interference (EMI): Prevent interference between links operating between long distances or two different rooms. Not as likely to have interference from signals from other devices.

(9) Few international regulatory constraints: IrDA (Infrared Data Association) functional devices will ideally be usable by international travelers, no matter where they may be.

Table 2.2 Division of Infrared Radiation by International Organization for Standardization

Designation	Frequency	Wavelength
Far infrared (FIR)	300 GHz-6 THz	50-1000μm
Mid Infrared (MIR)	6-100 THz	3-50μm
Near Infrared (NIR)	100-430 THz	0.7-3 μm

However, despite the advantages presented by the infrared medium, IR also shows some drawbacks:

(1) Line of sight: transmitters and receivers must be almost directly aligned (able to see each other) to communicate.

(2) Blocked from persons and objects. Communication from one room to another

requires the installation of infrared access points that are interconnected via a wired backbone.

(3) Short range: Attenuation increases and BER performance decreaseswith longer distances.

(4) Noise: Exist intense ambient infrared noise, arising from sunlight, incandescent lighting and fluorescent lighting, which induces noise in an infrared receiver.

(5) Weather sensitive: Large attenuation in atmosphere phenomena such as rain, fog, dust, pollution.

(6) Eye safety: Safety consideration must be considered when designing a wireless IR link. There are a number of international standards for laser emission: the International Electrotechnical Commission (IEC) (IEC60825-1), American National Standards Institute (ANSI) (ANSIZ136.1), European Committee for Electrotechnical Standardization (CENELEC).

The characteristics comparison between infrared and radio wireless links is presented in Table 2.3.

Table 2.3 Comparison between Infrared and Radio for Wireless Links

Property of Medium	**Infrared**	**Radio**	**Implication for IR**
Bandwidth Regulated?	No	Yes	Approval not required. Worldwide compatibility
Passes Through Walls?	No	Yes	Operate indoors More easily secured
Multipath Fading?	No	Yes	
Path Loss	High	High	
Dominant Noise	Other Users	Background Light	Difficult to operate outdoors

Source: [59]

In clear-sky weather conditions, IR signal suffers performance degradation caused

by air molecules and aerosols induced extinction. In Table 2.4 and Figure 2.6, the calculated atmospheric optical transmission windows range from 0.3μm to 14μm are shown by evaluation many broad and strong absorption bands in various data-bases [61, 62]. Considering the existing optical sources and safety regulations, most of the free space communication systems are designed and operate at wavelengths near 850nm and 1550nm. A 1.25 Gb/s optical channel at 850nm over a short range is reported by Henderson, which employs a commercially available ferroelectric LCOS display panel as a phase-modulating SLM to perform steering to correct for misalignment [63]. Due to the advantages of 1550mm wavelength, an optical wireless communication system at 1550nm with data rate of 12.5 Gb/s is demonstrated experimentally [64]. This system can realize error-free reception over a distance of 0.84m, which can be extended to more than 1m is error correction coding (ECC) is employed. Most recently, C. W. (Joanne) Oh demonstrated an infrared optical wireless communication system which achieves 36.7 Gb/s and 42.8 Gb/s transmission over a distance of 2.5m in the experiment [65, 66]. A pair of cascaded passive diffractive optical elements (DOEs) is used for steering optical data beams for 2D area coverage, which can make the system to provide a wide coverage of high capacity to multiple devices simultaneously.

Table 2.4 Atmospheric Transmission Windows

	I	**II**	**III**	**IV**	**V**	**VI**	**VII**	**VIII**
Start-wavelength (μm)	0.30	0.97	1.16	1.40	1.95	3.00	4.5	7.7
Stop-wavelength (μm)	0.92	1.10	1.30	1.80	2.40	4.20	5.2	14

Source: [67]

When IR is used for outdoor communications, its performance is degraded by significant signal loss due to the presence of rain, fog, dust and turbulence by absorption, scattering and scintillation effects. Compared to other atmospheric constituents, fog is the dominant source for the IR power loss, thus potentially reducing the IR link availability. Nevertheless, rain and dust also pose a great challenge to achieve the link availability. And in the clear weather conditions, scintillation effect by atmospheric turbulence can severely degrade the reliability and connectivity of IR links. Thus, these weather effects are needed to be investigated to improve the link performance for outdoor wireless communications.

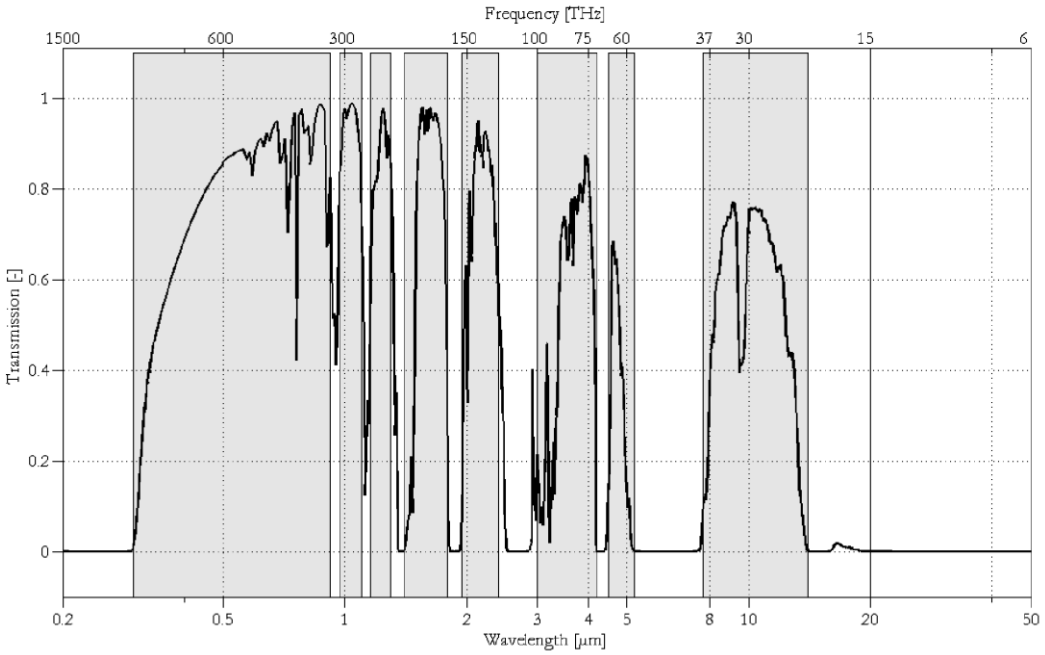

Figure 2.6 Atmospheric transmittance based on absorption analysis using LOWTRAN. A zenith path from 0 km to 120 km altitude as well as the midlatitude summer atmospheric model are assumed. Atmospheric transmission windows are highlighted in grey color.
Source: [68]

For the high speed fiber communication links, stated of polarization (SOP) changes

caused by polarization mode dispersion (PMD), is a major limitation. David Waddy's group has measured SOP in aerial fiber during summer and winter [69]. In their experiment, the weather data, such as temperature, wind speed and sun altitude, is obtained from a USA weather station. The fastest SOP changes larger than 10kHz cannot be measured due to the resolution of their measurements. In their research, they find that fast SOP fluctuation is mainly caused by the large temperature gradients.

2.3 Free-Space Power Loss on THz and IR links

The atmosphere, also called the neutral atmosphere, is defined as the part of the Earth's atmosphere where the number of ionized particles (such as free electrons, molecular and atomic ions) is negligible compared to the number of the neutral atoms and molecules. The boundary between the ionosphere and neutral atmosphere is at an altitude of about 90 km. In the atmosphere, its relative composition of the atmosphere is constant and the principle composition is given in Table 2.5.

From Table 2.5, it can be seen that nitrogen, oxygen, argon and carbon dioxide are the four most common gases in the atmosphere. Among them, the oxygen is the only component which has significant effect on the propagation of THz frequency. Water vapor, not listed in the table, is another important component due to its strong interaction with THz frequency. Based on the millimeter wave propagation model (MPM), which considers 44 oxygen spectral lines and 34 water vapor spectral lines [70], the calculated attenuation due to atmospheric gases is shown in Figure 2.7 when water vapor density is $7.5 g/m^3$, pressure is 1013 mbar and temperature is 20^oC. The curve of water vapor almost overlaps with the atmospheric attenuation, which means water vapor plays a clearly dominant role in the atmospheric attenuation for THz frequency above 100 GHz.

Table 2.5 Composition of Clean, Dry Atmospheric Air Near Sea Level

Constituent gas	Gas symbol	Content (% by volume)
Nitrogen	N_2	78.084
Oxygen	O_2	20.9476
Argon	Ar	0.932
Carbon dioxide	CO_2	0.0314
Neon	Ne	0.001818
Helium	He	0.000524
Krypton	Kr	0.000114
Xenon	Xe	0.0000087
Hydrogen	H_2	0.00005
Methane	CH_4	0.0002
Nitrous oxide	N_2O	0.00005
Ozone	O_3	Summer 0-7e-6 Winter 0-2e-6
Sulfur dioxide	SO_2	0 – 0.0001
Nitrogen dioxide	NO_2	0 – 0.000002
Ammonia	NH_3	0 – trace
Carbon monoxide	CO	0 – trace
Iodine	I_2	0 – 0.000001

Source: [69]

The THz and IR power launched into free space in outdoor will experience the absorption, scattering and scintillation due to the atmospheric weather conditions, such as rain, fog, dust, aerosols, smoke, snow and atmospheric turbulence [71, 72]. Furthermore, the attenuation in the atmosphere due to different weather conditions with respect to frequency in Figure 2.8 is modeled by the Laser Environment Effects Definition and Reference (LEEDR) modeling software provided by the Air Force Institute of Technology's Center for Directed Energy (AFIT/CDE) [73]. It can be seen that the

atmospheric attenuation for THz wave is strong and extremely variable over frequency.

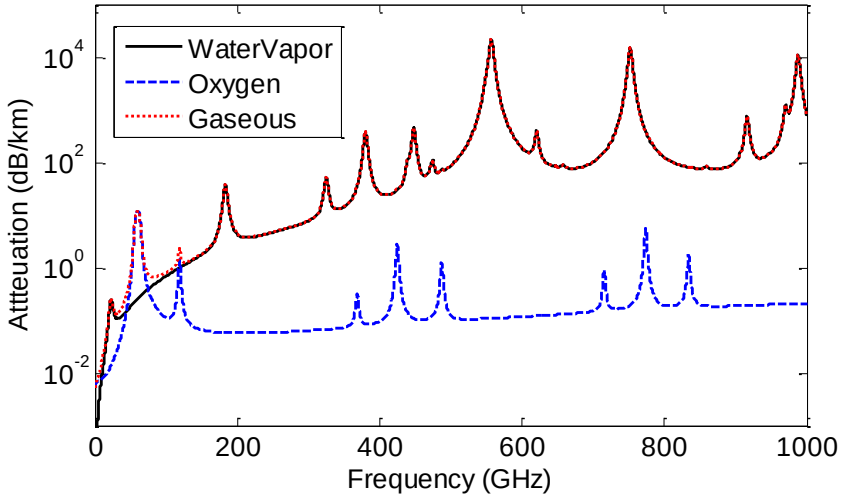

Figure 2.7 Attenuation due to atmospheric gas for 0-1000GHz based on the model of ITU Radio communication Sector (ITU-R). (Water Vapor 7.5g/m^3, Pressure 1013mbar, Temperature 20^{o}C).

Here, the major courses - absorption, scattering and scintillation, are mostly considered [74]. The attenuation, defined as the power loss of a signal propagating through the atmosphere in free space, is mainly absorption and/or scattering effects [75]. As shown in Figure 2.8, the absorption in IR range is mainly caused by oxygen and carbon dioxide in the atmosphere [76], while in THz region is primarily caused by oxygen and water vapor. In atmosphere, the laser energy is absorbed by the gaseous molecules to excite their transitions from lower to higher quantized rotational states. Scattering is mainly due to rain, fog, clouds, dust, smoke, snow and ice particles. Two kinds of scattering theory – Rayleigh and Mie scattering theories, are usually considered for the modeling based on the ratio of the scatter size and wavelength of the laser. Absorption and scattering are dominant effects which are fairly well known. And many software

packages, such as LOWTRAN, FASCODE, MODTRAN, HITRAN and LNPCWIN are commonly used for the prediction of attenuation effects suffered by different wavelengths. Scintillation, as the third source of power loss in atmosphere, occurs when laser propagates through lots of air pockets with different pressures and/or different temperatures. These air pockets can act as lenses with different indices of refraction and deflect the laser beams passing through them. In addition, airborne particulates such as dust, fog and rain can contribute to scintillation effects.

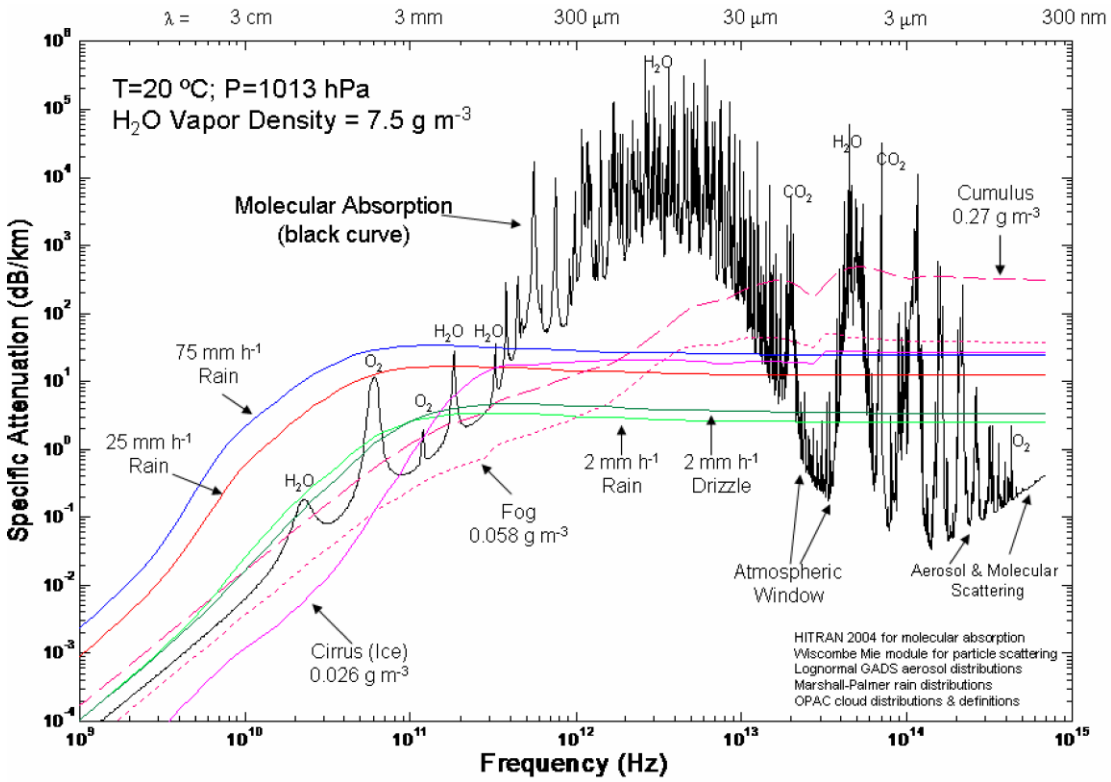

Figure 2.8 Atmospheric attenuation of electromagnetic radiation. (Temperature: 20°C, Pressure: 1013mbar, Water vapor density: 7.5g/m^3).
Source: [73]

2.3.1 Absorption

Energy in the THz frequency range is mainly absorbed by water vapor and oxygen when

it propagates through atmosphere. There are two absorption mechanisms exist: resonant and non-resonant absorption. Resonant absorption occurs on or close to the resonant absorption lines of these molecules, while non-resonant absorption occurs far away the absorption lines between the resonant frequencies. For a molecule which has an electric or magnetic dipole moment, its electric or magnetic fields can exert a torque on the molecule and change its rotational state, and then it can absorb or emit electromagnetic waves.

According to quantum mechanics, the rotational energy and angular momentum of a molecule are quantized and can be expressed by quantum numbers. When the electromagnetic waves at certain frequency corresponds to the energy difference in the quantum rotational states the gas is encountered by molecule, its photon will be absorbed and the molecule's rotational state will be excited to a higher energy state from a lower one. A simple mathematical expression can be used for this.

$$E_p = E_j - E_i, \tag{2.1}$$

here, the photon energy $E_p = h\nu$ for radiation with frequency ν. h is Planck constant. E_i and E_j are rotational energies on lower and higher states respectively. The energy difference between them is small (less than 0.005eV) compared to vibrational or electric quantum state transitions (2-4eV for a typical electronic transition).

2.3.2 Scattering

When the photon energy does not match with the resonant energy of molecule, the photon will be scattered instead of absorbed. Scattering occurs when photons interact with

molecules, atoms or other particles in the atmosphere. Actually, the photons do not contact with the scatters exactly. In quantum theory, a photon is a quanta of electromagnetic energy. The positions and momentums of photons and scatters can be expressed by quantum wave functions, which can overlap when both photon and molecule get close enough in space, and then scattering occurs.

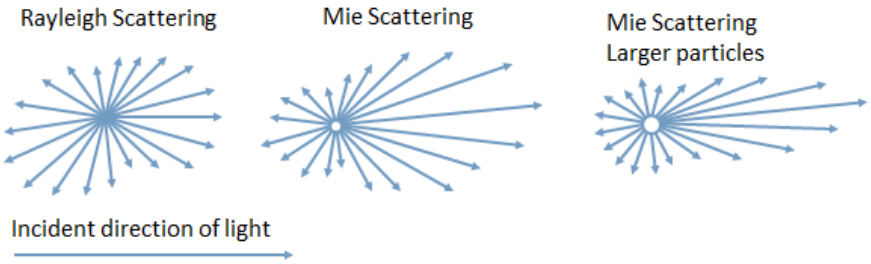

Figure 2.9 Rayleigh and Mie scattering.
Source: [77]

There are two types of collisions: inelastic and elastic collisions. Photons in the THz range can only have elastic collisions with molecules, where the energy and frequency of the photon is unchanged. Due to the very small relativistic mass of the THz photon compared to the molecule in atmosphere, the effect of the scattering on the momentum of the photon is significant. So the trajectory of the photon is altered and electromagnetic wave is deflected or spread, while the changes of the gaseous scatter are negligible. Two types of scatterings are introduced here: Rayleigh scattering and Mie scattering. Rayleigh scattering occurs when the scatter size is smaller than the EM (Electromagnetic) wavelength, while Mie scattering predominates when the scatter size is comparable to or larger than the EM wavelength. From Figure 2.9, it can be seen that Mie scattering is more directional and its forward lobe is sharper and more intense for larger scatters. Mie scattering is the dominant type of scattering from airborne particulates for

THz and IR waves.

(1) Mie Scattering

Assume S_i as the power density of an incident beam which is absorbed and scattered when incident on a scattering particle with geometrical cross-section area $A = \pi r^2$. r is the radius of a spherical particle. Absorption cross section is defined as the ratio of absorbed power P_a to the incident power density S_i,

$$Q_a = \frac{P_a}{S_i}. \tag{2.2}$$

And the scattering cross section is defined as

$$Q_s = \frac{P_s}{S_i}. \tag{2.3}$$

Then the absorption and scattering efficiency factors can be expressed as

$$\xi_a = \frac{Q_a}{\pi r^2}, \tag{2.4}$$

$$\xi_s = \frac{Q_s}{\pi r^2}. \tag{2.5}$$

The total power loss is $P_e = P_a + P_s$, and the corresponding extinction (attenuation) cross section Q_e and efficiency ξ_e are

$$Q_e = Q_a + Q_s, \tag{2.6}$$

$$\xi_e = \xi_a + \xi_s . \tag{2.7}$$

Mie investigated the solution for the absorption and scattering of laser beams expressed by normalized circumference χ and the relative index of refraction n

$$\chi = \frac{2\pi r}{\lambda_b} = \frac{2\pi r}{\lambda_0}\sqrt{\varepsilon_b^{'}} , \tag{2.8}$$

$$n = \frac{n_p}{n_b} = \sqrt{\frac{\varepsilon_p}{\varepsilon_b}} = \sqrt{\varepsilon} , \tag{2.9}$$

here, λ_b and λ_0 are wavelengths in the background medium and vacuum, respectively. $\varepsilon_b^{'}$ is the real part of the relative dielectric constant of the background medium. n_p, n_b are complex indices of refraction of the particle material and of the background medium. And ε_p, ε_b are the corresponding complex dielectric constants. In the atmosphere, $\varepsilon_b^{'} = 1$, $n_b = 1$ and $\lambda_b = \lambda_0$.

The extinction and scattering efficiencies can be calculated from Mie's solutions by

$$\xi_e(n,\chi) = \frac{2}{\chi^2}\sum_{l=1}^{\infty}(2l+1)\,\mathrm{Re}\{a_l + b_l\} , \tag{2.10}$$

$$\xi_s(n,\chi) = \frac{2}{\chi^2}\sum_{l=1}^{\infty}(2l+1)\left(|a_l|^2 + |b_l|^2\right), \tag{2.11}$$

where, Mie coefficients a_l, b_l are related to χ and n, and involve Bessel functions of complex functions. Due to the temperature dependence of refractive index, the extinction efficiency is frequency and temperature dependent. Figure 2.10 shows the extinction

efficiency with respect to frequency from 0 to 1000 GHz under different temperatures for a water drop radius is 1mm. The frequency responses of extinction, absorption and scattering efficiencies are shown Figure 2.11.

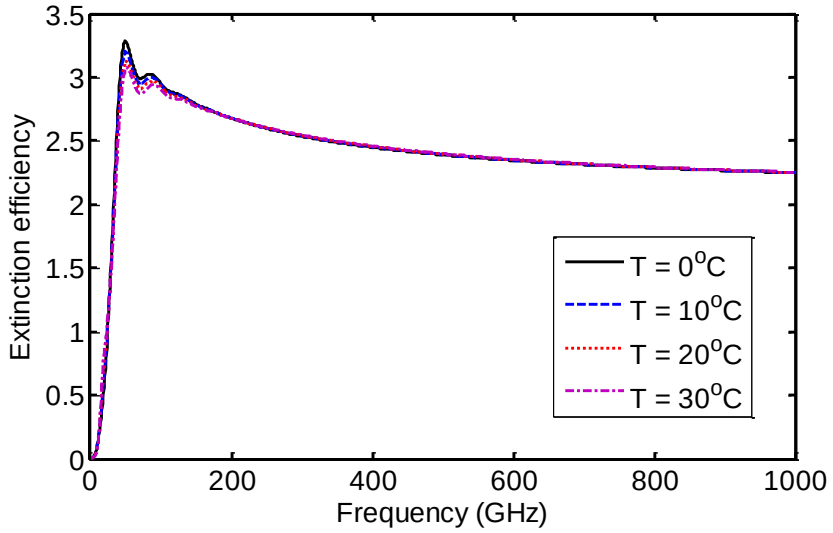

(a)

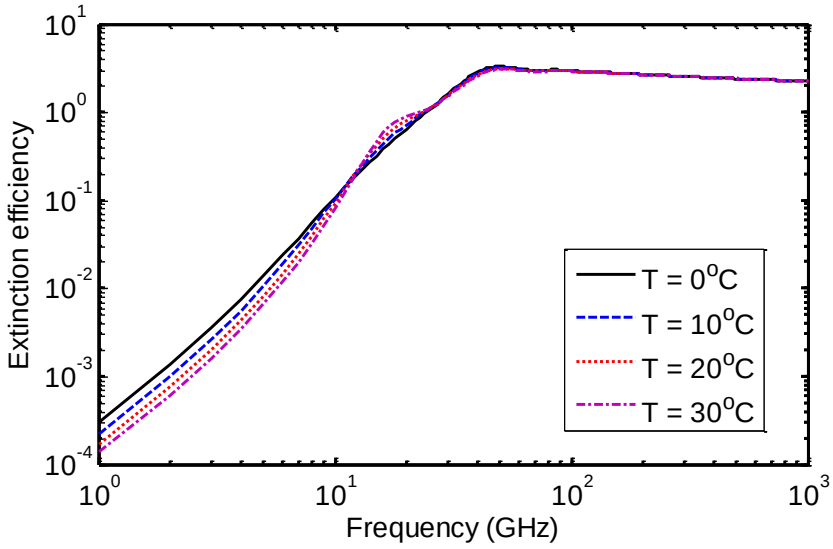

(b)

Figure 2.10 (a) Extinction (attenuation) efficiency with water drop radius 1mm (b) Logarithmic scale.

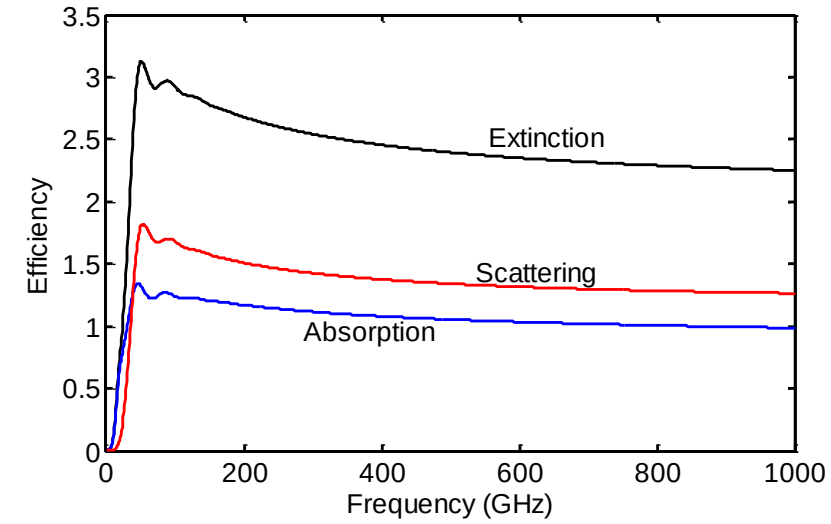

(a)

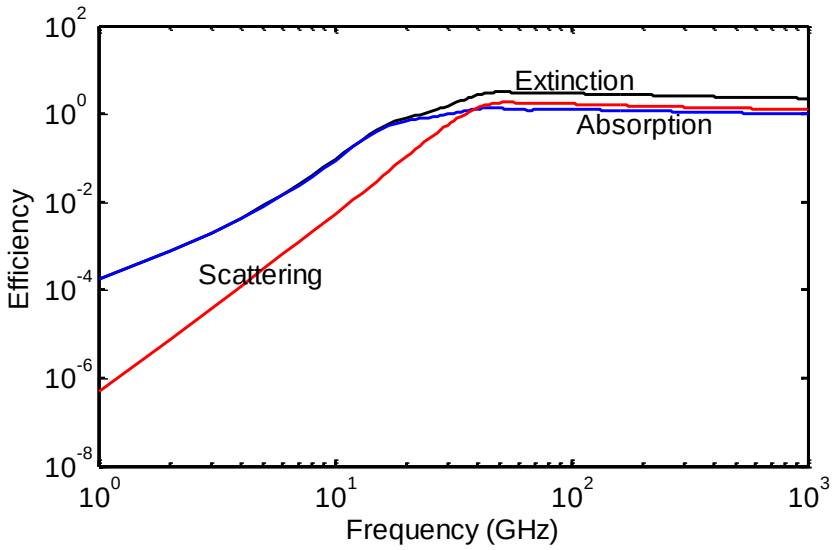

(b)

Figure 2.11 (a) Calculated extinction, absorption and scattering efficiencies with water drop radius 1mm (b) Logarithmic scale. (Temperature 20^{o}C).

(2) Rayleigh Scattering

When the wavelength is larger than the particle size, Rayleigh scattering should be considered and the expressions for extinction and scattering efficiencies can be expressed

as

$$\xi_e = 4\chi \,\mathrm{Im}\{-K\} + \frac{8}{3}\chi^4 |K|^2 + \cdots, \tag{2.12}$$

$$\xi_s = \frac{8}{3}\chi^4 |K|^2 + \cdots. \tag{2.13}$$

Here, the complex term K expressed by refractive index n

$$K = \frac{n^2 - 1}{n^2 + 2}. \tag{2.14}$$

The absorption coefficient can be obtained by

$$\xi_a = \xi_e - \xi_s = 4\chi \,\mathrm{Im}\{-K\}. \tag{2.15}$$

Figure 2.12 shows the extinction efficiency with respect to frequency from 0 to 1000GHz under different temperatures when water drop radius is 1mm.

So, Rayleigh scattering and Mie scattering are both frequency and temperature dependent. Which kind of mechanism should be considered depends on the comparison between scatter size and EM wavelength.

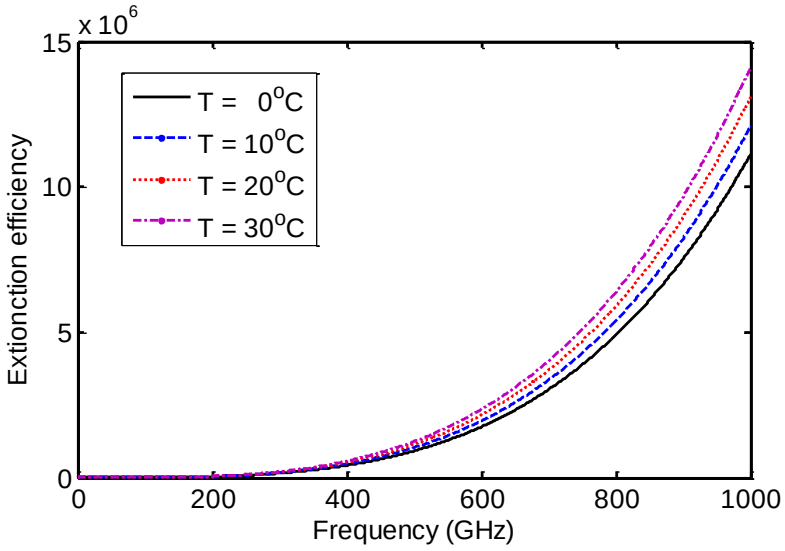

(a)

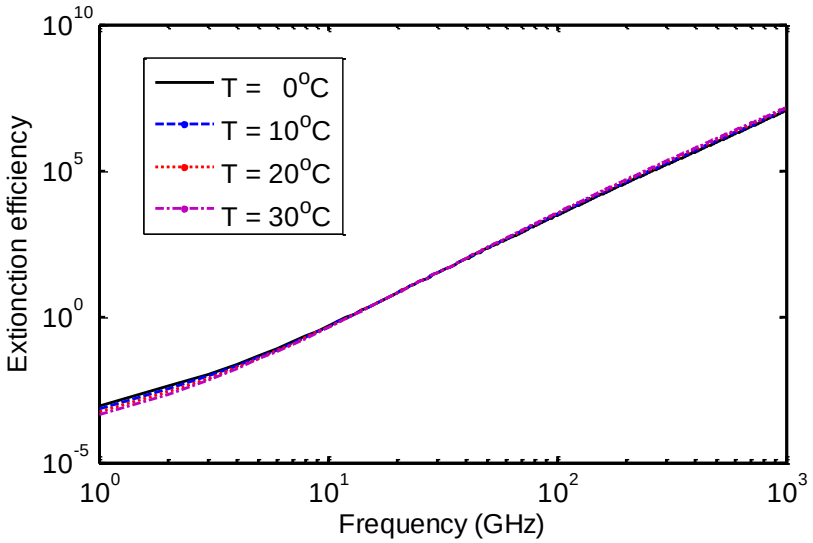

(b)

Figure 2.12 (a) Predication of attenuation for frequency up to 1000 GHz; (b) Logarithmic scale.

2.3.3 Scintillation

At the receiver plane, atmospheric scintillation can lead to light intensity fluctuation in time and space [57]. In an atmosphere free of airborne particulates, the received signal

power fluctuates due to the thermally induced air refractive index changes along the propagation path. Atmosphere can act like a series of small lenses caused by these index fluctuations, which lead to deflection of parts of the laser beam into and out of the propagation path. Further introduction for this will be shown in Chapter 4. The time scale of these fluctuations, on the order of milliseconds, is related to the wind speed. After rain, fog, clouds, and dust, scintillation is the most significant factor in clear weather that causes degradation of THz wireless communication performance, which appears to be more significant for receiver with small aperture [78]. Scintillation effect can be accumulated and becomes more serious over a long distance.

Since refractive index fluctuations in the atmosphere caused by the temperature fluctuations can deflect the laser beam from the receiver and disrupt its wave front, a constant laser beam will suffer intensity fluctuations and scintillation when it propagates through atmospheric turbulence as shown in Figure 2.13 [79]. In Figure 2.14, the index of refraction structure constant, which is always used to characterize scintillation effect, is shown. The scintillation strength depends on index of refraction structure constant C_n^2, wavelength of light and path length L through the atmosphere. These three parameters are combined together into the Rytov parameter.

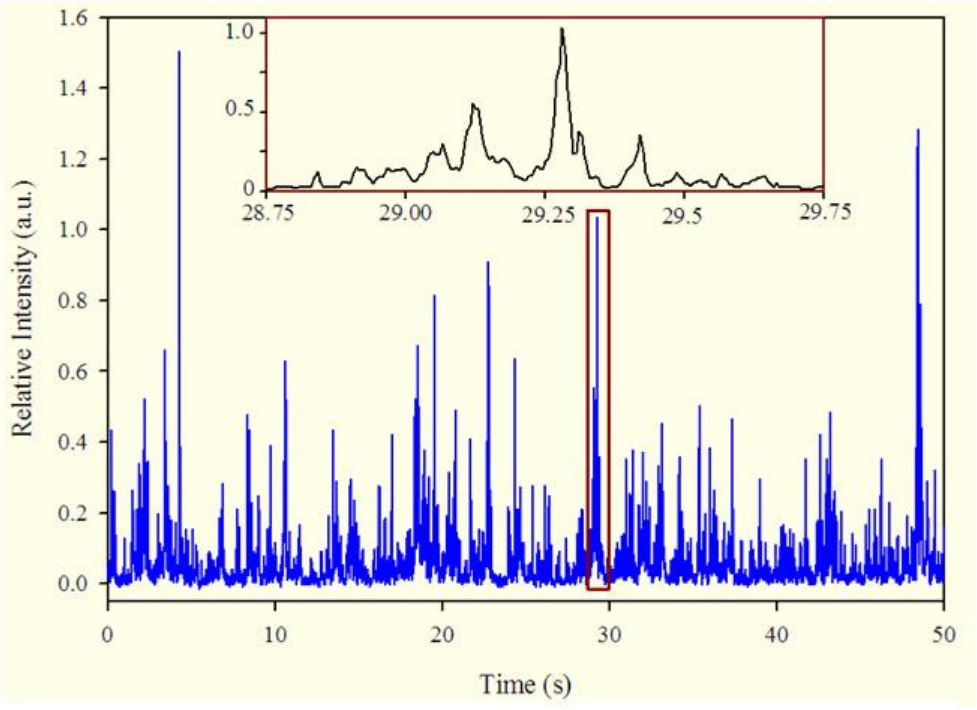

Figure 2.13 Received laser intensity after propagates through a turbulence atmosphere.
Source: [79]

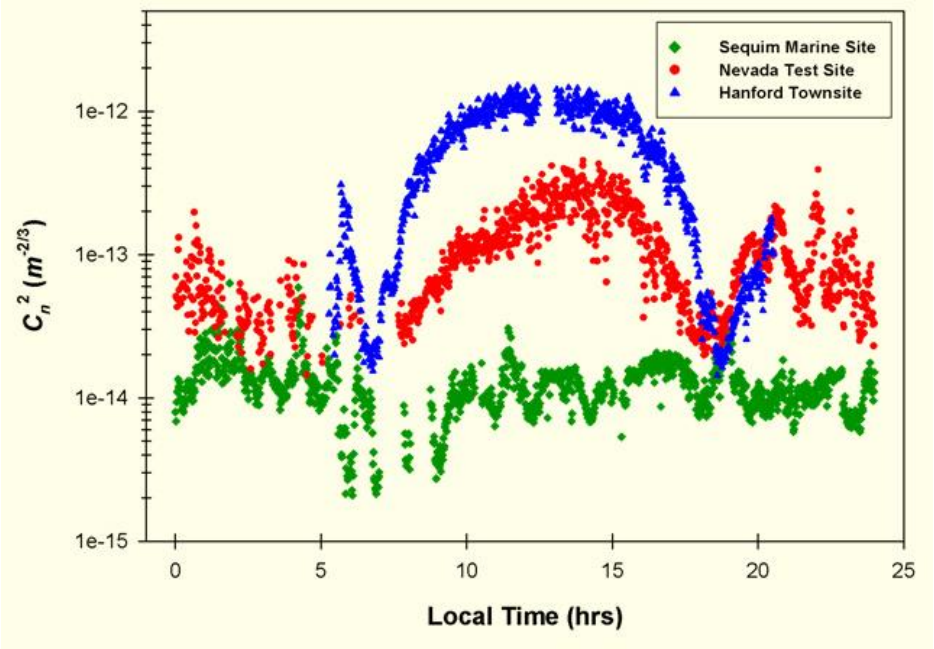

Figure 2.14 Index of refractive structure constant variation from three different locations: Hanford Town Site, Nevada Test Site and Sequim Marine Site.
Source: [79]

2.4 Weather effects on THz Communication Links

The performance of THz and IR communication links is impacted differently by weather conditions such as fog, rain, snow, cloud, water vapor and atmospheric gases. The atmosphere attenuation of THz and IR waves at sea level for different weather conditions can be compared in Figure 2.8. For fog density of 0.058g/m^3, the 1.5 μm wavelength IR signal suffers 20 dB/km power attenuation which is substantially larger than the 2 dB/km that 625GHz frequency suffers. So the communication systems at THz frequency could serve as a good candidate when IR signaling fails in fog.

2.4.1 Attenuation Due to Rain for THz Communication Links

In the rain environment, many measurements of THz power attenuation were reported and several raindrop size distributions and simulating models were found. Differences in the experimental and theoretical results indicate that further measurements are required to fully confirm these rain attenuation models and further theoretical models are needed to simulate these experiments.

Rain attenuation at 103 GHz on a propagation distance of 390 m were measured by Utsunmiya's group in 2005 [80]. They compared their measurements with the calculations based on several different raindrop size distributions - Marshall-Palmer, Best, Joss-Thams-Waldvogel and Weibull distributions as shown in Figure 2.15 and 2.16. And they found the Weibull distribution is the best fit to the measured values for 10 second and 1 minute integration time.

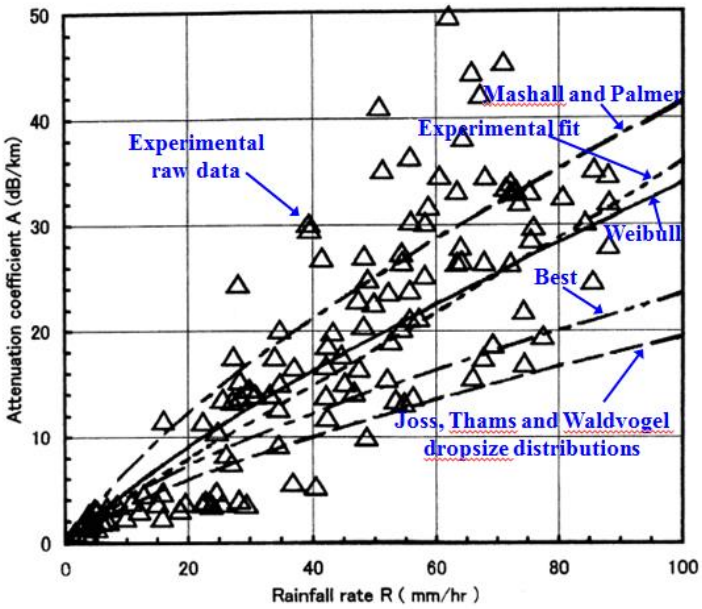

Figure 2.15 Comparison between measured and calculated attenuation due to rain for 103 GHz frequency for integration time of 10 second.
Source: [80]

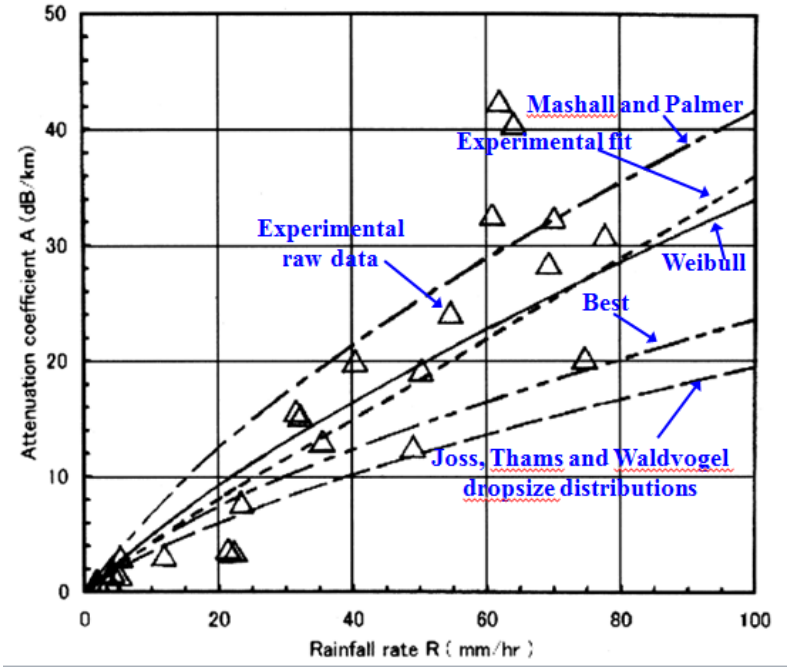

Figure 2.16 Comparison between measured and calculated attenuation due to rain for 103 GHz frequency for integration time of 1 minute .
Source: [80]

Babkin's group conducted wave propagation at 313GHz in rain with rain rate up to 12mm/hr in the central part of the European part of the former Soviet Union [81]. Then, Ishii's group calculate the corresponding attenuation due to rain by using Marshall-Palmer, Best, Polyakva-Shifrin and Weibull raindrop size distributions, and a specific attenuation model by ITU-R [82]. Figure 2.17 shows the measured attenuation due to rain is compared with the calculations under different raindrop size distributions. It can be seen that the experimental results are in very good agreement with the calculation from Weibull and ITU-R specific attenuation model.

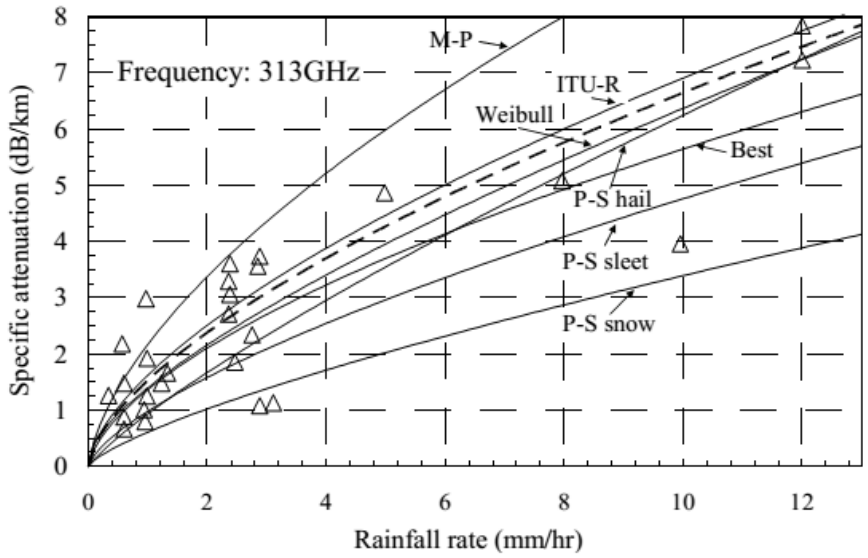

Figure 2.17 Comparison of measured and calculated attenuation due to rain for 313GHz frequency. M-P: Marshall and Palmer, P-S: Polyakva and Shifrin.
Source: [82]

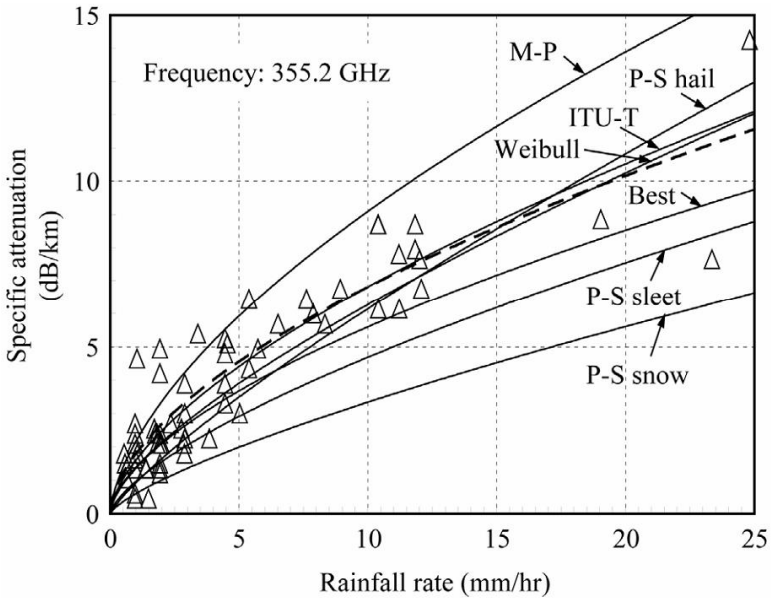

Figure 2.18 Comparison between measured and calculated attenuation due to rain for 355.2GHz frequency. M-P: Marshall and Palmer, P-S: Polyakva and Shifrin.
Source: [34]

In 2011, Ishii's group measured the rain attenuation at 355.2 GHz and compared their measurements with models based on many different raindrop size distributions and ITU-R specific attenuation model [34]. Comparison between measured and calculated attenuation values are shown in Figure 2.18, which proves that Weibull distribution and ITU-R model are in good agreement with their measurements, and the best fit is the calculation from ITU-R specific attenuation model.

The measurements of THz attenuation at 120 GHz due to rain is measure by Hirata's group for a 10Gb/s data rate during the heavy rain period and annual rain period over a distance of 400m [35]. The measurements are shown in Figure 2.19 and compared with the theoretical calculations using five rain drop size distributions: Laws and Parsons distribution with heavy rain [L-P(H)] and light rain [L-P(L)], Marshall–Palmer distribution (M-P), Joss Thunderstorm distribution (J-T), and Joss Drizzle distribution of

(J-D). Results show that the L-P and ITU models agree well with the measurements in the range from 20 to 60 mm/h for the heavy rain period and from 10 to 80 mm/h for the annual rain period.

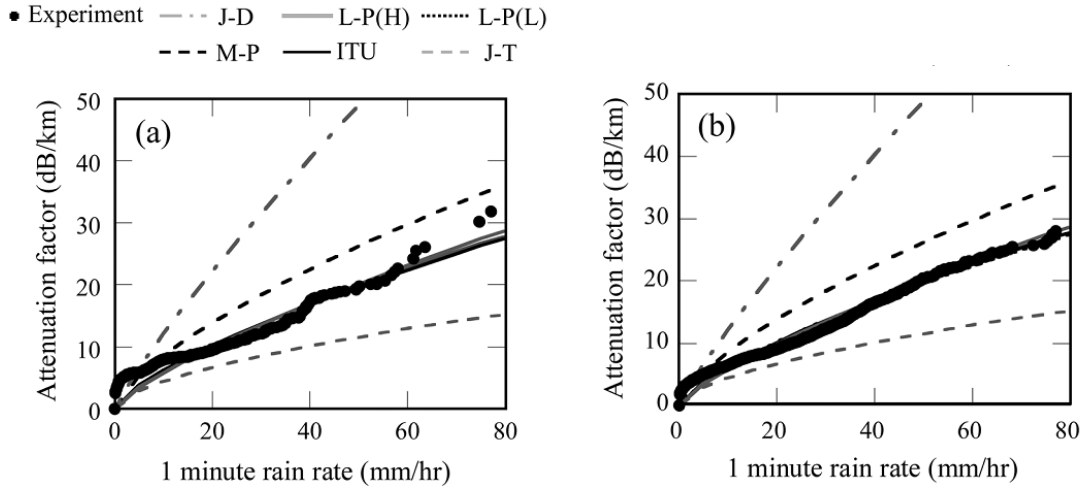

Figure 2.19 Comparison between measured and calculated attenuation due to rain for 120 GHz frequency during (a) heavy rainy period and (b) annual period.
Source: [35]

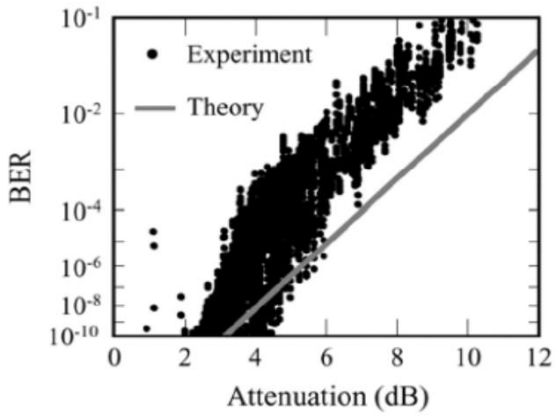

Figure 2.20 Measured and predicted BER for 120GHz wireless link with respect to power attenuation due to rain.
Source: [35]

Besides, they observed a discrepancy, which is shown in Figure 2.20, between

their experimental measurements and calculated values using random noise theory: the BER increases relative to the theoretical predictions as the rain attenuation increases, but the degradation of BER is worse than the theoretical value. So they thought there may be two possible reasons for this: wave front distortions (scintillations) due to the rain and the difference in the measurement cycle for rain attenuation of 1s and for BER of 100 ps.

2.4.2 Scintillation Effects on the THz Communication Link

Scintillation effects were observed experimentally at frequencies near 116, 140, 173, and 230 GHz in clear weather, rain, fog and snow [83]. Shahid Ahmed Khan's group measured the scintillation effects at 97 GHz and used the Mousley-Vilar equation to model the long-term probability distribution of scintillation amplitudes [84]. In Bao's study, he found that the Rytov's method is a good model to characterize the scintillation effect on THz wave and show that the scintillation effect is very important for the practical THz propagation. There are some more experimental results concerning the effect of scintillation on THz communication [85-87].

The scintillation effects due to wind on 125 GHz frequency propagating in free space is measure by Yamaguchi's group [33]. The whole transmitter and receiver systems are covered by weather-proof boxes to isolate the effects of weathers. A telescope finder was used and its axis was aligned with the antenna axis to detect the receiver axis deviation. In Figure 2.21, the receiver axis deviation increases when the wind velocity is increased, and this lead to the decrease of the input power. But, they did not observe the increase of BER caused by the wind because the input power was always greater than the minimum required value.

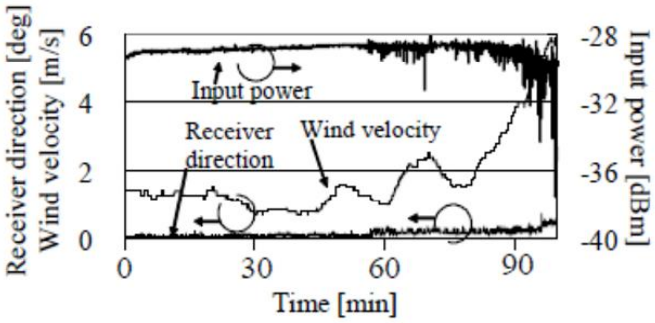

Figure 2.21 Measured input power with respect to wind velocity and receiver axis deviation.
Source: [33]

Even though there are lots of theoretical and experimental works about the effects of outdoor THz wireless performance, a comprehensive analysis is still needed. That's because it is challenging to measure the impact of these effects under outside weather conditions due to its long observation time and difficulty in obtaining some occurrence of similar weather conditions to verify results of independent measurements. In this dissertation, experimental and theoretical characterization and investigation of the weather conditions on THz and IR wireless communication channels are demonstrated. Different methods are introduced to control the weather conditions to emulate the outdoor environments.

2.5 Summary

In this chapter, a complete review of the THz wireless communication technology together with its block diagram and performance is described. Different kinds of transmitters and receivers and its mechanisms are detailed. Fundamentals of IR technology together with its advantages and disadvantages for communication are outlined. The principle composition of the atmosphere is listed and the attenuation of

electromagnetic radiation due to different components is shown. The main degradation effects on THz and IR wireless communication links by outdoor weather conditions, such as absorption, scattering and scintillation, are introduced. Mie theory and Rayleigh scattering theory can be employed for the prediction of the attenuation of signals due to the weather conditions. The present studies about many kinds of weather conditions on THz communication are shown briefly.

CHAPTER 3

EXPERIMENTAL SETUP OF COMMUNICATION CHANNELS

THz and IR wireless communication setups were developed in our lab for the comparison of the signaling performance of THz and IR links under different weather conditions. In this chapter, the experimental design of the frequency multiplier chain based 625GHz communication link is presented mainly [54]. The IR wireless communication link at 1.5μm wavelength [88], duobinary modulation technique [89, 90] and a Mach-Zehnder Interferometer [91] are also described.

3.1 625 GHz Wireless Communication Systems

A frequency multiplier chain based 625 GHz wireless communication system was developed in our lab, which can obtain high output power and larger transmitter bandwidth at a high carrier frequency. In the system, a duobinary modulation technique is employed to ensure that a sufficiently narrow spectrum bandwidth can be efficiently passed through an up-converting frequency multiplier chain [92]. This 625 GHz source can realize large power output when compared with current commercially available transmitter architectures. A Schottky diode operating in direct detection modes is employed on the receiver side to covert the THz signal to baseband. This design is less complex than mixer based receivers. Figure 3.1 shows the block diagram of this setup where the main transmitter and receiver components are evident.

3.1.1 THz Transmitter

The THz transmitter (Virginia Diodes Inc.), based on a Frequency-Multiplier-Chain, can realize maximum output power of about 1 mW operating in a continuous wave mode.

It is composed of an amplifier driven at 2 W saturation power followed by four frequency doublers and one frequency tripler. All of them are based on biased Schottky diodes, which feed a horn antenna with aperture of 2.4 mm. As a result of the frequency multiplication, a frequency band between 585 GHz and 653 GHz can be up-converted from a launched tone within the frequency acceptance band between 12.2 GHz and 13.6 GHz.

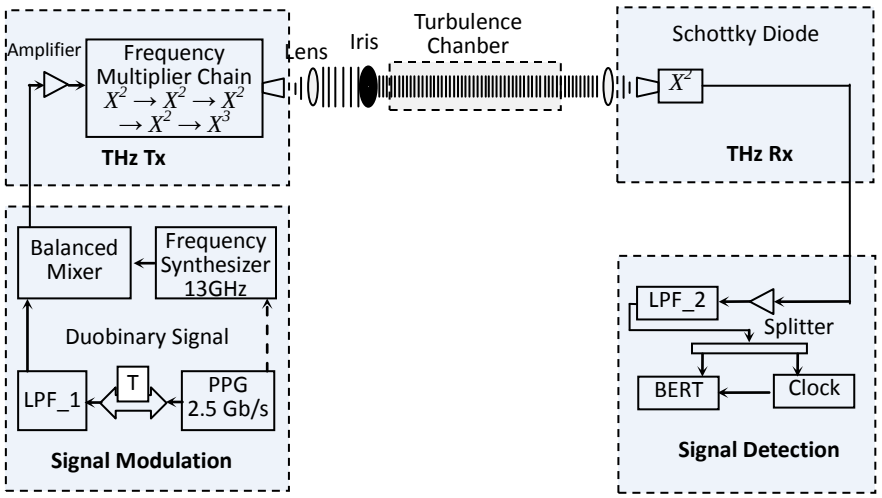

(a)

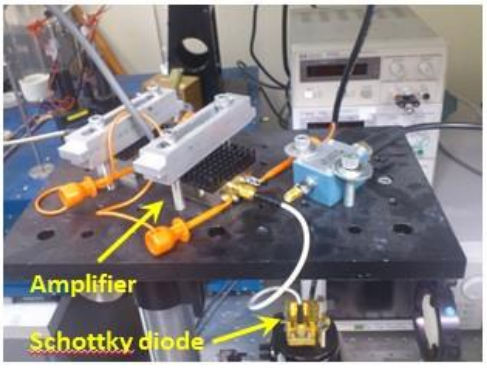

(b)

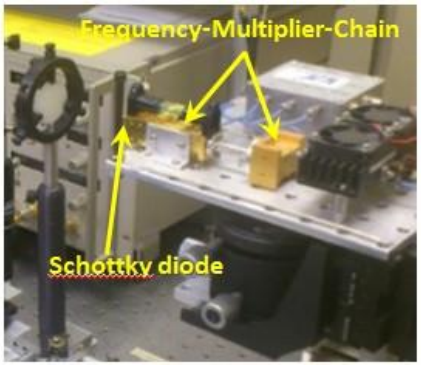

(c)

Figure 3.1 (a) Schematic of up converting frequency multiplier chain based 625 GHz transmission link, (b) Snapshots of the transmitter and receiver.

3.1.2 Transmission Channel

A THz lens with short focal length of 32 mm is employed to collimate the output of the horn antenna with beam diameter of ~ 15 mm. Then the beam is transmitted up to a length of 3 meters, and coupled by an identical THz lens into a similar horn antenna with its output connected to a zero biased Schottky diode.

3.1.3 THz Receiver and Signal Detection

The detector operates in the low power region with input power smaller than 10 μW. This detector is good approximation a square law converter with a responsitivity of about 2500 V/W at 600 GHz. The Schottky diode's output is amplified by about 42 dB using two amplifiers (80 kHz-7 GHz pass band, 6 dB noise figure, maximum output power ~19 dBm) and filtered by a quasi-Gaussian low pass filter (LPF-2) with 3GHz 3dB-bandwidth. A 6 dB electrical power splitter launches one output (Vpp ~ 500mV) to a Bit Error Rate Tester (BERT) and the other to a 2.5 Gb/s NRZ clock recovery circuit that synchronizes the measurement equipment.

The detector used is based on commercially available Schottky diodes. Such design is sub-optimal for high-speed signaling. Under low input power, the video resistance of the diodes is nominally ~ 1.5k Ohm and connected via a series of 50 Ohm transmission lines and cables to an external high-speed electrical amplifier with matched input impedance [94]. For low speed applications and after replacing the amplifier with a high impedance device, a voltage of about 70 mV at the Schottky diode output is detectable. However with 50 Ohm termination of the diode a significantly smaller voltage level is accessible at the high-speed amplifier input.

3.2 1.5 μm IR Wireless Communication System

The block diagram of the main transmitter and receiver elements of IR communication link with data acquisition interfaces is shown in Figure 3.2.

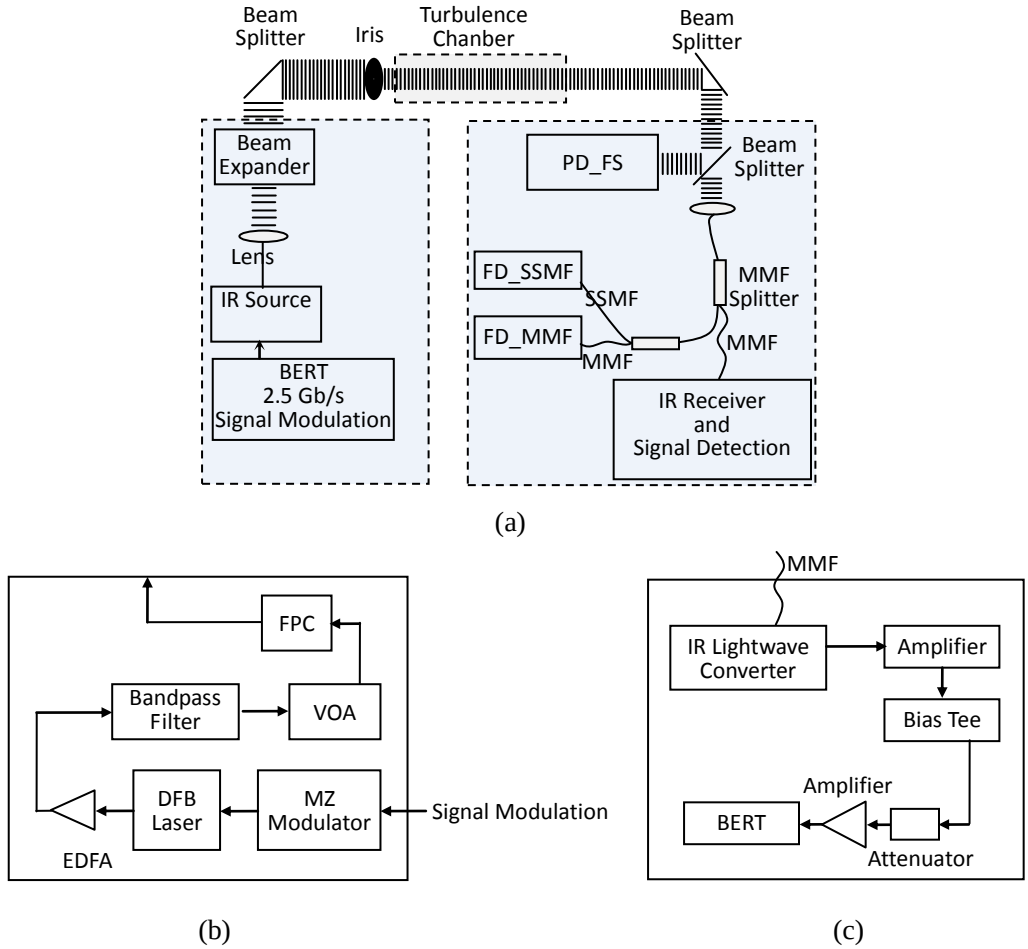

Figure 3.2 (a) Schematic diagram of IR wireless communication link, (b) IR transmitter, (c) IR receiver and signal detection.

3.2.1 Transmitter and Receiver Elements of IR Communication Link

In Fig, 3.2 (a), the IR transmitter is composed by a DFB (distributed feedback) laser with output wavelength ~1550 nm, a Mach-Zehnder optical modulator, a high power EDFA

(erbium-doped fiber amplifier), a narrow bandwidth optical filter with bandwidth of ~1 nm, a low loss VOA (variable optical attenuator) and a FPC (fiber based polarization controller). Standard single mode fibers are used for connections.

The beam splitting ratio is polarization dependent and the FPC is adjusted to achieve the maximum detectable receiver power. The Mach-Zehnder modulator is driven by the same 2.5 Gb/s NRZ signals as the THz transmitter. An EDFA amplifies the modulator output to about 25 dBm, which is the maximum input power of the bandpass filter. This reduces the detection of spontaneous emission on the receiver side.

The IR transmitter is driven by the same 2.5 Gb/s NRZ data pattern as the THz transmitter. The IR beam is expected to about 15 mm diameter by a fiber collimator, which is comparable to the THz beam size before the iris. The collimated IR beam is superimposed with the THz beam using a thin (2 μm) Pellicle Beamsplitter (Thorlabs) with 55% reflection ratio at 45^{o} incident angle, and transmitted through the turbulence chamber. After emerging from the chamber, the beam is deflected with a similar beam splitter which taps off a fraction of the IR power leaving the chamber and launches it towards a large area free space photodetector with effective area of 19.6 mm^2. The remaining beam power is coupled via a fiber collimator into a 1×2 multimode fiber (MMF) coupler with 50:50 splitting ratio. A fraction of its output power is launched to a DC-coupled IR lightwave convertor (Agilent 81495A) with large bandwidth. The remaining IR power enters another 1×2 multimode fiber (MMF) coupler. A low bandwidth photodetector with a standard single mode fiber (SSMF) is coupled to one output port while the other is connected to a photodetector via MMF. The outputs of the free space detector (PD_FS), the PD connected to SSMF (PD_SSMF) (core diameter

~9μm), and the PD connected to MMF (PD_MMF) (core diameter ~50μm) are recorded via a DAQ board with 16 bit resolution and a maximum sampling rate of 125 kHz. The sampling rate is sufficiently high to track even the fastest fluctuations of the signals which has been verified by measuring the spectrum of the PDs' electrical output signals. There are essentially no fluctuations in IR power above a few tens of kHz. A lightwave convertor, which is accessible via general purpose interface bus (GPIB) is used for both data detection and measuring the optical power of the incoming signal (Siegel, 2004). The ac-output of the bias tee is strongly attenuated and thereafter amplified in order to level the signal-to-noise ratio (SNR) such that BERs around 10^{-7} and higher can be adjusted while satisfying the BERT requirements of input voltage swings between 250 mV and 2 V.

3.2.2 Data Acquisition

The output of PD_FS, PD_SSMF, and PD_MMF are recorded via a DAQ board with 16 bit resolution and up to 125 kHz sampling rate, sufficiently high to track even the fastest fluctuations of the signals. BERs, RF power of THz signal, and optical power of the IR signal are recorded via GPIB. A LabView time controller, set to a minimum clock rate of 500 ms, which the GPIB interface can handle, synchronizes all recordings.

3.3 Duobinary Modulation

Duobinary modulation is a scheme for transmitting data rates using less bandwidth compared to regular (non-return-to-zero) NRZ modulation by applying phase coding and pulse widening [93]. In the setup, the source's acceptance frequency band between 12.8-13.6 GHz for an applied input RF tone requires multi Gb/s data rate signals with comparably narrow bandwidth such that intersymbol interference (ISI) effects caused by

bandwidth reduction can remain small [95-97]. So, the delay-and-add approach is employed to generate the duobinary modulation.

As shown in the signal modulation block of Figure 3.1, a 2.5 Gb/s NRZ format is generated by a PPG (pulse pattern generator) with adjustable output power. The signal is divided into two replicas by means of a wideband 6 dB electrical power splitter and one branch is delayed by the duration of a bit (400 ps) with respect to the other. The replicas are combined with another 6 dB power splitter, terminated with 10 dB 50 Ohm attenuators at both input, in order to achieve better impedance matching and less reflections. The resulting signal possesses three amplitude levels (-1, 0, 1). A quasi Gaussian low pass filter (LPF-1) with about 1700 MHz 3 dB bandwidth is then applied to reduce the spectral width of the signal, mainly by cutting off its tail. This signal is launched into the intermediate frequency (IF) port of a double balanced mixer where the data modulates the output of a frequency synthesizer that is connected to the local oscillator (LO) port. It is a specific feature of the double-balanced mixer that a negative input at the IF port causes a 180 degree phase shift of the signal at the radio frequency (RF) output. This is utilized to establish the required phase coding for duobinary modulation. The data signal enters the THz source and modulates the THz radiation which emanates from the horn antenna of the THz source with 2.4 mm aperture. Note, after the first frequency doubler of the source, the duobinary phase coding is eliminated due to the squaring operation of the Schottky diode.

3.4 Mach-Zehnder Interferometer

To characterize the turbulence induced phase change, visible light (632.8nm) from a Mach-Zehnder Interferometer (MZI) is co-propagated with the THz and IR beams. Figure

3.3 shows the schematic diagram of the MZI design embedded in the test bed. A He-Ne laser beam (632.8nm) with a diameter of 2 mm is first split into two parts by a beam splitter (BS1) and then recombined by a second beam splitter (BS2). The combined beams form localized interference fringes. One part of the visible beam co-propagates with the THz and IR beams at a small angle (< 3^{o}) while the other part of the visible beam propagates through ambient air which is isolated from the turbulence chamber ($90 \times 40 \times 30 cm^{3}$). Air flows into the chamber with constant velocity and temperature.

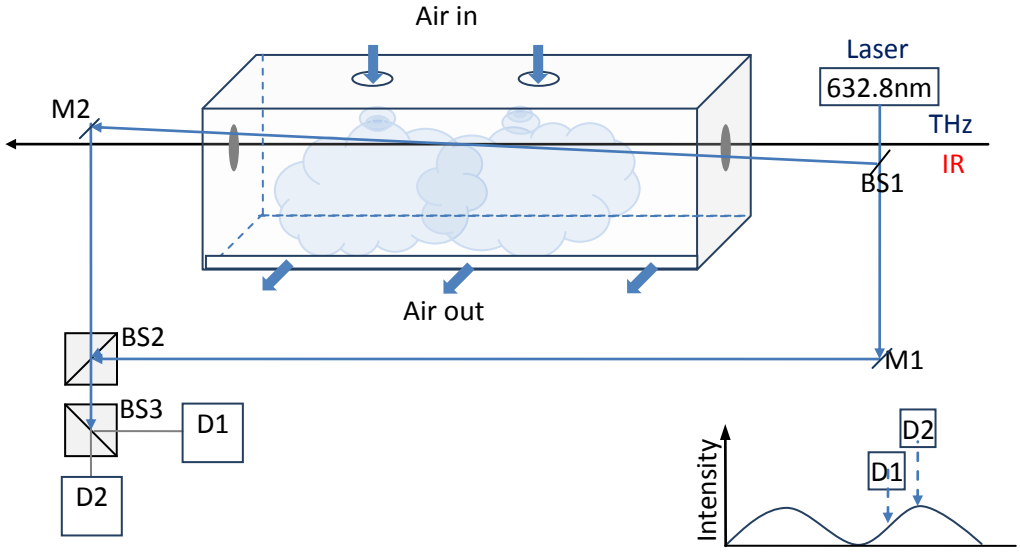

(a)

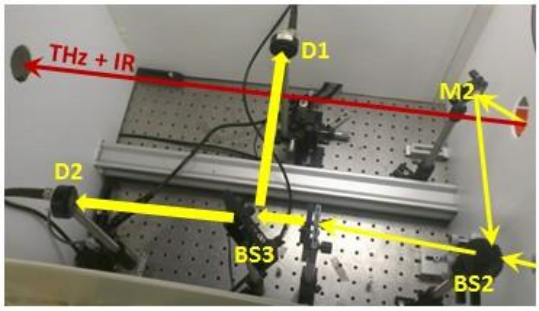

(b)

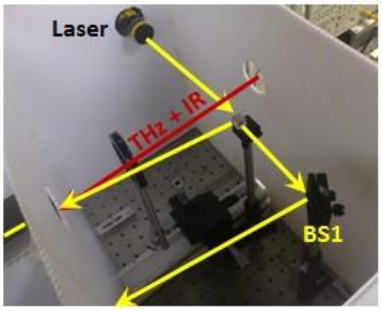

(c)

Figure 3.3 (a) Schematics of a Mach-Zehnder interferometer setup to characterize turbulences with visible light. ($L_{ab}=L_{bc}=L_{cd}=15cm$); Inset: Position of photodectors D1, D2 relative to interference fringe intensity; (b) and (c) corresponding setup in the laboratory.

The refractive index change of the turbulent air inside the chamber relative to the ambient air leads to phase change and deflection of the beams passing through the chamber. The total phase change of a wave represents the accumulated turbulence impact in this chamber. To investigate the phase change, a beam splitter (BS3) is used to split the visible beam and launch parts of it after magnification onto two photo-detectors (D1, D2). The detectors' apertures are about 500μm which is small compared to the width of the interference fringes (~5mm). In the absence of air flow and turbulence, D1 is adjusted to detect the interference fringes at a medium intensity and D2 to detect the peak interference fringe intensity. By comparing the D1 and D2, and measuring whether the power at D1 is increasing or decreasing, one can analyze the sign of the phase change. Since the refractive index changes are similar in all three wavelength bands [16], measuring it at visible wavelengths allows us to estimate the cumulative refractive index fluctuations inside the turbulent air for the THz and IR signals.

The 632.8nm laser beam is considered as a uniform plane wave and is split by BS1 as

$$U_1 = A_1 \exp\left[j\left(\phi_0 + ks_1\right)\right], \tag{3.1}$$

$$U_2 = A \exp\left[j\left(\phi_0 + ks_2\right)\right], \tag{3.2}$$

where A is amplitude, ϕ_0 is initial phase delay, k is the wavenumber, and s_1 and s_2 are the path lengths shown in Figure 3.3. The total field at the point of BS2 is the sum of the two fields

$$U_{total} = U_1 + U_2 = A\exp\left[j\left(\phi_0 + ks_1\right)\right] + A\exp\left[j\left(\phi_0 + ks_2\right)\right]. \tag{3.3}$$

The intensity at this point is

$$I_{total} = \left|U_1\right|^2 + \left|U_2\right|^2 + U_1 \cdot U_2^* + U_1^* \cdot U_2 . \tag{3.4}$$

Equation (3.4) can be rewritten as

$$\begin{aligned} I_{total} &= A^2 + A^2 \\ &+ A^2 \exp\left[j\left(\phi_0 + ks_1\right)\right]\exp\left[-j\left(\phi_0 + ks_2\right)\right] + A^2 \exp\left[-j\left(\phi_0 + ks_1\right)\right]\exp\left[j\left(\phi_0 + ks_2\right)\right] \end{aligned} \tag{3.5}$$

Simplifying Eq. (3.5), one can get

$$\begin{aligned} I_{total} &= A^2 + A^2 + A^2 \exp\left[j\left(ks_1 - ks_2\right)\right] + A^2 \exp\left[j\left(ks_2 - ks_1\right)\right] \\ &= 2A^2\left[1 + \cos\left(k\left(s_1 - s_2\right)\right)\right] \end{aligned} . \tag{3.6}$$

Let $s_1 - s_2 = \Delta$ being the path difference due to the refractive index change, and can be written as $s_1 - s_2 = \Delta n \cdot L$. L is the chamber length. Then Eq. (3.6) can be

$$I_{total} = 2A^2\left[1 + \cos\left(k\Delta nL\right)\right]. \tag{3.7}$$

Equation (3.7) shows that the intensity of the interference pattern should be a cosine squared distribution which was first observed by ThomasYoung in 1801.

After BS3, the voltages detected by D1 and D2 are

$$V_1 = V_0\left[1 + \cos\left(k\Delta nL + \pi/2\right)\right], \tag{3.8}$$

$$V_2 = V_0\left[1+\cos\left(k\Delta nL\right)\right]. \tag{3.9}$$

So, one can infer the phase change by an unwrapping algorithm from

$$\cos\left(k\Delta nL\right)+ j\sin\left(k\Delta nL\right)=\left(\frac{V_2-V_0}{V_0}\right)-j\left(\frac{V_1-V_0}{V_0}\right). \tag{3.10}$$

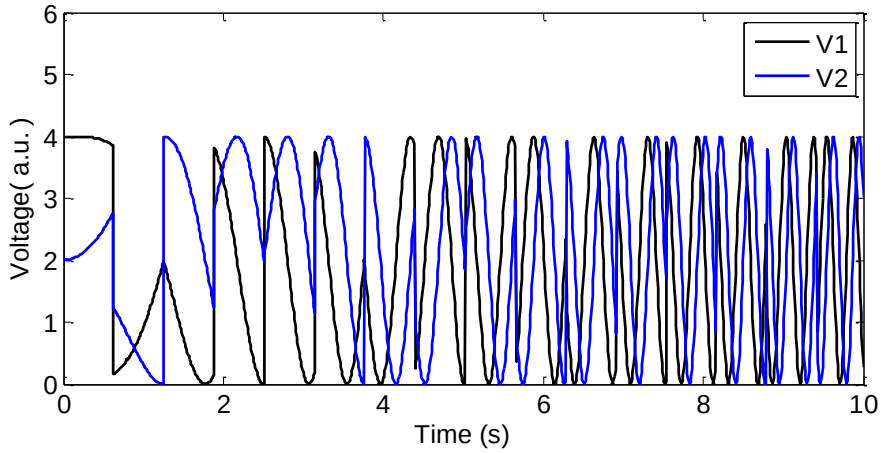

(a)

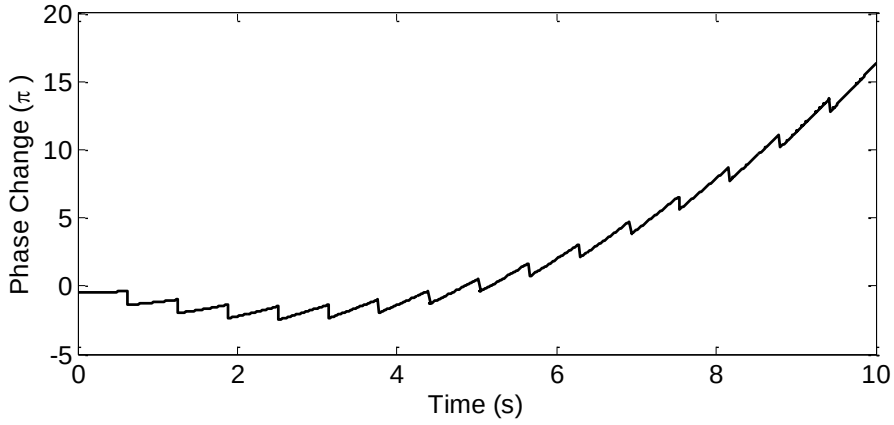

(b)

Figure 3.4 (a) Theoretical output of photodetectors D1 and D2 and (b) it's corresponding phase change.

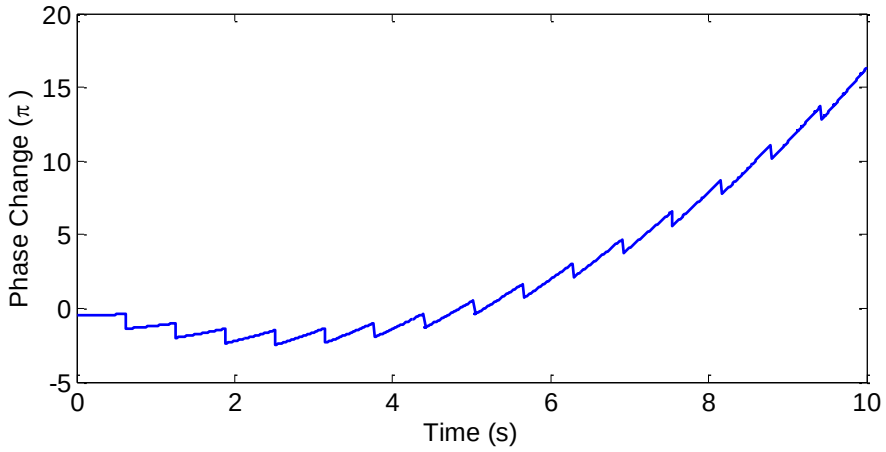

Figure 3.5 Calculated phase change based on our method and unwrapping algorithm.

Assume the outputs from photodetectors D1 and D2 based on Eqs. (3.8) and (3.9) are shown in Figure 3.4 (a) and Figure 3.6(a) with the assumed corresponding phase difference shown in Figures 3.4 (b) and 3.6 (b). By using the method shown in Eq. (3.10) and unwrapping algorithm in Matlab 2012b, the calculated phase changes are shown in Figures 3.5 and 3.7, which are identical to the input phase change in Figures 3.4(b) and 3.6(b). So this confirms that the unwrapping algorithm works well for the phase difference calculation.

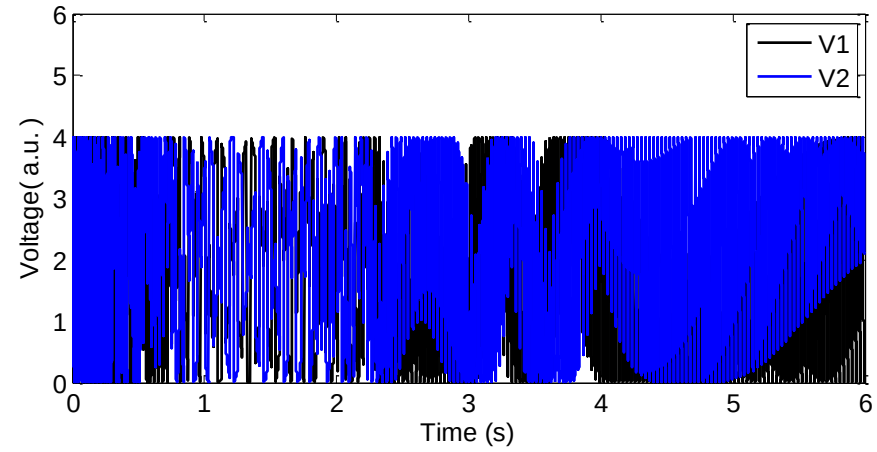

(a)

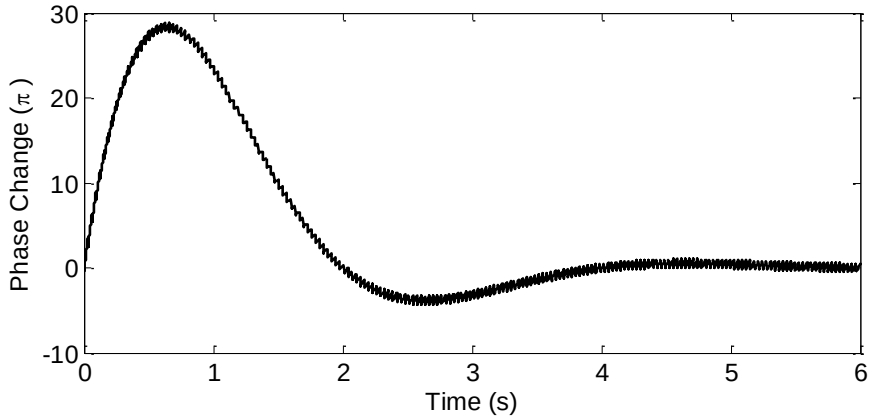

(b)

Figure 3.6 (a) Theoretical output of photodetectors D1 and D2 and (b) it's corresponding phase change.

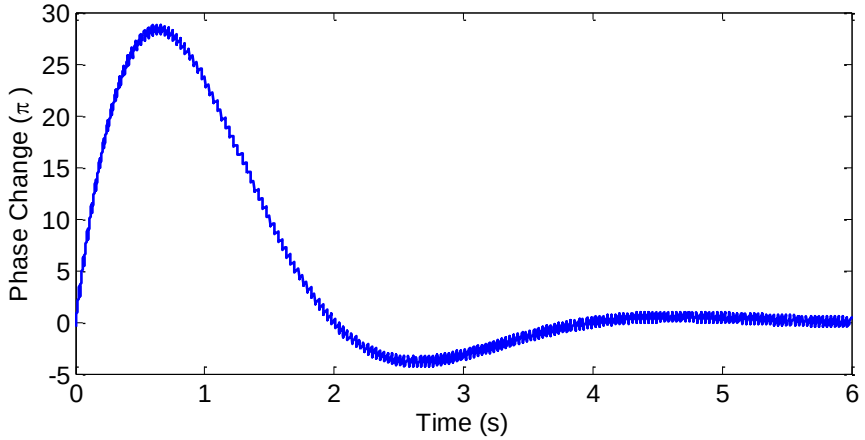

Figure 3.7 Calculated phase change based on our method and unwrapping algorithm.

3.5 Summary

A Frequency-Multiplier-Chain based 625 GHz transmitter is detailed in this chapter, which can realize high output power and larger transmitter bandwidth at a high carrier frequency. The THz wave is radiated by a horn antenna and collected by a similar horn antenna with a THz lens. In the receiver side, the detector is based on Schottky diodes which can realize high-speed signaling. A duobinary modulation is generated by using the delay-and-add approach to get a sufficiently narrow spectrum bandwidth. The IR transmitter is composed by DFB laser, Mach-Zehnder optical modulator, EDFA, optical filter, optical attenuation and fiber based polarization controller. In the IR receiver side, the IR signal is split to several parts for the power detection and scintillation effect confirmation. In this setup, Labview software is used for the instrument controlling and data recording. A Mach-Zehnder interferometer is developed to measure the phase change induced by the atmospheric turbulence in the communication links. The acoustic noise induced by the air supplier for the air turbulence generation is analyzed also in this chapter.

CHAPTER 4

ATMOSPHERIC THURBULENCE THEORIES

It is well known that rain, snow, fog, dust, etc. influence the transmission of laser beams through the atmosphere by three effects: absorption, scattering, and atmospheric turbulence. Absorption and scattering by the constituent gases and particles of the atmosphere give rise primarily to attenuation of the laser beam. In clear weather conditions, apart from absorption and scattering, atmospheric turbulence also impairs the laser beam performance [98-100].

4.1 Air Turbulence Introduction

As a laser beam propagated through the atmosphere, it suffers attenuation and scintillation effect. Attenuation refers to the scattering and absorption due to aerosols and molecules [71, 106-108]. The absorption and scattering is the main contribution to signal attenuation [107]. When the scattering particle is comparable in size with the laser wavelength, Mie scattering occurs and the laser beam is scattered to the forward direction as mentioned in Section 2.3. In general, atmospheric attenuation is mainly dependent on the different weather conditions.

In the presence of clear weather for which attenuation and scattering by airborne particulates should be minimal, the propagation of a laser beam can still be affected by air turbulence. Radiated solar radiation penetrates into earth’s atmosphere and absorbed by the earth. This leads to the air around the earth surface becomes warmer and lighter than at higher altitudes. So the warmer and cooler air mix thoroughly with each other to become uniform, and this causes the random fluctuation of the air temperature [101, 102].

So, turbulence is caused by the temperature inhomogeneities presents in the atmosphere [103, 104] which can also be understood as air pockets of different sizes with changing temperatures. These air pockets of variable temperatures can act like prisms with different refractive indices, which will alter the directions of the laser beam when it propagates through the atmosphere. Then random fluctuation of the received signal power and phase front distortion occur [105], and further degrade the performance of wireless links. Atmospheric turbulence can be characterized by the inhomogeneity of the refractive index in the atmosphere along the beam path due to spatial and temporal temperature fluctuations. So, when the propagating laser beam suffers intensity fluctuation at the receiver side, scintillation effect occurs. For long paths (> 1km) parallel or near to the ground, scintillation is dominant and can lead to a time-varying fading effect on the order of milliseconds.

Some effects of the atmospheric turbulence are listed as follows [109, 110]

(1) Scintillation – The phase front of the laser beam is distorted due to the variation of the index of refraction, thus leading to the irradiation fluctuation or scintillation.

(2) Beam spreading – The laser beam is spread by diffraction in the propagation path, thus resulting in the beam spreading.

(3) Beam wandering – The deflection of the laser beam is caused when the diameter of the turbulence eddies are greater than the laser beam diameter.

(4) Beam steering – The beam is out of the receiver aperture range due to the angular deviation of the beam from its initial Line-of-sight target.

(5) Image dancing – The focus of the laser beam moves randomly in the receiver plane due to the variations of the arrival-angle of the beam.

4.2 Air Turbulence Characterization

Based on the theory of turbulence and laminar movement of viscous fluid, the

atmospheric turbulence can be modeled and studied. The Reynolds number $R_e = vl/v_o$, as a very important parameter in the fluid dynamics, is usually used to characterize the turbulence flow of a viscous fluid. This parameter is a non-dimensional quantity defined by Reynolds with v_o as the kinematic viscosity in m^2/s, v as the characterized velocity of flow in m/s and l (m) as the dimension of the flow. R_e=2000 is regarded as a critical value. When the Reynolds number exceeds this value, turbulence flow occurs [111]. Similarly, atmospheric turbulence caused by the variation in the air temperature and pressures contributes to the fluctuation of index of refraction [108, 106].

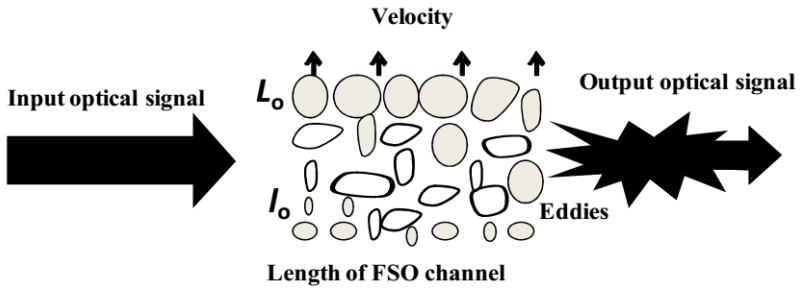

Figure 4.1 Atmospheric channel based on velocity fluctuations with turbulent eddies.
Source: [108]

Principally, Navier-Stokes equations can be employed to model turbulence [112]. But, because this modelling is a nonlinear process, it will be very complex. So, Kolmogrov theory is given which employs energy cascade theory for the explanation of turbulence baded on dimensional analysis and approximations for simplification [108]. According to cascade theory, when the wind velocity reaches to one point where the critical Reynolds number exceeds the normal air flow, air pockets of different temperatures and variable sizes are formed and distributed randomly. As mentioned previously, the turbulence can be understood as air pockets of different sizes with

changing temperatures floating in the air. The air pockets' scales range from an outer scale also called the larger scale size L_0 to the inner scale called the small scale size l_0. During the turbulence process, larger air pockets can be broken by inertial forces into smaller ones. Formation of wind shear or convection is responsible for the large scale energy pockets, while small scale pockets (smaller than the inner scale) leads to the dissipation of energy from these air pockets [108]. These small air pockets act like prisms to trigger a random interference effect between different points of the propagating beam and then distort wave front as shown in Figure 4.1.

Air pockets are usually considered to be statistically uniform and isotropic. They are smaller than the outer scale L_0 which grows linearly with respect to the height above the ground from the observer to about 100 meters. This means that the velocity field is constant in its mean value and the correlations between random fluctuations from point to point just depend on their separation instead of the observation points in the field. In Kolmogorov theory, the longitudinal structure function of the wind velocity along the propagation path of the wireless link between two points *i* and *j* follows a power law equation in [113, 114]

$$D_v\left(L_{ij}\right)=\left\langle\left(v_i-v_j\right)^2\right\rangle=\begin{cases}C_v^2 L_{ij}^{2/3}, & l_0 \ll L_{ij} \ll L_0\\ C_v^2 l_0^{-4/3} L_{ij}^2, & 0 \le L_{ij} \ll l_0\end{cases}. \tag{4.1}$$

Here the velocity structure constant C_v^2 is a measure of the total amount of the energy in the turbulence. v_i and v_j are the velocity components at point *i* and *j*. Mostly, The atmospheric turbulence can be explained by velocity fluctuation. Alternatively, the temperature structure function can also be used to characterize turbulence by following a

similar power law equation [108, 115]

$$D_T\left(L_{ij}\right)=\left\langle\left(T_i-T_j\right)^2\right\rangle=\begin{cases}C_T^2L_{ij}^{2/3}, & l_0\ll L_{ij}\ll L_0\\ C_T^2l_0^{-4/3}L_{ij}^2, & 0\le L_{ij}\ll l_0\end{cases}. \tag{4.2}$$

Here C_T^2 is the temperature structure constant. T_i and T_j represent the temperature at point *i* and *j*. There is a 2/3 power law behavior in the upper expression in Eqs. (4.1) and (4.2), corresponding to the inertial subrange. Kolmogorov first suggested it on the basis of dimensional analysis [108]. At small distances, the quadratic behavior of the structure at small separation distances can be conducted by employing Taylor series. The temperature structure function based on the temperature gradient along the laser beam path is a very easy and useful method to characterize the atmospheric turbulence. In our research, this method is employed to characterize the atmospheric turbulence, and it will be found that it is very convenient and accurate.

For the characterization of the atmospheric turbulence and the description of the intensity fluctuation, many statistical models, such as log-normal distribution model, gamma-gamma model, K-distribution model and negative exponential distribution model, were developed. But none of them is suitable for all the turbulence conditions due to the non-stationary nature of turbulence [108]. Log-normal distribution model is uniquely defined by a signal parameter directly related to the weather measurements. It is widely employed for weak turbulence because that it is mathematically simple and matches well with the experimental measurements for weak turbulence. The gamma-gamma model could be used to characterize both the strong and weak turbulence conditions [115, 17, 117]. The K-distribution, as a special case of gamma-gamma model, is found suitable for

strong turbulence [118-120]. The negative exponential distribution is always used for saturation regimes [121]. In this chapter, the log-normal model is employed due to its simplicity and the generated weak turbulence in the setup.

4.2.1 Log-normal Model

As the name implies, the log-amplitude of laser intensity follows a normal (Gaussian) distribution when the central limit theorem is applied [120]. The laser intensity of laser sections scattered from a great number of independent scatters is modeled along the beam path in the medium.

The electric field $\vec{E}(\mathbf{r})$ of a monochromatic wave propagating in the atmosphere can be conducted from Maxwell's equation as [99, 122]

$$\nabla^2 E(\mathbf{r}) + k^2 n^2(\mathbf{r}) E(\mathbf{r}) - \nabla \cdot \left[\nabla \cdot E(\mathbf{r})\right] = 0\,, \tag{4.3}$$

where, $k = \dfrac{2\pi}{\lambda}$ is the wave number. The last term of Eq. (4.3) refers to the turbulence induced depolarization part of the propagating wave in atmosphere, which can be ignored when the scale of turbulence is larger than the wavelength [71, 123]. $n(\mathbf{r})$ refers to the random refractive index which can be expressed as a free-space term plus turbulence-induced term as

$$n(\mathbf{r}) = 1 + n_t(\mathbf{r})\,. \tag{4.4}$$

According to Rytov approximation, the electric field can be expressed in the complex form as the multiplication of unperturbed and perturbation terms

$$E(\mathbf{r}) = \exp\left(\Psi_0(\mathbf{r}) + \Psi_1(\mathbf{r})\right). \tag{4.5}$$

Here, $E_0(\mathbf{r}) = \exp\left(\Psi_0(\mathbf{r})\right)$ is the unperturbed incident field and $\exp\left(\Psi_1(\mathbf{r})\right)$ refers to the first order perturbed field due to turbulence. The other orders of perturbation terms are neglected for simplification, which is valid for weak turbulence conditions. The turbulence-induced field fluctuation can be written as

$$\Psi_1(\mathbf{r}) = \chi(\mathbf{r}) + j\delta(\mathbf{r}). \tag{4.6}$$

Here, $\Psi_1(\mathbf{r})$ is Gaussian distributed, so $\chi(\mathbf{r})$ denotes the log-amplitude fluctuation in Gaussian distribution and $\delta(\mathbf{r})$ denotes the log-phase fluctuation in Gaussian distribution. Therefore, the field irradiance in terms of intensity fluctuations at any point in the atmospheric turbulence along the beam path is

$$I(\mathbf{r}) = \left|E(\mathbf{r})\right|^2 = \left|E_0(\mathbf{r})\right|^2 \mathrm{e}^{2\chi(\mathbf{r})} \quad . \tag{4.7}$$

The field amplitude follows log-normal distribution due to the Gaussian distribution of $\chi(\mathbf{r})$ as

$$p_\chi(\chi) = \frac{1}{\sqrt{2\pi\sigma_\chi^2}} \exp\left(-\frac{\left(\chi - E[\chi]\right)^2}{2\sigma_\chi^2}\right), \tag{4.8}$$

where $E[\chi]$ denotes the mean of the log-amplitude and $\sigma_\chi^2 = \langle\chi^2\rangle - \langle\chi\rangle^2$ refers to the log-amplitude variance, which is usually related to the Rytov variance σ_R^2. Using the Kolmogorov spectrum in the study of plane waves or spherical waves, it is customary to distinguish these cases by values of the log-amplitude variance for spherical wave and

plane wave [108]

$$\sigma_\chi^2 = 0.56k^{7/6}\int_0^L C_n^2(\chi)(L-\chi)^{5/6}d\chi \quad \text{plane wave,} \tag{4.9}$$

$$\sigma_\chi^2 = 0.563k^{7/6}\int_0^L C_n^2(\chi)(\chi/L)^{5/6}(L-\chi)^{5/6}d\chi \quad \text{spherical wave,} \tag{4.10}$$

where, k and L represent wave number and parallel path length. C_n^2 is regarded as a constant for horizontal propagation of a field in the atmospheric turbulence. Considering the relation between intensity and amplitude, the log-intensity can be expressed as

$$l = \ln\left(\left|\frac{E(\mathrm{r})}{E_0(\mathrm{r})}\right|^2\right) = 2\chi \ . \tag{4.11}$$

So, the intensity follows the same log-normal distribution which can be derived by invoking the transformation of variable as

$$p(I) = \frac{1}{\sqrt{2\pi\sigma_l^2}I}\exp\left(-\frac{\left(\ln\left(\frac{I}{I_0}\right)-E[l]\right)^2}{2\sigma_l^2}\right) \ . \tag{4.12}$$

Here, the log-intensity variance can be $\sigma_l^2 = 4\sigma_\chi^2$ based on Eq. (4.11), and the mean log-intensity can be $E[l] = 2E[\chi]$. Some experimental results have shown that the intensity fluctuations obey log-normal distribution for weak atmospheric turbulence conditions [124].

From Eq. (3.8) with a normalized mean, i.e., $E\left[\frac{I(\mathbf{r})}{I_0(\mathbf{r})}\right] = E\left[\mathrm{e}^{2\chi(\mathbf{r})}\right] = 1$, so

$$E\left[\mathrm{e}^{2\chi(\mathbf{r})}\right] = \exp\left(2E\left[\chi(\mathbf{r})\right] + 0.5\times 2^2\sigma_\chi^2\right) = 1. \tag{4.13}$$

So, one can conclude $E[l] = -\sigma_l^2/2$. Then, the log-normal pdf based on Eq. (4.12) is plotted as shown in Figure 4.2 with irradiance variance 0.1, 0.2, 0.5. The log-normal distribution is more skewed with longer tails towards infinity with variance increasing, which confirms the intensity fluctuation increase due to atmospheric turbulence.

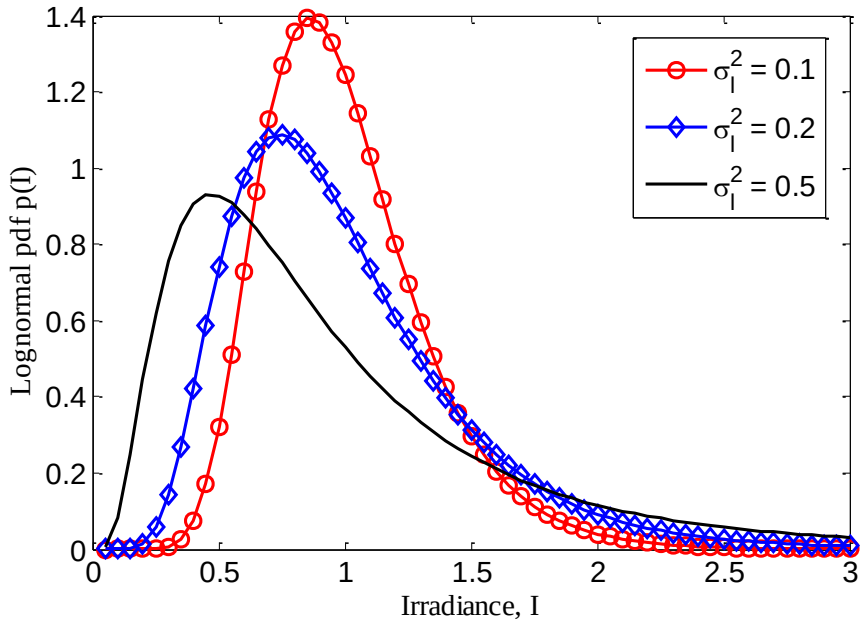

Figure 4.2 Log-normal probability density function with respect to irradiance for different irradiance variances 0.1, 0.5, 0.8.

The scintillation index refers to the variance of irradiance fluctuation scaled by the square of the mean irradiance, which can be given by Rytov variance under Rytov approximation to

$$\sigma_R^2 = 1.23 C_n^2 k^{7/6} L^{11/6} \quad \text{plane wave,} \tag{4.14}$$

$$\sigma_R^2 = 0.5 C_n^2 k^{7/6} L^{11/6} \quad \text{spherical wave .} \tag{4.15}$$

Weak fluctuations are associated with $\sigma_R^2 < 1$, and strong fluctuations are associated with $\sigma_R^2 \gg 1$. The Rytov variance implies the normalized irradiance variance in weak fluctuations, and also is considered as a representation of turbulence strength related to C_n^2 and the path length L [108, 113, 125].

Table 4.1 Strength of Turbulence Based on Rytov Variance

Turbulence Strength	σ_R^2
Weak	< 0.3
Medium	~ 1
Strong	>> 1

Source: [108]

4.2.2 Gamma-gamma Model

The gamma-gamma turbulence model considers that the light intensity fluctuation is attributed to the small scale and large scale atmospheric effects [126]. The small scale leads to scattering (scintillation) by air pockets smaller than the Fresnel zone $R_F = \left(L/k\right)^{1/2}$ or the coherence radius ρ_0 of the light, whichever is smaller. Here *k* refers to wave number and *L* stands for the propagation distance. Large scale effects lead to refraction which are due to the air pockets that are larger than the first Fresnel zone or the scattering disk $L/k\rho_0$, whichever is larger. In gamma-gamma distribution, the received

intensity of the light can be expressed as the product of two independent random variables I_x and I_y , $I = I_x I_y$. Here, both variable arise from large to small scale air pockets and obey gamma-gamma distribution with probability density function (pdf) as

$$p(I_x) = \frac{\alpha(\alpha I_x)^{\alpha-1}}{\Gamma(\alpha)} \exp(-\alpha I_x), \quad I_x > 0, \ \alpha > 0 \ , \tag{4.16a}$$

$$p(I_y) = \frac{\beta(\beta I_y)^{\alpha-1}}{\Gamma(\beta)} \exp(-\beta I_y), \quad I_y > 0, \ \beta > 0 \ . \tag{4.16b}$$

Here, α and β are the effective number of large and small scale cells, respectively. Changing one variable as $I_y = I/I_x$, the conditional pdf can be obtained as

$$p(I|I_x) = \frac{\beta(\beta I/I_x)^{\beta-1}}{I_x \Gamma(\beta)} \exp(-\beta I/I_x), \quad I > 0 . \tag{4.17}$$

Here, I_x is regarded as the mean value of I . In order to derive the unconditional intensity distribution, an average over the Gamma distribution of (4.16a) on Eq. (4.17) is conducted and the gamma-gamma distribution function is obtain as

$$\begin{aligned} p(I) &= \int_0^\infty p(I|I_x)\, p(I_x)\, dI_x \\ &= \frac{2(\alpha\beta)^{(\alpha+\beta)/2}}{\Gamma(\alpha)\Gamma(\beta)} I^{\frac{\alpha+\beta}{2}-1} K_{\alpha-\beta}\left(2\sqrt{\alpha\beta I}\right), \quad I > 0 \end{aligned} \ . \tag{4.18}$$

Here, $\Gamma(\cdot)$ stands for the gamma function and $K_{\alpha-\beta}(\cdot)$ represents the modified Bessel function of the 2nd order of $\alpha - \beta$. When a plane wave is assumed, the effective numbers

α and β can be expressed as [127-129]

$$\alpha = \left[\exp\left(\frac{0.49\sigma_R^2}{\left(1+1.11\sigma_R^{12/5}\right)^{7/6}} \right) - 1 \right]^{-1}, \tag{4.19a}$$

$$\beta = \left[\exp\left(\frac{0.51\sigma_R^2}{\left(1+0.69\sigma_R^{12/5}\right)^{5/6}} \right) - 1 \right]^{-1}. \tag{4.19b}$$

If spherical wave is assumed, then the parameters become [128, 130]

$$\alpha = \left[\exp\left(\frac{0.49\sigma_R^2}{\left(1+0.18d^2+0.56\sigma_R^{12/5}\right)^{7/6}} \right) - 1 \right]^{-1}, \tag{4.20a}$$

$$\beta = \left[\exp\left(\frac{0.51\sigma_R^2\left(1+0.69d^2\sigma_R^{12/5}\right)^{-5/6}}{\left(1+0.9d^2+0.62d^2\sigma_R^{12/5}\right)^{5/6}} \right) - 1 \right]^{-1}. \tag{4.20b}$$

Here, $d = \sqrt{kD^2/4L}$ with D the receiving lens aperture diameter.

The gamma-gamma turbulence model can be used to characterize turbulence with any strength from weak to strong. Based on Eq. (3.19), the distribution is plotted in Figure 4.3 under different turbulence strengths, which shows that the distribution spreads more under higher turbulence strength.

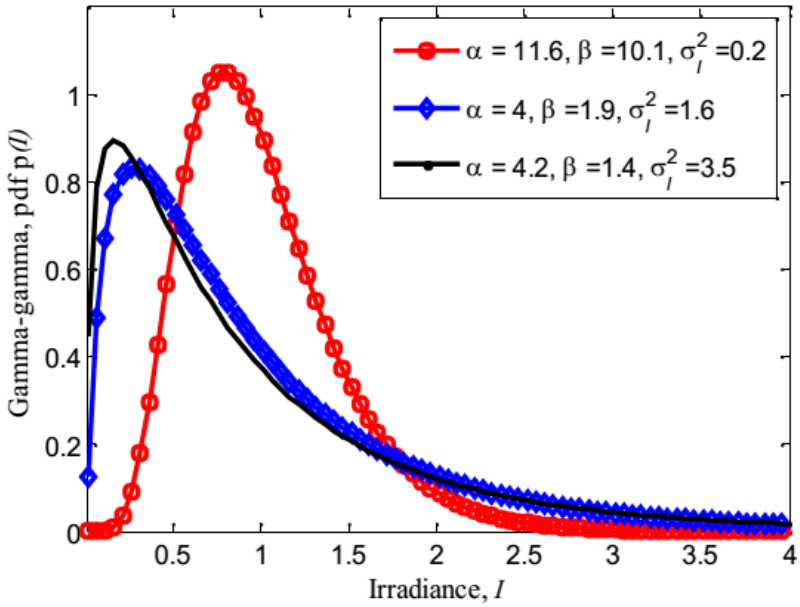

Figure 4.3 Gamma-gamma probability density function with respect to irradiance for different turbulence strengths: weak, moderate and strong.

4.2.3 K-distributed Model

The K-distributed model, as a special case of gamma-gamma model when $\beta = 1$, is a useful method to characterize strong turbulence [131] when the scintillation index ranges from 2 to 3 or the propagation length is larger than 1km [132]. The distribution function can be expressed by setting $\beta = 1$,

$$f_K(I) = \sum_{p=0}^{\infty} \left[a_p(\alpha,1) I^p + a_p(1,\alpha) I^{p+\alpha+1} \right], \quad I > 0, \tag{4.21}$$

where, the effective number α lies between 1 and 2 [133].

4.2.4 Negative Exponential Model

The negative exponential model is usually employed to characterize the intensity fluctuation in the saturation regime [115, 134], which can be given by

$$f_{NE}(I) = \frac{1}{I_0}\exp\left(-\frac{I}{I_0}\right), \quad I > 0 \ . \tag{4.22}$$

Here, the mean intensity $E[I] = I_0$ is assumed to be unity in the saturation regime. So, Eq. (4.22) becomes

$$f_{NE}(I) = \exp(-I), \quad I > 0 \, . \tag{4.23}$$

The exponential distribution based on Eq. (4.22) under different mean intensities are shown in Figure 4.4, where the mean values of the distribution reduces significantly with the intensity as I_0 decreases.

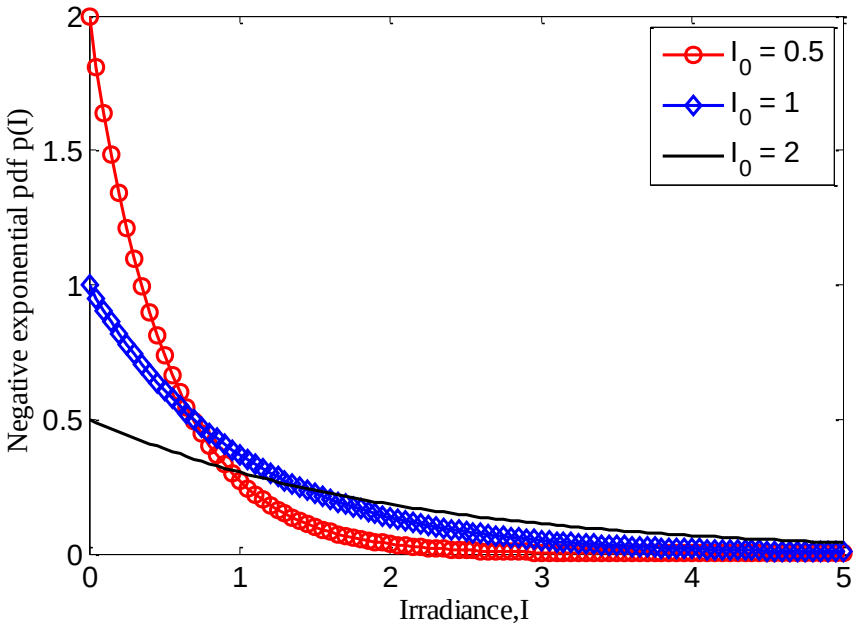

Figure 4.4 Negative exponential probability density function for I_0 = 0.5, 1, 2.

4.3 Attenuation due to Atmospheric Turbulence

Atmospheric refractive index is greatly related to temperature, humidity and pressure.

However, it is found that the temperature has a more significant influence than the humidity and atmospheric pressure to the atmospheric index in the optical wave band [135]. As one of the most significant parameters of the atmosphere for optical wave propagation, the refractive index n is very sensitive to small-scale temperature fluctuations. In Eq. (4.4), the first term $n_0 = \langle n(r,t) \rangle \sim 1$ is the mean value, and the second term $n_1(r,t)$ is random deviation from its mean value due to spatial variation of pressure and temperature of the air.

The refractive index of air in the millimeter wave band up to a few hundred GHz can be well approximated as [136]

$$n_{mmW} = 1 + \frac{77.6}{T}\left[P_a + 4810 \frac{P_v}{T} \right] \times 10^{-6}, \tag{4.24}$$

where T, P_a, P_v stand for the temperature in kelvin, the atmospheric pressure in millibars, and the water vapor pressure in millibars, respectively. The water vapor pressure can be $P_v = \rho \mathrm{T}/216.7$ with water vapor density ρ in unit of g/m^3. Similarly, for IR wavelengths the refraction index of air can be written as [16]

$$n_{IR} = 1 + 79 \times 10^{-6} \frac{P_a}{T} \ . \tag{4.25}$$

In this formula, the pressure fluctuations are usually negligible, and the contribution of humidity in refractive index fluctuation is insignificant [137]. Therefore, the refractive index fluctuations in the range of THz and IR regions are mostly dependent on the random temperature fluctuations in clear weather conditions [108, 139].

A widely used parameter, which is called refractive index structure parameter (RISP) C_n^2,

is employed to characterize the atmospheric turbulence based on the altitude h of the atmosphere [138, 139].

$$C_n^2(h) = 0.005(v/27)^2 \left(10^{-5}h\right)^{10} \exp(-h/1000) + 2.7\times10^{-6} \exp(-h/1500) + \hat{\mathbf{A}} \exp(-h/100), \tag{4.26}$$

where $\hat{\mathbf{A}}$ is a normal value of $C_n^2(0)$ at the ground level in $m^{-2/3}$, and wind velocity $v \sim 21$ m/s. From Eq. (4.26), it is found that the parameter C_n^2 varies with h of the atmosphere and is almost considered to be constant for a horizontally propagating field. The typical average values of C_n^2 is 10^{-12} $m^{-2/3}$ -10^{-17} $m^{-2/3}$ for the strong to weak turbulence regimes, respectively [140]. Practically, C_n^2 is a measure of the strength of the fluctuations in the refractive index. The value of C_n^2 along the propagation path can be calculated by incorporating the temperature structure function C_T^2 and is given as [108, 141]:

$$C_n^2 = \left(\frac{dn_1}{dT}\right)^2 C_T^2. \tag{4.27}$$

The temperature difference is obtained from point measurement of the mean square temperature difference between two temperature sensors at two different points. This allows us to determine the parameter C_T^2 for any given length L using Eq. (4.2). The RISP C_n^2 can be inferred by using Eq. (4.27): in terms of power spectrum of refractive index fluctuations, the power spectral density for refractive index fluctuations over turbulence channel is given by [115, 142]

$$\Phi_n(k) = 0.033 C_n^2 k^{-11/3}, \qquad 2\pi/L_0 \ll k \ll 2\pi/l_0 , \tag{4.28}$$

where *k* is the spatial wave number and valid only for inertial sub-range defined in Eq. (4.28). In general, the spatial power spectrum of refractive index fluctuations is considered to be the same for temperature and velocity fluctuations. For a wide range of *k*, Eq. (4.28) is modified by Tatarskii and von Karman as given in [143].

Evaluate and characterize the turbulence based on theory is very challenging and complex. This is because the observable atmospheric channel quantities such as temperature, pressure, and wind velocity are mixed and behave in a nonlinear fashion. Therefore, the atmospheric turbulence can be simply expressed and characterized based on the statistical distributions e.g., probability distribution function (pdf) of received irradiance and its related properties. Two assumptions have been made to simplify the mathematics [144, 145]: (1) The atmospheric free space communication channel is non-dispersive for wave propagation. (2)The mean energy in the absence or presence of turbulence is the same. This assumption is true for spherical and plane waves. Note that, in general, a laser beam propagating over a long link span is mostly considered to be a plane wave [143].

Several models have been developed to describe the attenuation of atmospheric turbulence. The Rytov approximation and Andrew's method are widely employed for actual analysis.

4.3.1 Rytov Approximation

The Rytov approximation starts on the basis of Rytov's analysis [113]. The relationship between the refractive index structure parameter and relative variance of optical intensity

is shown in Eqs. (4.14) and (4.15). According to [146], the scintillation variance for a weak turbulence can be expressed as

$$\sigma_{\chi}^2 = 23.17 \cdot C_n^2 \cdot k^{7/6} \cdot L^{11/6} . \tag{4.29}$$

So, the attenuation due to scintillation is [147]

$$\alpha = 2\sigma_{\chi} = 2\sqrt{23.17 \cdot C_n^2 \cdot k^{7/6} \cdot L^{11/6}} . \tag{4.30}$$

However, the drawback for this method is that the effect of receiver aperture is not included which has a great influence on the turbulence study. This will be presented later.

4.3.2 Andrew's Method

Andrew's method is one of the more prominent approaches, which is derived on the basis of a detailed mathematical analysis of atmospheric turbulence presented by Larry C. Andrews [148]. The attenuation because of atmospheric turbulence can be expressed approximately on the basis of empirical experience [147, 149]

$$\alpha = 10 \cdot \log\left|1 - \sqrt{\sigma_I^2(D)}\right| , \tag{4.31}$$

where, σ_I^2 is the scintillation index defined by mean variance of optical intensity [103], which will be described in detail. D is the receiver diameter.

In the Forth-Order Statistics, based on the extended Rytov theory, the irradiance of the optical field can be

$$\hat{I} = \frac{I}{\langle I \rangle} = XY . \tag{4.32}$$

Here, X is from large-scale turbulence packet effects and Y is from small-scale turbulence packet effects. Then, according to Eq. (4.30), the second moment can be

$$\begin{aligned}\left\langle \hat{I}^2 \right\rangle &= \left\langle X^2 \right\rangle \left\langle Y^2 \right\rangle \\ &= \left(1+\sigma_X^2\right)\left(1+\sigma_Y^2\right)\end{aligned} \tag{4.33}$$

with σ_X^2 , σ_Y^2 being normalized variances of *X* and *Y*, respectively. Then the scintillation index can be a sum of three terms involving the normalized variances of large-scale and small-scale irradiance fluctuations:

$$\begin{aligned}\sigma_I^2 &= \frac{\left\langle I^2 \right\rangle}{\left\langle I \right\rangle^2} - 1 \\ &= \left\langle \hat{I}^2 \right\rangle - 1 \\ &= \left(1+\sigma_X^2\right)\left(1+\sigma_Y^2\right) - 1\end{aligned} \tag{4.34}$$

Under the Rytov approximation and considering the relation between the log amplitude variance and the scintillation index, the scintillation index can be expressed in the form

$$\sigma_I^2 = \exp\left(\sigma_{\ln X}^2 + \sigma_{\ln Y}^2\right) - 1, \tag{4.35}$$

where $\sigma_{\ln X}^2$ and $\sigma_{\ln Y}^2$ are large-scale and small-scale log-irradiance scintillations [108].

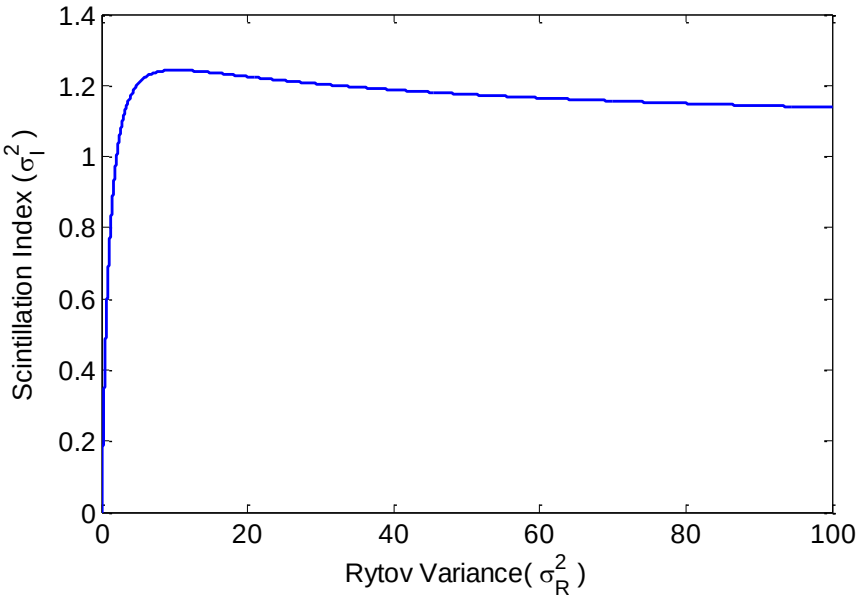

Figure 4.5 Scintillation index vs. Rytov variance for plane wave.

So, in the case of negligible inner scale l_0 and infinite outer scale L_0, the scintillation index for plane wave is

$$\sigma_I^2 = \exp\left[\frac{0.49\sigma_R^2}{\left(1+1.11\sigma_R^{12/5}\right)^{7/6}} + \frac{0.51\sigma_R^2}{\left(1+0.69\sigma_R^{12/5}\right)^{5/6}}\right] - 1, \qquad 0 \le \sigma_R^2 < \infty \ , \tag{4.36}$$

which is considered valid for all values of Rytov variance σ_R^2 (Eq. (4.14)) and is suitable under weak and strong scintillations.

Similarly, the scintillation index for spherical wave can be expressed as

$$\sigma_I^2 = \exp\left[\frac{0.49\sigma_R^2}{\left(1+0.56\sigma_R^{12/5}\right)^{7/6}} + \frac{0.51\sigma_R^2}{\left(1+0.69\sigma_R^{12/5}\right)^{5/6}}\right] - 1, \qquad 0 \le \sigma_R^2 < \infty \ . \tag{4.37}$$

Note that the Rytov variance σ_R^2 for plane and spherical waves is different in Eqs. (4.14, 4.15). The scintillation index with respect to scintillation strength (Rytov variance) for plane and spherical waves is plotted in Figure 4.5 and 4.6, which show that scintillation index reaches to a peak value as the scintillation strength increases, and then approaches the unity as the turbulence reaches the saturation regime.

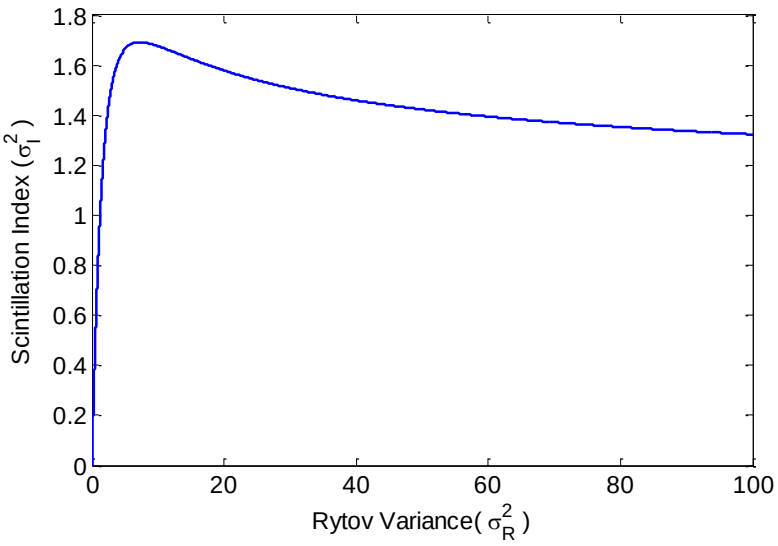

Figure 4.6 Scintillation index vs. Rytov variance for spherical wave.

4.4 Aperture Averaging

When calculating the scintillation index, the receiving aperture needs to be considered. The decrease of scintillation attributed to the increasing receiving area has been described previously [150]. So the aperture averaging effect, as the most valuable asset of Andrew's method, is considered in our theoretical model, which is intentionally used in direct detection systems to reduce scintillation and, consequently, increase the mean SNR.

Under general intensity fluctuation conditions and using the large-scale filter function

with both inner and outer scale parameters, the scintillation index for plane and spherical wave can be derived by considering the aperture averaging effect as

$$\sigma_I^2(D) = \exp\left[\frac{0.49\sigma_R^2}{\left(1+0.65d^2+1.11\sigma_R^{12/5}\right)^{7/6}} + \frac{0.51\sigma_R^2\left(1+0.69\sigma_R^{12/5}\right)^{-5/6}}{1+0.90d^2+0.62d^2\sigma_R^{12/5}}\right]-1, \quad \textit{plane wave},$$

(4.38)

$$\sigma_I^2(D) = \exp\left[\frac{0.49\sigma_R^2}{\left(1+0.18d^2+0.56\sigma_R^{12/5}\right)^{7/6}} + \frac{0.51\sigma_R^2\left(1+0.69\sigma_R^{12/5}\right)^{-5/6}}{1+0.90d^2+0.62d^2\sigma_R^{12/5}}\right]-1, \quad \textit{spherical wave}.$$

(4.39)

Here, $d=\sqrt{kD^2/4L}$, which contains information about the distance between the transmitter and receiver, wavelength of signal source and the receiver diameter D. In Figure 4.7 and 4.8, the scintillation index with respect to turbulence strength are plotted for $\lambda = 1550\,\text{nm}$, $L = 1\,\text{km}$ and aperture $D = 0, 1, 5, 10\,\text{mm}$. It can be seen that the aperture averaging effect can reduce the scintillation effect for both plane and spherical waves.

In the log-normal model, Rytov approximation is employed to characterize the atmospheric turbulence, which predicts that the Rytov variance is proportional to the path length L and the index of refraction structure parameter C_n^2. But this model is only suitable for the weak turbulence. For strong turbulence conditions, it fails due to the appearance of multiple scattering which cannot be accounted by the Rytov approximation [71, 108]. Turbulence ranging from weak to strong conditions can be described by Gamma-gamma models due to its assumption that the fluctuation of laser intensity

consists of large scale (refraction) and small scale (scattering) effects [126]. Besides, the I-K model and Beckmann model are also good candidates for weak to strong turbulence conditions.

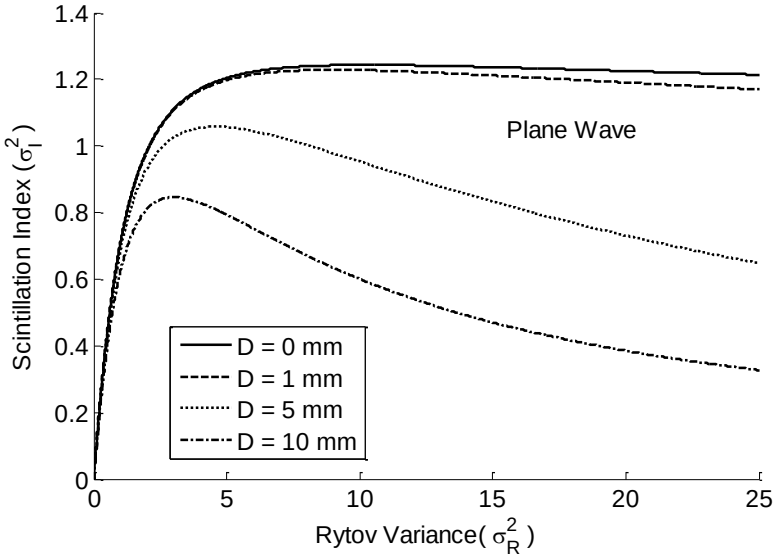

Figure 4.7 Scintillation index of a plane wave vs. Rytov variance with different aperture diameters. (wavelength 1550nm, L = 1km).

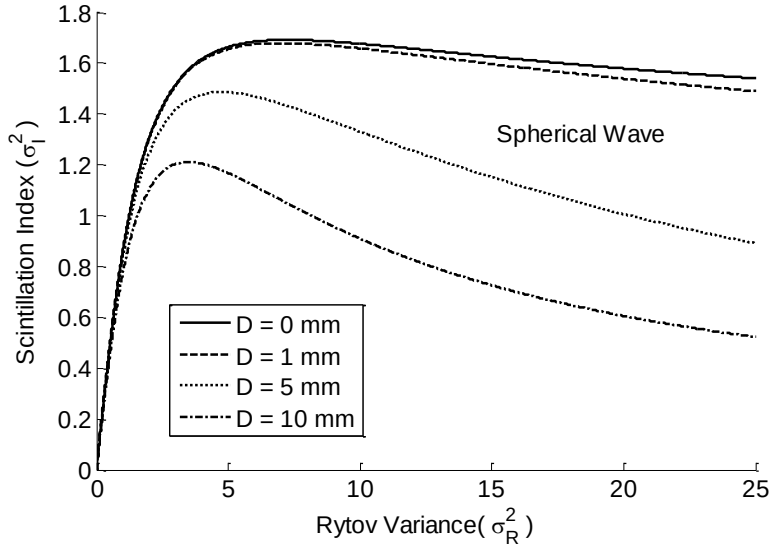

Figure 4.8 Scintillation index of a spherical wave vs. Rytov variance with different aperture diameters. (wavelength 1550nm, L = 1km).

4.5 Beam Spreading

The spot width of a laser beam propagating through turbulences can be related to the Rytov variance σ_R^2. The refractive index fluctuations cause beam spreading beyond the intrinsic laser beam divergence. The relationship between the mean intensity over time of the beam propagating through the turbulence can be expressed as

$$\left\langle I\left(\mathbf{r},L\right)\right\rangle = \frac{W_0^2}{W_e^2}\exp\left(-\frac{2r^2}{W_e^2}\right), \tag{4.40}$$

where W_0 is beam radius at the transmitter, **r** is the distance from the spot center, and W_e is the effective long-term averaged beam radius in free space at the receiver given by

$$W_e = W\sqrt{1+1.33\sigma_R^2\Lambda^{5/6}}, \tag{4.41}$$

where W is the beam radius at the receiver for an unperturbed channel. Λ is the Fresnel ratio of the beam at the receiver.

4.6 Summary

In this chapter, atmospheric turbulence is introduced briefly and some effects of the turbulence are listed. Kolmogrov theory, which is discussed in this chapter, is mainly based on the classical studies of temperature, velocity, fluctuation of index of refraction and statistical modeling of signal power fluctuation induced by atmospheric turbulence. This theory has been well established and studied to describe and analyze various effects

of the atmospheric turbulence on the wireless signal propagation. Based on this method, the atmospheric turbulence can be categorized in strength from weak to strong [99, 158], which is dependent on the refractive index variation, temperature inhomogeneities and propagation distance through the atmosphere. The theoretical models can be classified to log-normal, gamma-Gamma, K-distributed and negative exponential models based on the statistical distribution of the random fading irradiance signals. These four models corresponds to weak, weak-to-strong, strong and saturation regimes, respectively [123, 151, 152]. The log-normal model is employed and verified experimentally for the characterization of atmospheric turbulence. Aperture averaging effect is analyzed, which can reduce the scintillation effect and increase the mean SNR.

CHAPTER 5

RAIN THEORIES

Rain has long been recognized as one of important reasons for unwanted performance degradation in sensing, imaging and communication systems using THz waves above 300GHz due to its strong unavoidable interaction with water molecules.

5.1 Rain Introduction

Rain is formed due to the precipitation of water vapor in atmosphere. The formation process occurs mainly in two different ways based on warm or cold cloud. Raindrops are created by condensation, collision and coalescence in warm clouds, where raindrops with approximate radius of 10 μm are generated by condensation. The larger raindrops are created by collision and coalescence. A cloud which exists above the zero-degree isotherm level is typically called a cold cloud, where ice crystals and super-cooled water droplets are contained. In cold clouds, rain can be formed by vapor, riming or aggregation. Ice crystal growth by riming and aggregation can produce a wide range of particles sizes, which melt to create larger raindrops.

Raindrops vary in both shape and size [153]. A spherical shape for a rain drop is assumed due to the surface tension of water when there is no noticeable motion relative to the surrounding air. That’s because the inside spherical pressure due to the surface tension of the rain drop is greater than the atmosphere. However, when it drops, the pressure, decrease at the top and sides, and increase at the bottom of the drop, and also the increased air resistance deforms the water drop by spreading the shape sideways and flattening the bottom surface. In References [154, 155], it is found that raindrop with

diameter larger than 2.0 mm suffers the effect due to the pressure difference on the outside of the drop and becomes oblate spherical in shape. The different types of raindrop shapes for given sizes is shown in Figure 5.1. However, in our setup, due to the very small velocity of the rain drops when they reach the laser beam, it is assumed the pressure difference on different surface sides is negligible and so the raindrops are spherical.

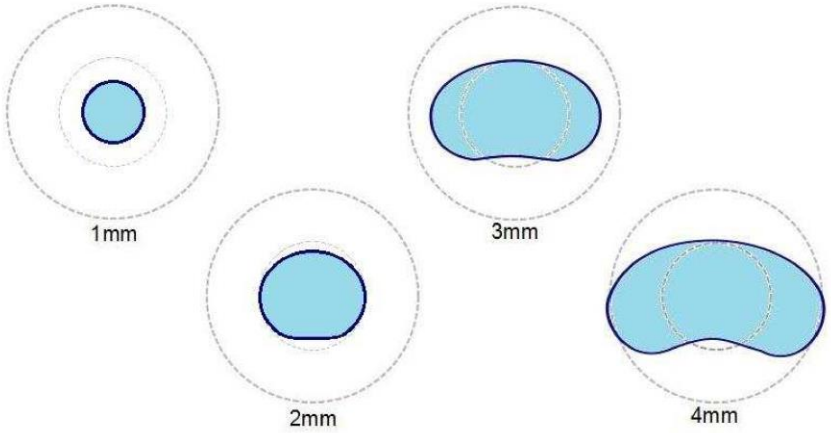

Figure 5.1 Equilibrium raindrop shapes at radius: 1 mm, 2 mm, 3 mm and 4 mm. Source: [155].

5.2 Raindrop Size Distribution

The raindrop size distribution (DSD) is defined as the number concentration of raindrops with diameter D in a given volume of space. Denoted by N (D) with unit $m^{-3}mm^{-1}$, it can be used to calculate rain attenuation and rain rate by employing a suitable model. Many raindrop size distributions for rain have been investigated, such as exponential distribution [156], log-normal distribution [157], gamma distribution [158] and the normalized gamma distribution [159].

5.2.1 Exponential Distribution

The work on raindrop size distribution was first started by Laws and Parsons [160], and then continued by Marshall and Palmer [156] by measuring raindrops on dyed filter paper to analyze the raindrop distribution. By fitting their data, the famous empirical equation is proposed as

$$N(D) = N_0 \exp(-\Lambda D). \tag{5.1}$$

Here D refers to the raindrop diameter in mm. $N_0 = 8000 m^{-3} mm^{-1}$ and $\Lambda = 4.1 R^{-0.21} mm^{-1}$ are parameters of distribution with R as the rain rate in mm/hr. $N(D)$ is the number density of raindrops of diameter D in a unit volume. This distribution of raindrop size is shown in Figure 5.2 for rain rate of 0.25, 1, 5, 25 and 100 mm/hr. However, the drawback for this distribution is that it is not in very good agreement with the experimental points for drops less than D = 1 mm.

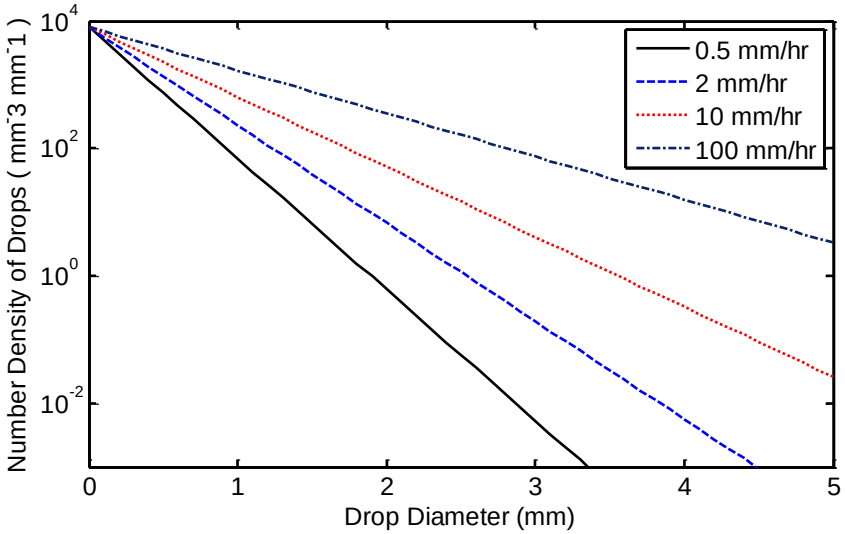

Figure 5.2 Marshall and Palmer raindrop size distribution.

A similar form is obtained by Joss, Thams and Waldvogel [161] by measuring the raindrop-size distribution using a distrometer in Switzerland. The constants N_0 and Λ in the equation differ for drizzle, widespread and thunderstorm rain cases as shown in Table 5.1. J-D, J-W and J-T represent different types of rain of drizzle, widespread and thunderstorm.

Table 5.1 Parameters for Exponential Distribution. J-D: Joss drizzle distribution; J-W: Joss widespread distribution; J-T: Joss thunderstorm distribution

Type of Rain	N_0 **m^{-3}mm^{-1}**	Λ **mm^{-1}**
Drizzle [J-D]	30000	$5.7R^{-0.21}$
Widespread [J-W]	7000	$4.1R^{-0.21}$
Thunderstorm [J-T]	1400	$3.0R^{-0.21}$

Source: [16]

5.2.2 Log-normal Distribution

The log-normal distribution, given in Eq. (5.2) can better estimate the raindrop size distribution because there are a fewer number of small raindrops considered. The distribution under different rain rates is shown in Figure 5.3, where the log-normal distribution has more flexibility in representing different drop distributions for a given rain rate when compared with exponential distribution in Figure 5.2.

$$N(\mathrm{D}) = \frac{N_t}{\sqrt{2\pi}\ln\sigma D}\exp\left[\frac{-\ln^2\left(D/\bar{D}\right)}{2\ln^2\sigma}\right], \tag{5.2}$$

where N_t refers to total raindrop number in a unit volume, σ is the standard geometric deviation, and $\bar{D}$ indicates the geometric mean diameter.

5.2.3 Gamma Distribution

The gamma distribution, which improves the estimation accuracy of raindrop size distribution, especially at high rain rates, was investigated by Ulbrich. It can be expressed as

$$N(D) = N_0 D^{\mu} \exp(-\Lambda D). \tag{5.3}$$

where Λ refers to a parameter of distribution, μ is the shape parameter and $N(D)$ is in $\mathrm{m}^{-3}\mathrm{cm}^{-1-\mu}$. The effect of the shape parameter on the raindrop size distribution is shown in Figure 5.4.

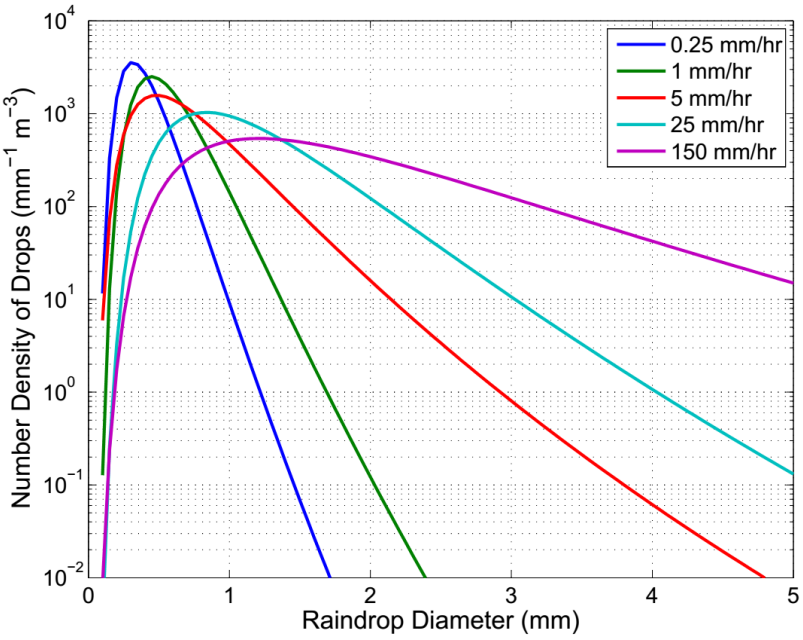

Figure 5.3 Log-normal raindrop size distribution.
Source: [200]

Table 5.2 Parameters for Gamma Distribution

Type of Rain	N_0 $m^{-3}mm^{-1}$	Λ mm^{-1}
Thawing of Pellets (Hail)	$64500R^{-0.5}$	$5.7R^{-0.27}$
Thawing of Granular Snow (Sleet)	$11750R^{-0.29}$	$4.1R^{-0.2}$
Thawing of Non Granular Snow (Sleet)	$2820R^{-0.18}$	$3.0R^{-0.19}$

Source:[165]

One case of gamma distribution as shown in Eq. (5.4) is proposed by Litovinov [162, 164] by using the Russian data for all three types of rain. This model was also described by Krasyuk, Rozenberg and Chistyakov and by University of Tennessee [164, 165].

$$N(D) = N_0 D^2 \exp(-\Lambda D). \tag{5.4}$$

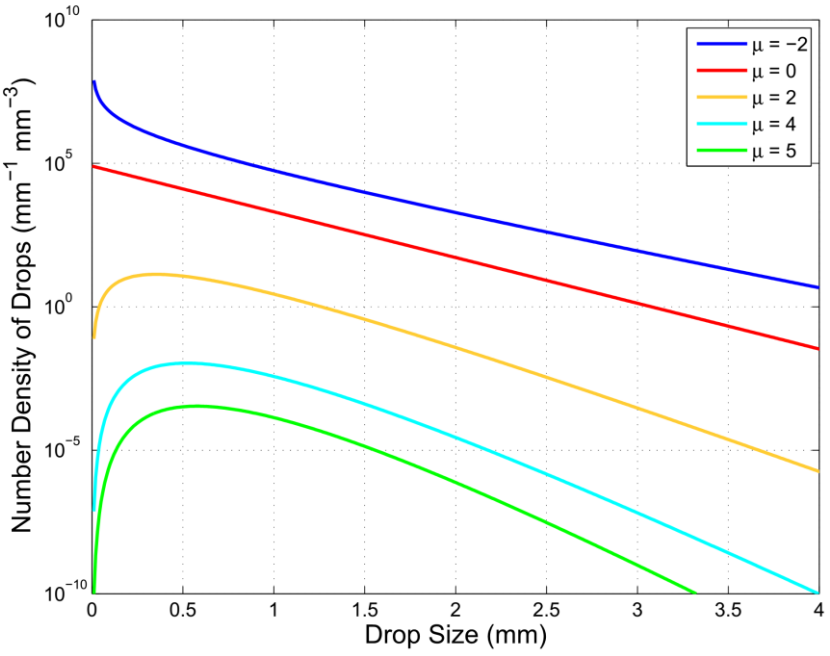

Figure 5.4 Gamma raindrop size distribution.
Source: [165]

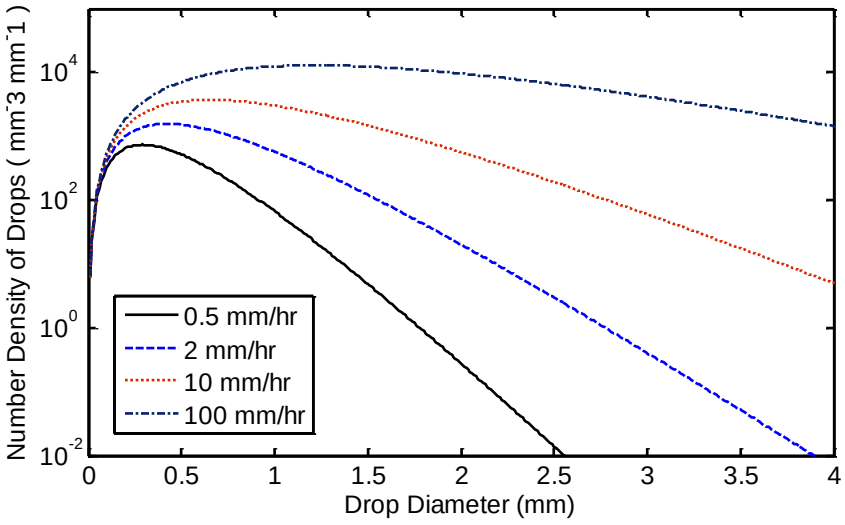

Figure 5.5 Gamma raindrop size distribution. (Type of rain - Thawing of Pellets (Hail)).

5.2.4 Normalized Gamma Distribution

The normalized gamma distribution is first defined by Willis by three parameters μ, N_ω and D_m [166] and later presented by Montopoli [167] as

$$N(D) = N_\omega \cdot \frac{6}{4^4} \cdot \left[\frac{(4+\mu)^{(4+\mu)}}{\Gamma(4+\mu)} \right] \cdot \left(\frac{D}{D_m} \right)^{\mu} \cdot \exp\left[-(4+\mu) \cdot \frac{D}{D_m} \right] . \quad (5.5)$$

This distribution is the present best fit to a wide variety of raindrop size distribution as shown in [159]. The effects of a variety of changes in the distribution parameters on the raindrop distribution is shown in Figure 5.6.

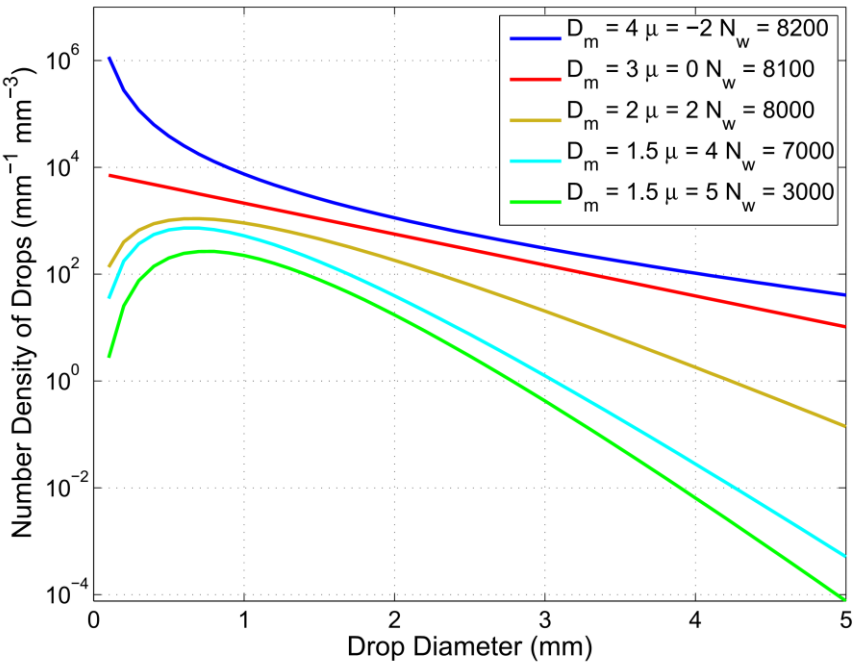

Figure 5.6 Normalized Gamma raindrop size distribution.
Source: [159]

5.3 Rain Rate

Rain rate, related to the raindrop size distribution, is used to express the amount of rain over a given time. It is defined by Baltas as [168]

$$R = \frac{3.6}{10^3} \cdot \frac{\pi}{6} \cdot \int_0^\infty v(D) D^3 N(D)\, dD, \tag{5.6}$$

where R indicates the rain rate, $N(D)$ refers to the raindrop size distribution, D is the raindrop diameter and $v(D)$ is the rain fall velocity. Rain rate is proportional to the raindrop size distribution of order at a given time [167]. Atlas assumed that the fall velocity $v(D) = 3.78 D^{0.67}$ [169]. The general expression of the nth order raindrop size

distribution can be expressed as

$$m_n(t) = \int_0^{\infty} D^n \cdot N(D,t)\, dD = \sum_{i=1}^{n_c} D_i^n \cdot N_m(D_i,t) \cdot \Delta D_i \,. \tag{5.7}$$

The following expression shows that the rain rate is proportional to the raindrop size distribution of the order 3.67

$$R = 3.78 \cdot \frac{\pi}{6} \cdot m_{3.67}(t) \,. \tag{5.8}$$

During a long time period, a rain event may vary considerably. Rain rate measurement over such a long time interval effectively averages the rain rate. So, small time intervals (such as 1 minute) will represent more variations in the rain event. Rain rate can be measured over different time intervals. The rain rate is calculated by averaging the experimental 1-min rain rate measurements at different positions and is expressed in mm/hr to make facilitate comparisons with other technical reports [170].

5.4 Attenuation by Rain

Absorption and scattering of electromagnetic waves are the main reasons for the attenuation in wireless communication links. If a plane wave with field E_i propagates in direction $\hat{\mathbf{K}}_1$ and incident on a raindrop at the origin, it will induces a transmitted field inside the drop and a scattered field E_s towards direction $\hat{\mathbf{K}}_2$ [171].

$$E_s = f\left(\hat{\mathbf{K}}_1, \hat{\mathbf{K}}_2\right) \frac{\exp(-ikr)}{r} E_i \,, \tag{5.9}$$

where r is the distance from the origin to the observation point, $k = 2\pi/\lambda$ is the free space propagation constant and λ is the incident wavelength. $f\left(\hat{\mathbf{K}}_1, \mathbf{K}_2\right)$, obtained from the solution of the boundary value, refers to a matrix function denoting scattering amplitude and the polarization state of the scattered wave. Therefore the scattering amplitude is related to $\hat{\mathbf{K}}_1$, $\hat{\mathbf{K}}_2$, frequency, size, material, shape of the raindrop, and polarization of the incident wave. The raindrop and fields are shown graphically in Figure 5.7.

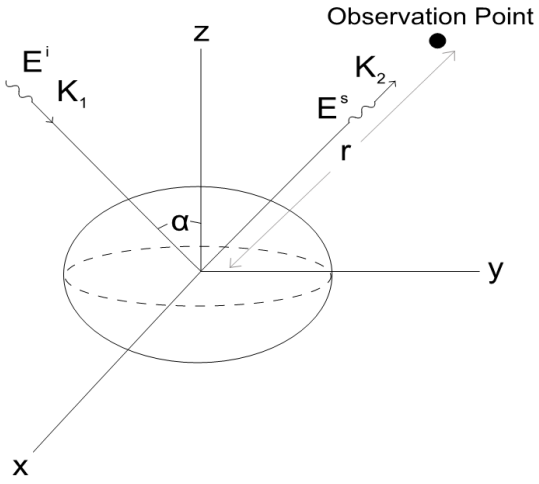

Figure 5.7 Electromagnetic scattering geometry.
Source: [171]

Absorption, scattering and total extinction cross sections are always considered for a raindrop [172-174]. Q_a, the absorption extinction cross section, represents the power absorbed by the raindrop, and Q_s, the scattering extinction cross section, represents the power scattered in all directions. Q_t, the total extinction cross section is directly related to attenuation of the transmitted signal and can be expressed as

$$Q_t = -\left(4\pi/k\right)\mathrm{Im}\left[\hat{e},\, f\left(\mathbf{K}_1^{\text{资}}, \mathbf{K}_2\right)\right], \tag{5.10}$$

where $\hat{e}$ is a unit vector of the polarization state. $\mathbf{K}_1^{\text{资}} = \mathbf{K}_2$ can be considered when there is only forward scattering. The absorption and scattering can be modelled by several different methods such as Mie scattering, Rayleigh approximation, depending on the frequency of the signal and the shape of the raindrop.

As mentioned in Section 2.3, when gas molecules absorb the photons propagating in the atmosphere, absorption occurs [175]. Due to the interactions between photons and molecules, absorption, as a quantum effect, is highly wavelength dependent. The collision between gas molecules and photons propagating in the atmosphere leads to scattering effect, where the direction of the photons will be altered with or without modification of its wavelength. With the change in photon direction, the energy of a laser beam would be partially dispersed and deflected from detector's solid angle field of view (FOV).

Mie first considered a dielectric sphere with arbitrary radius *r* to solve for the scattering and absorption of electromagnetic waves [176]. Ishimaru then restated his derivation and formulated it by using two parameters - the relative index of refraction *n* and the normalized circumference χ [177]

$$\chi = k_b r = \frac{2\pi r}{\lambda_b} = \frac{2\pi r}{\lambda_0}\sqrt{\varepsilon_b'}, \tag{5.11a}$$

$$n = \frac{n_p}{n_b} = \left(\frac{\varepsilon_p}{\varepsilon_b}\right)^{1/2} = \varepsilon^{1/2}, \tag{5.11b}$$

where k_b and λ_b are the wave number and wavelength in the background medium. λ_0 is

the wavelength in free space. $\varepsilon_b^{'}$ is the real part of the relative dielectric constant of the background medium. n_p and n_b are the complex indices of refraction of the particle material and of the background medium, respectively, and ε_p and ε_b are the corresponding complex dielectric constants. $\varepsilon_b^{'}=1$, $n_b=1$ when the background medium is air.

The results of Mie's solution lead to expressions for the scattering and extinction efficiencies of the sphere in the form of converging series, given by

$$\xi_s\left(n,\chi\right)=\frac{2}{\chi^2}\sum_{l=1}^{\infty}\left(2l+1\right)\left(\left|a_l\right|^2+\left|b_l\right|^2\right), \tag{5.12a}$$

$$\xi_e\left(n,\chi\right)=\frac{2}{\chi^2}\sum_{l=1}^{\infty}\left(2l+1\right)\mathrm{Re}\left(a_l+b_l\right), \tag{5.12b}$$

where a_l and b_l as functions of n and χ, are Mie coefficients.

If the particle size is much smaller than the wavelength of the incident wave $\left|n\chi\right|<<1$, the Mie expression for Eq. (5.12) can be reduced to simple expressions known as Rayleigh approximation [178].

5.5 Dielectric Constant of Water

Currently, the double-debye dielectric model (D3M) is the most accurate model for computing the dielectric constant of water. This model was first developed by William Ellison for sea water [179] and can also be reduced to a model for pure water when the water salinity is set to zero.

$$\varepsilon_W^{'} = \varepsilon_{W\infty} + \frac{\varepsilon_{W0} - \varepsilon_{W1}}{1+\left(2\pi f \tau_{W1}\right)^2} + \frac{\varepsilon_{W1} - \varepsilon_{W\infty}}{1+\left(2\pi f \tau_{W2}\right)^2}, \tag{5.13}$$

$$\varepsilon_W^{"} = \frac{2\pi f \tau_{W1}\left(\varepsilon_{W0} - \varepsilon_{W1}\right)}{1+\left(2\pi f \tau_{W1}\right)^2} + \frac{2\pi f \tau_{W2}\left(\varepsilon_{W1} - \varepsilon_{W\infty}\right)}{1+\left(2\pi f \tau_{W2}\right)^2} + \frac{\sigma_i}{2\pi\varepsilon_0 f}, \tag{5.14}$$

where ε_0 is the permittivity of free space. The expression contains two relaxation terms, one with a relaxation time constant τ_{W1} and another with τ_{W2}. The parameter functions are

$$\varepsilon_{W0} = 87.85306 \exp\left\{-0.00456992T - a_1 T - a_2 S^2 - a_3 ST\right\}, \tag{5.15a}$$

$$\varepsilon_{W1} = a_4 \exp\left\{-a_5 T - a_6 T - a_7 ST\right\}, \tag{5.15b}$$

$$\tau_{W1} = \left(a_8 + a_9 S\right) \exp\left(\frac{a_{10}}{T + a_{11}}\right) \text{ ns}, \tag{5.15c}$$

$$\tau_{W2} = \left(a_{12} + a_{13} S\right) \exp\left(\frac{a_{14}}{T + a_{15}}\right) \text{ ns}, \tag{5.15d}$$

$$\varepsilon_{W\infty} = a_{16} + a_{17} T + a_{18} S, \tag{5.15e}$$

$$\sigma_i = \sigma\left(T, 35\right) \cdot P\left(S\right) \cdot Q\left(T, S\right), \tag{5.15f}$$

where

$$\sigma\left(T, 35\right) = 2.903602 + 8.607 \cdot 10^{-2} T + 4.738817 \cdot 10^{-4} T^2 - 2.991 \cdot 10^{-6} T^3 + 4.3041 \cdot 10^{-9} T^4, \tag{5.15g}$$

$$P(S) = S\,\frac{37.5109 + 5.45216S + 0.014409S^2}{1004.75 + 182.283S + S^2}, \tag{5.15h}$$

$$Q(T,S) = 1 + \frac{a_0(T-15)}{T + \alpha_1}, \tag{5.15i}$$

$$a_0 = \frac{6.9431 + 3.2841S - 0.099486S^2}{84.85 + 69.024S + S^2}, \tag{5.15j}$$

$$\alpha_1 = 49.843 - 0.2276S + 0.00198S^2. \tag{5.15k}$$

Coefficients a_1 to a_{18} are listed in Table 5.3. According to Ellison, this semi-expirical model represents the dielectric constant "of pure water to within 1% over the frequency range 0-20GHz, to within 3% over the frequency range 30-100GHz, and to within 5% over 100-1000GHz."

Table 5.3 Values of Coefficients for Double-debye Dielectric Model

$a_1 = 0.46606917\times10^{-2}$	$a_{10} = 0.58366888\times10^{3}$
$a_2 = -0.26087876\times10^{-4}$	$a_{11} = 0.12684992\times10^{3}$
$a_3 = -0.63926782\times10^{-5}$	$a_{12} = 0.69227972\times10^{-4}$
$a_4 = 0.63000075\times10^{1}$	$a_{13} = 0.38957681\times10^{-6}$
$a_5 = 0.26242021\times10^{-2}$	$a_{14} = 0.30742330\times10^{3}$
$a_6 = -0.42984155\times10^{-2}$	$a_{15} = 0.12634992\times10^{3}$
$a_7 = 0.34414691\times10^{-4}$	$a_{16} = 0.37245044\times10^{1}$
$a_8 = 0.17667420\times10^{-3}$	$a_{17} = 0.92609781\times10^{-2}$
$a_9 = -0.20491560\times10^{-6}$	$a_{18} = -0.26093754\times10^{-1}$

Source: [201]

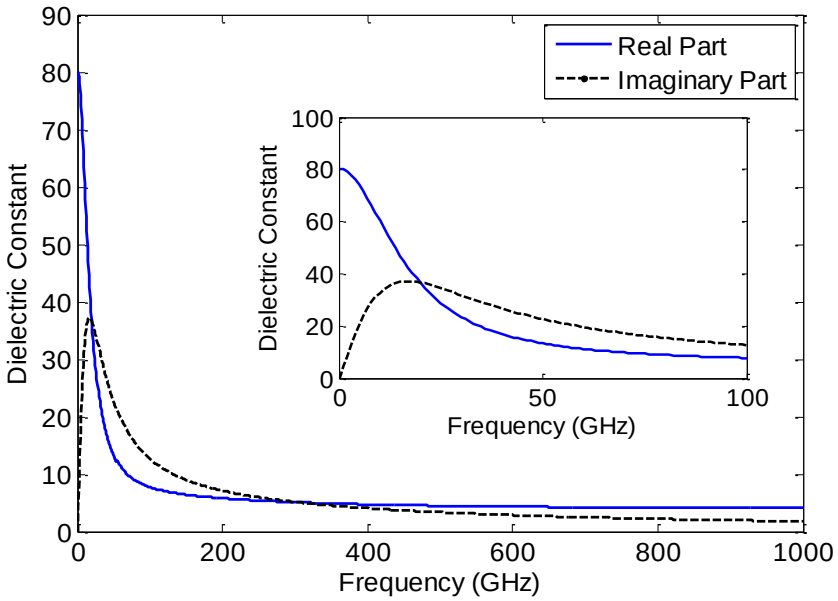

Figure 5.8 Spectrum of the permittivity (real part) and dielectric loss factor (imaginary part) of pure water at 20^{o}C.

The frequency responses of permittivity and loss factor of pure water based on Eqs.(5.13) and (5.14) are shown in Figure 5.8, where the same general shape are observed for both spectrum plots. There is a maximum loss at 16.7 GHz. Based on this plot, it is easy to conclude that the attenuation spectrum due to water will have the same shape as the imaginary curve.

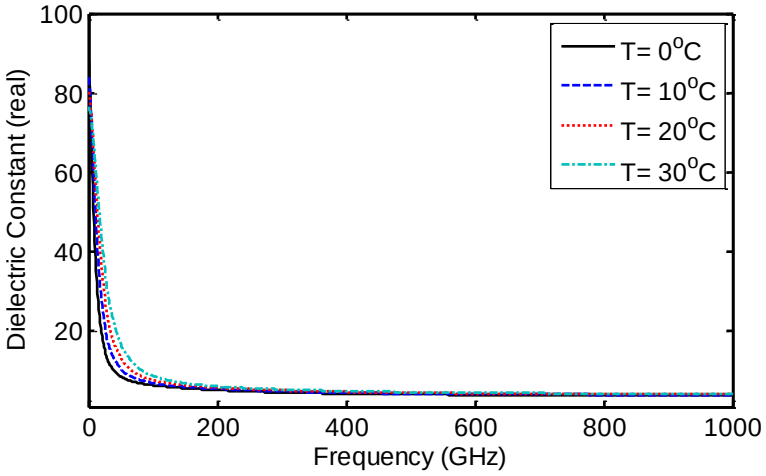

(a)

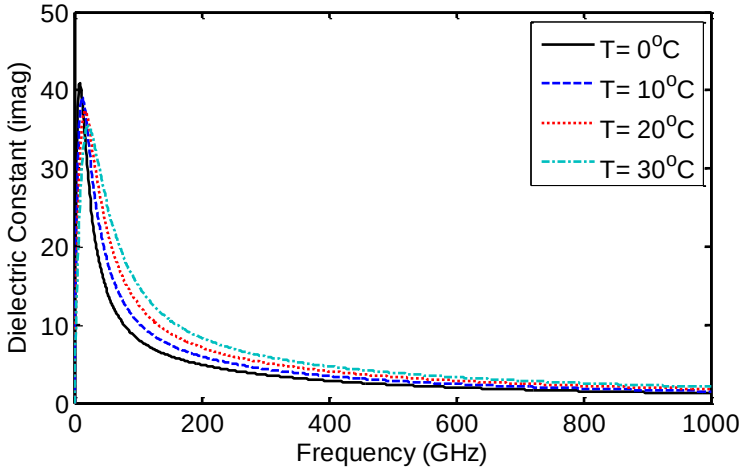

(b)

Figure 5.9 (a) Spectrum of the permittivity (real part) and (b) dielectric loss factor (imaginary part) of pure water at different temperatures.

The symbol ε refers to the average relative dielectric constant of the material under consideration. In general, ε as a complex, consists of a real part $\varepsilon^{'}$ and an imaginary part $\varepsilon^{''}$,

$$\varepsilon = \varepsilon^{'} - j\varepsilon^{''}, \tag{5.16}$$

where ε' is the relative permittivity of the material and ε'' is its dielectric loss factor. The dielectric constant ε is related to the complex index of refraction n through $\varepsilon = n^2$ with n defined as

$$n = n' - jn'' . \tag{5.17}$$

It follows that

$$\varepsilon' = \left(n'\right)^2 - \left(n''\right)^2 , \ \varepsilon'' = 2n'n'' , \tag{5.18}$$

and, conversely

$$n' = \mathrm{Re}\left\{\sqrt{\varepsilon}\right\}, \ n'' = -\mathrm{Im}\left\{\sqrt{\varepsilon}\right\} . \tag{5.19}$$

For a given raindrop size distribution $p(r)$ with r as the radius of the raindrop radius, the attenuation coefficient α in dB/km can be determined by integrating over all the raindrop sizes as

$$\alpha = 3.3429 \int_0^\infty p\left(r\right) \xi_e\left(r\right) \cdot \pi r^2 dr . \tag{5.20}$$

Figure 5.10 shows the simulated attenuation spectrum due to rain with Marshall and Palmer raindrop distribution based on Eq. (5.20).

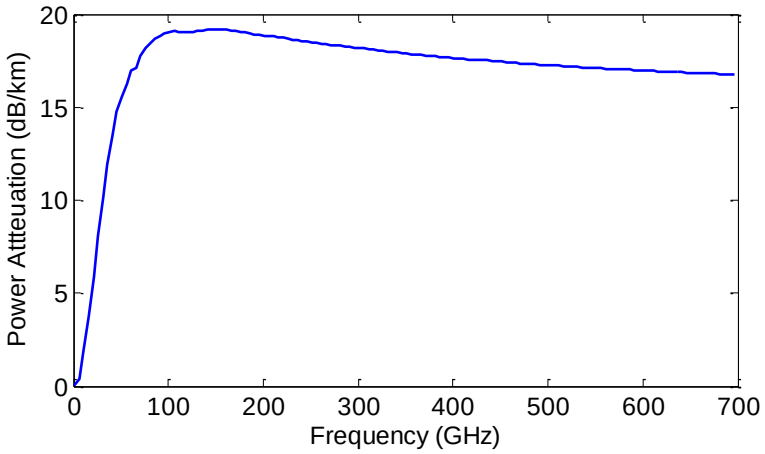

Figure 5.10 Attenuation spectrum due to rain at 20^{o}C.

5.6 Summary

A brief introduction of rain is described. Many raindrop size distributions for rain are presented, such as exponential distribution, log-normal distribution, gamma distribution and normalized gamma distribution. Theory of attenuation by rain caused by absorption and scattering is shown. Absorption, as a quantum effect and being highly wavelength dependent, occurs due to the absorption of light photon by the gas molecule in the atmosphere. Scattering occurs when the photons are deflected because of the collisions between photons and gas molecules. The Double-debye model is employed for the computing of the dielectric constant of water. A simulated attenuation spectrum due to rain by using Marshall and Palmer raindrop distribution is shown.

CHAPTER 6

EXPERIMENTAL AND SIMULATING RESULTS IN ATMOSPHERIC TURBULENCE

Practically, it is a hard work to measure and analyze the effect of atmospheric turbulences on communication channels due to the required long observation waiting time and the difficulty of obtain some reoccurrence of the different atmospheric conditions. So a turbulence chamber was built in laboratory to simulate the atmospheric turbulence and investigate its effects on the THz and IR communication links under controlled and reproducible lab conditions.

The THz and IR communications lab setup with a maximum data rate of 2.5 Gb/s at 625 GHz carrier frequency and 1550nm wavelength has been previously described in Chapter 2. It allows for simultaneous recording and analysis of performance degradations in both channels due to the same atmospheric turbulence. Figure6.1 shows a block diagram of the experimental setup. An iris is inserted concentrically into the beam to limit the total received power to an amount that results in a bit-error-rate (BER) of about 10^{-6} for an unloaded turbulence chamber. The initial BER is adjusted to that level because then statistical BER fluctuations do not significantly impact conclusions that drawn from the measurement results. Also, a BER of 10^{-6} is a typical threshold for modern forward error correction technology used in lightwave communication systems [180].

The experiments were carried out under total dark environment to reduce the effect of ambient light.

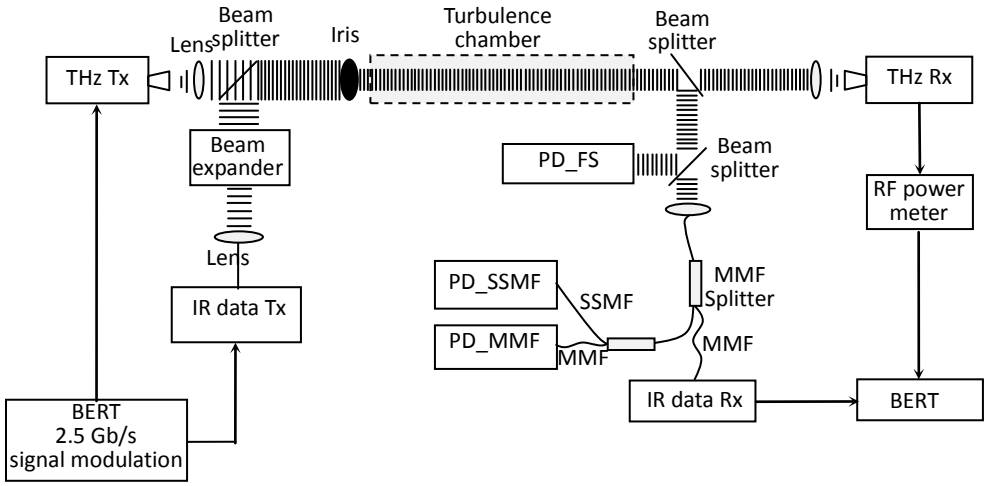

Figure 6.1 Schematic diagram of the THz and IR wireless communication testbed.

6.1 Experimental Results in Atmospheric Turbulence

In Figure 6.2, three thermistors are positioned inside the chamber which allows us to measure the temperature evolution. For technical reasons the sensors are located a few centimeters below the beam path but do not block them. Each sensor has a thermal response time τ ~3s, thus no rapid temperature fluctuations of the environmental air can be traced. The temperature of the air launched into the chamber can be set to 32^{o}C (cold), 55^{o}C (warm), and 70^{o}C (hot) and airspeeds of 28.6 m/s (low) and 41.6 m/s (high) can be independently adjusted. This parameter set enables the generation of air turbulence that is strong enough to obtain minimal-detectable degradations in the THz channel and weak enough to cause medium-strong scatter effects in the IR signal.

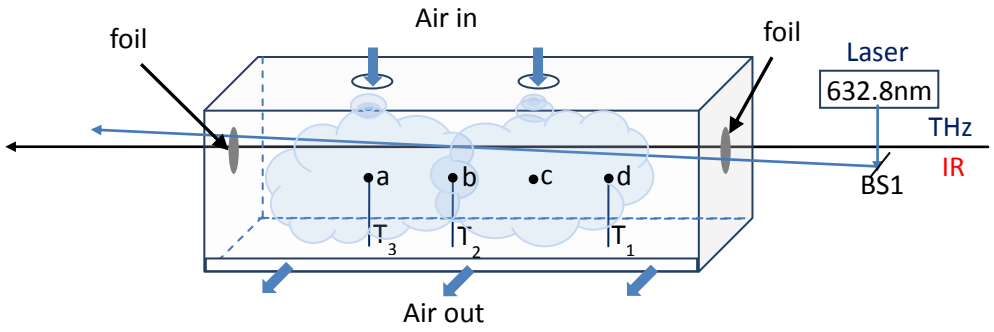

Figure 6.2 Schematics of a turbulence chamber setup to characterize turbulences. (L_{ab}=L_{bc}=L_{cd}=15cm).

6.1.1 Acoustic Noise Analysis

It is found that the air flow was partially leaking outside of the chamber and acoustical noise from the fans caused vibrations of the mirrors and beam splitters that form the interferometer for the visible light. Therefore the holes through which the beams enter and leave the chamber are covered with transparent foil polyvinylidene chloride (PVDC) (20um thick). In Figure 6.3, the power spectrums under different weather conditions are shown with and without foils covered. It can be seen that the power collected is reduced when foils are used. That means the vibration noise is reduced due to the foil. In Figure 6.4, the total powers under different weather conditions are compared. Here, it could be further verified that the foil reduces the vibrations of the optical components, but there was still some residual impact from residual acoustical waves.

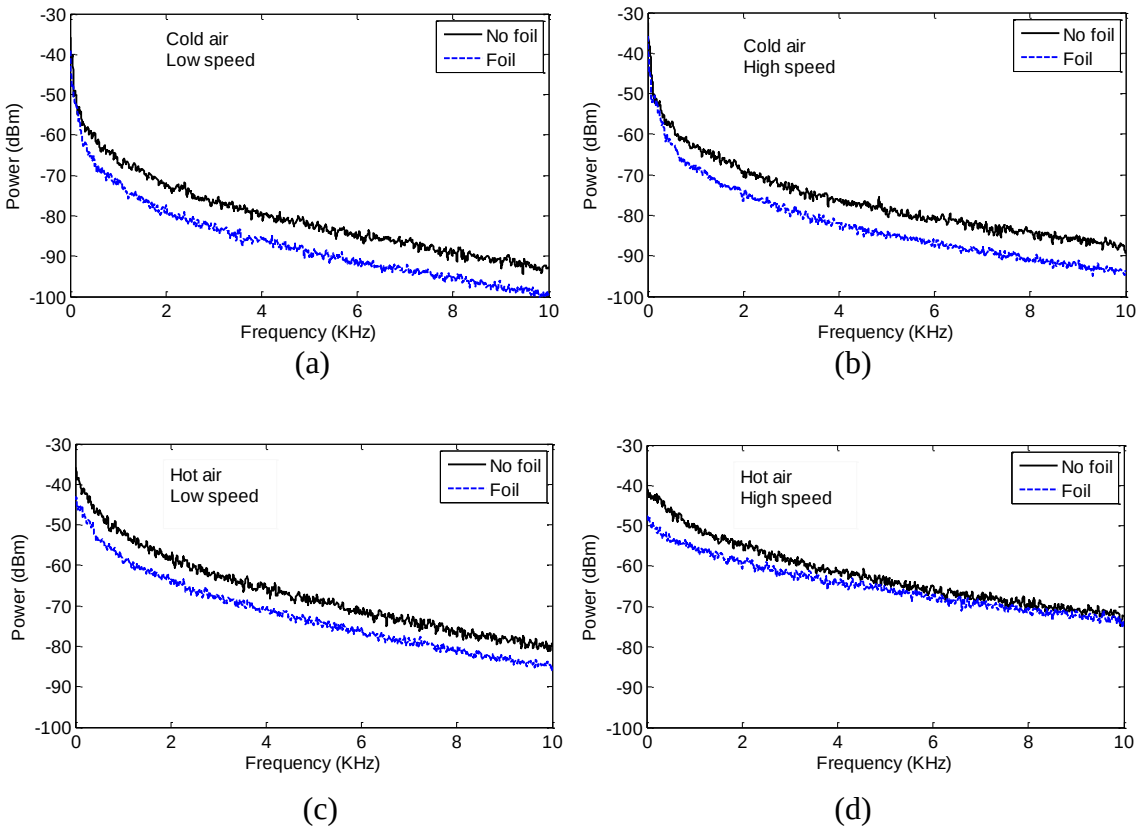

Figure 6.3 Power spectrum detected from D1 in Mach-Zehnder Interferometer at different turbulence conditions with and without foil covers.

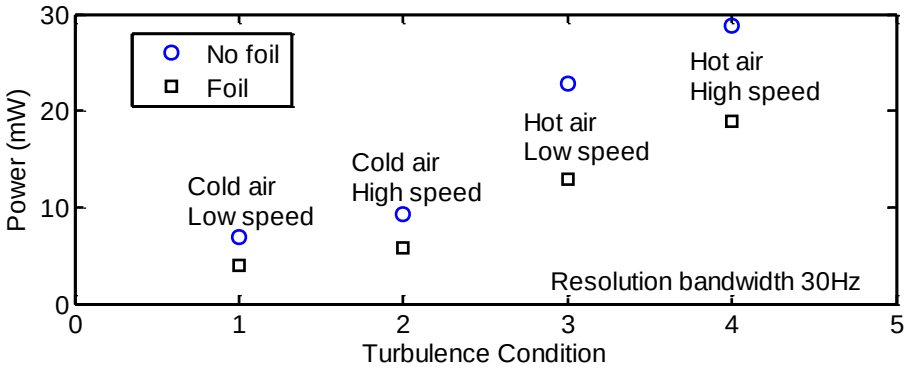

Figure 6.4 RF-power at the output of D1 in Mach-Zehnder Interferometer at different turbulence conditions with and without foil covers phase change in the chamber detected with D1 and D2.

In Figure 6.5, the power spectrums under different weather condition are recorded with foil covers. One can see that the total power is higher for higher temperature and higher air speed. This means that there is more power for the air with higher turbulence strength which is related to temperature and air speed.

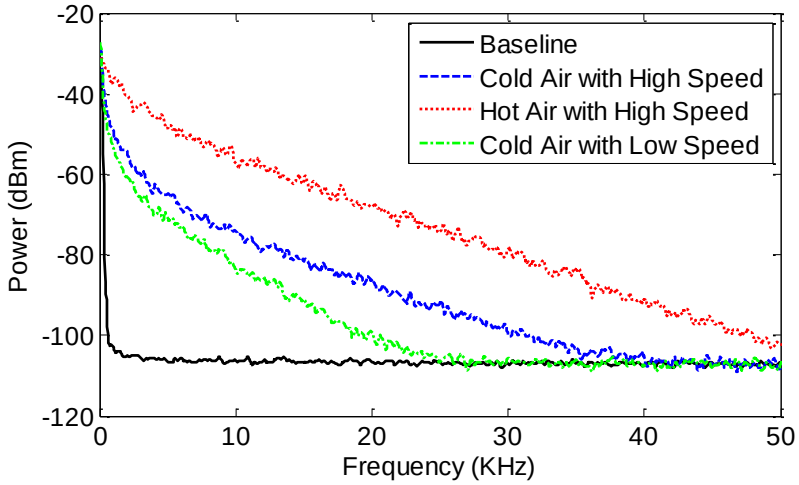

Figure 6.5 Power spectrum detected from D1 in Mach-Zehnder Interferometer at different turbulence conditions with foil covers.

6.1.2 Attenuation and BER Performance

After air is launched into the turbulence chamber, a typical evolution of the attenuations in the THz and IR channels becomes visible as shown in Figure 6.6 (a) for the PD_MMF. Ten seconds after initiating the recording, hot air is launched with high speed into the propagation path of the beams. The IR beam breaks up into a speckle pattern at the receiver side. Depending on the receiver aperture these speckle effects become more or less visible by the fluctuation strength of the detected IR power. For the PD_MMF, the time-averaged (500ms) maximum attenuation of the IR light (around 1dB) is clearly evident while the impact on THz signal is small (0.015dB), but above the detection sensitivity limit. After the air-supply is powered off at 20 seconds recording time, the

transmitted IR power recovers and approaches its original level. The resolution of the RF power meter is 0.005 dB, which explains the rough quantization of the recorded THz signal. For the IR channel, a strong correlation between its attenuation and the recorded BER is clearly visible. The recorded BERs for the THz link verify that air turbulence has little impact on the signal, but a common trend between the channel attenuation and the recorded BER is visible. Figure 6.6(c) shows the corresponding temperature evolution in the chamber. The plots include the de-convoluted recordings in order to partially compensate for slow response time of the sensor. Obviously, the attenuation in the IR channel reduces immediately when the air flow stops. But the temperature inside the chamber decays significantly more slowly. This observation suggests that the link attenuation is mainly caused by a constant flow of air pockets with different temperatures into chamber that relatively quickly mix and achieve a thermal equilibrium once the air flow stops. The mixing however does not produce a homogeneous temperature before the airflow has reached the beams and causes refraction index variations.

A series of experiments were conducted for which air at high speed but with different temperatures is induced into the chamber. Attenuation of the IR signal and the corresponding BER as a function of time are plotted in Figure 6.7 (a) and (b). As expected, the attenuation and BER change significantly with air temperature; a strong correlation between the air temperature and BER is apparent. In comparison, the attenuation of the THz link and the corresponding BER vary less over time as shown in Figure 6.7 (c) and (d). Here, it is found that the air flow increases slightly the attenuation and the BER of the THz channel but the correlation between both quantities is not always unambiguous. This effect may be caused by reflections of the THz signals inside the transmitter and receiver

horns that lead to standing waves and multi path propagation phenomena.

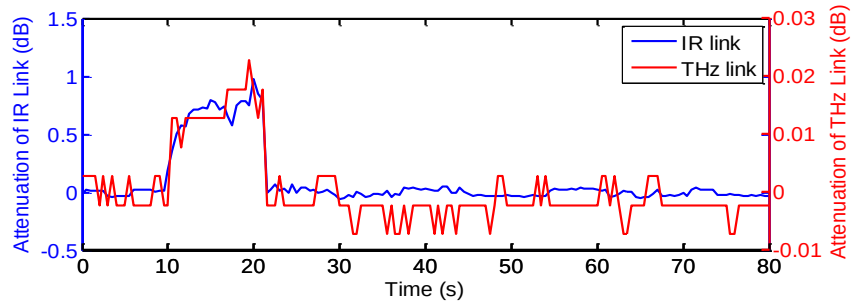

(a)

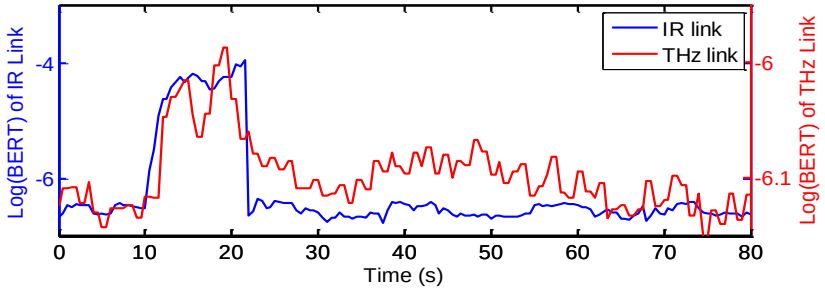

(b)

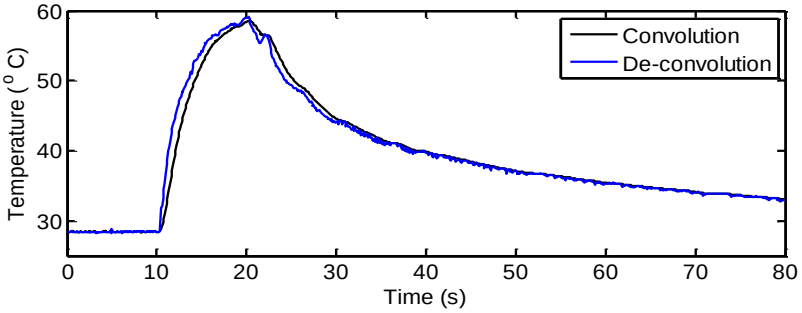

(c)

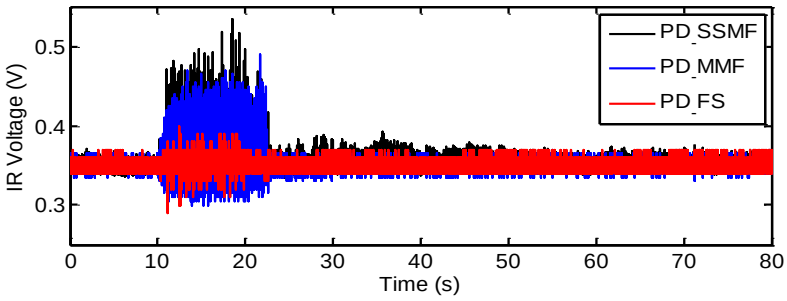

(d)

Figure 6.6 (a) Attenuation of THz link (red curve) and IR link (blue, PD_MMF) as the function of time, for warm air at high speed (b) corresponding Log(BER) of THz link (red) and IR link (blue) as the function of time, (c) Temperature evolution in turbulence chamber, (d) Normalized output power of the PD_SMF, PD_MMF and PD_FS when warm air with high speed enters chamber.

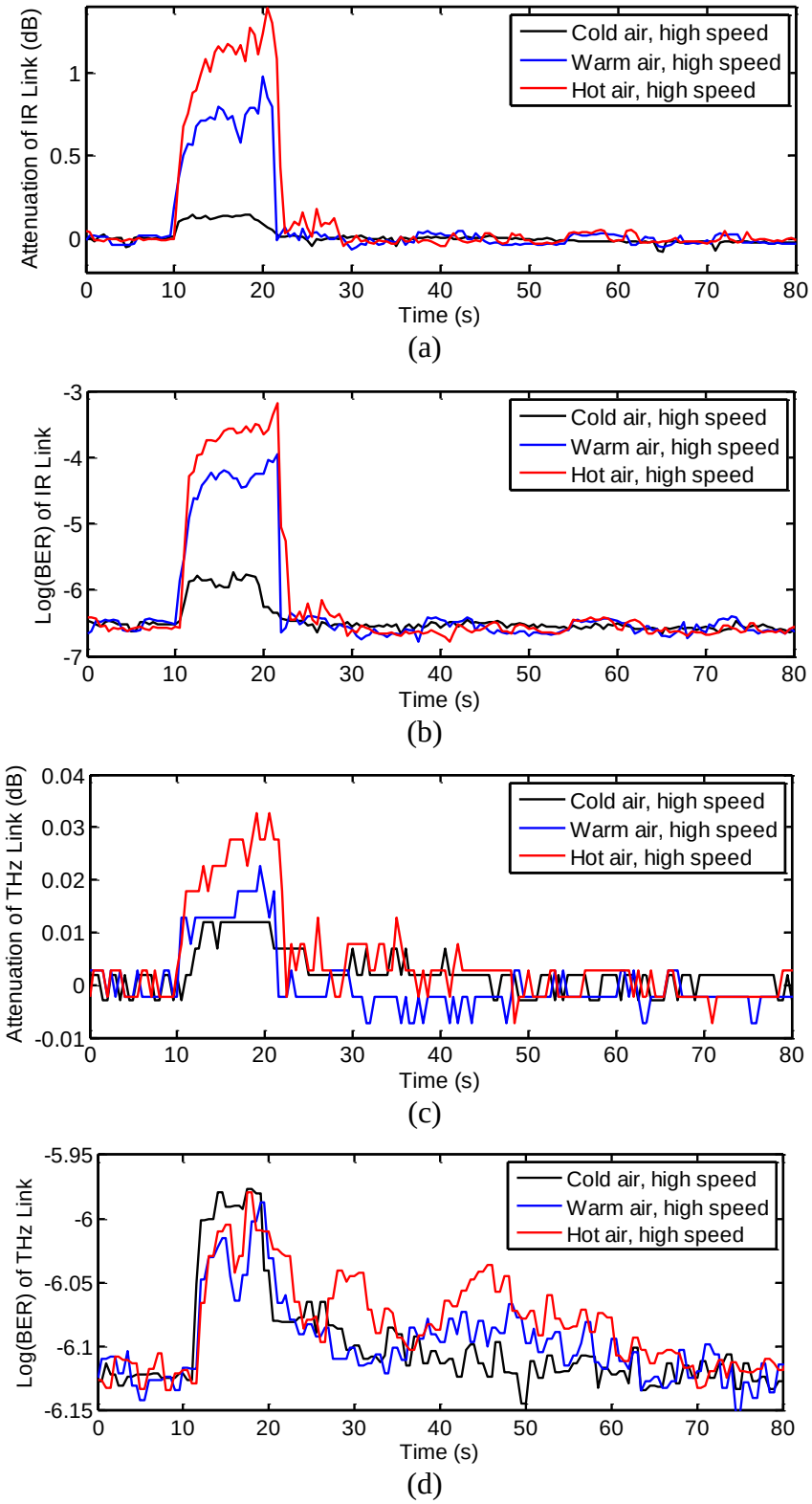

Figure 6.7 (a) Attenuation of IR link for different turbulence conditions detected with IR data Rx, (b) corresponding Log (BER) of IR link, (c) Attenuation and (d) Log (BER) of THz link for different turbulence conditions.

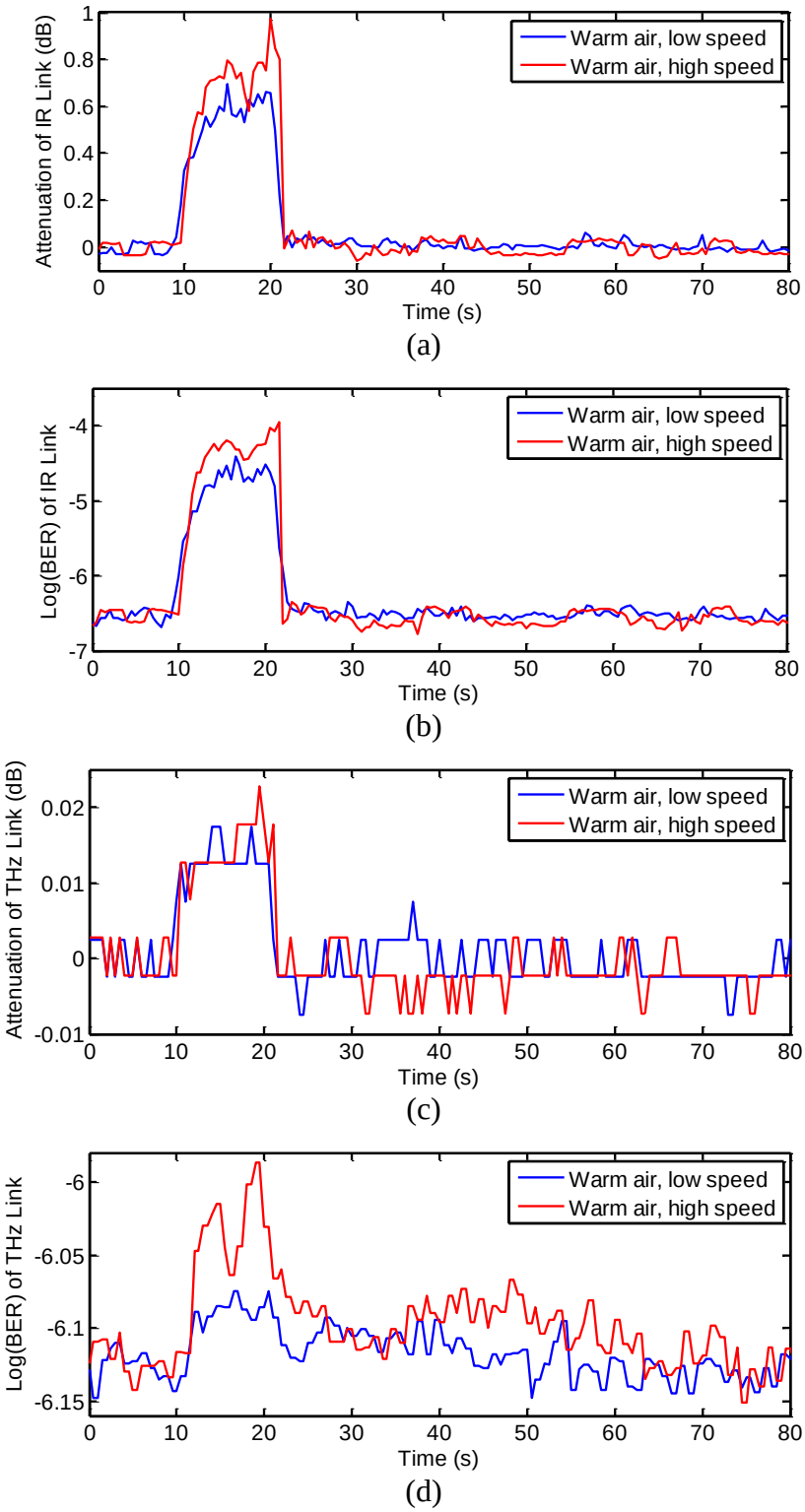

Figure 6.8 (a) Attenuation and (b) Log (BER) of IR link for different turbulence conditions, (c) Attenuation and (d) Log (BER) of THz link for different turbulence conditions.

In another series of experiments, warm air at different velocities is launched into the chamber. The attenuation of the IR signal and its corresponding BER with a fixed air temperature are shown in Figure 6.8 (a) and (b). As expected, the attenuation and BER increase with increasing air speed. The recordings of the THz link attenuation and the corresponding BER are plotted in Figure 6.8 (c) and (d).

The IR attenuation effects discussed above can solely be attributed to scintillations in the turbulence chamber since absorption phenomena are too small to cause such power variations. Scintillation is a severe problem for free-space communications at IR and visible wavelengths and has been extensively researched [124, 182, 183]. The constantly changing turbulence pattern causes the scintillations, which leads to speckle effects in the receiver plane as shown in Figure 6.9. The smaller the receiver aperture the more likely that spatial averaging is less effective resulting in the detection of relatively large power level fluctuations. If scintillation effects were to occur, more pronounced variations in the power coupled into PD_SSMF with small aperture would be expected compared to the output of the free space large area detector PD_FS. In Figure 6.2(d), apparently, the variations in the power coupled into PD_SSMF are stronger compared to those of the IR power detected by the PD_FS. All recordings were done at a sampling rate 125 kHz and clearly visible is the sharp drop off of the fluctuations compared to the air temperature decay (Figure 6.6(c)) supporting the aforementioned picture of an air stream consisting of air pockets with different temperatures.

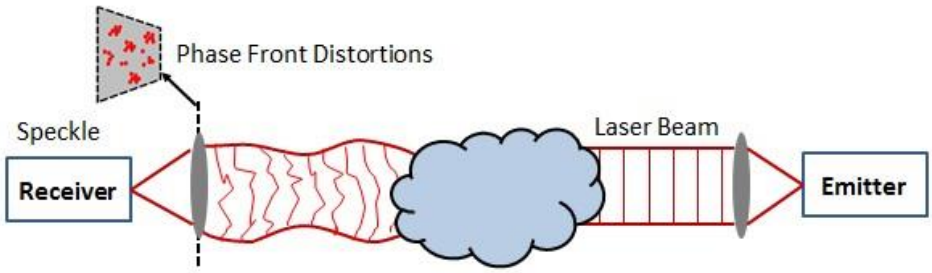

Figure 6.9 Air turbulence causes refractive index fluctuations resulting into speckle (intensity variations at receiver) that limits the reach of IR systems.
Source: [181]

6.1.3 Scintillation Effect Study

Scintillations are caused by local refraction index changes of air. Since the refraction index itself depends on the air pressure and temperature, both quantities can contribute to this phenomenon. To analyze which factor is dominant in the setup, the output of D1 shown in Figure 2.4 is recorded by an electrical spectrum analyzer. Note, acoustical noise in the lab, airflow in the room, and vibrations of the lab table significantly affect the interferometer. However, one can visualize the impact of temperature fluctuations inside the chamber by comparing the spectra for hot and cold airflow at same speed (Figure 6.5). In both experiments vibrations and acoustical noise of the setup are similar but the spectra significantly differ. Hot airflow causes a relatively wider spectrum that contains more power. Two holes in the turbulence chamber allow the THz, IR, and visible beams to pass through the chamber. When the two holes to the chamber through which the beams are launched are covered with a foil (Polyvinylidene chloride, 20 μm). Then the airflow out of the chamber and into the lab environment via these two paths is reduced. By covering or uncovering these holes, the vibrations and acoustical noise in the system change. Under conditions of covered and uncovered hole, the integrated power density of the recorded spectra is shown in Figure 6.4, where the power is reduced when the holes are

covered. Regardless of the change in vibrations and acoustical noise in the system, the temperature of the launched air obviously has a stronger impact on the spectra than the airspeed, which correlates with pressure variations inside the airflow. This leads to the conclusion that the scintillation effects in the setup are mainly caused by temperature fluctuations which fits to a fundamental assumption made for outdoor scintillation models [17, 18].

The effects of temperature variations in the chamber can be separated into two parts - a spatially more uniform and slowly changing temperature increase (~seconds) and relatively fast temporally and spatially varying temperature gradients (~kHz). In Figure 6.10 (b) and (c), the phase change in one arm of the interferometer and temperature evolution at a fixed position (b) in the chamber are shown. The phase change is calculated using the output from D1 and D2 by employing a phase unwrapping algorithm. It can be seen that the slow phase change follows closely the temperature evolution. To further confirm the conclusion, estimation of the phase change is conducted using the refraction index of air with the approximation $n = 1 + 79 \times 10^{-6} P/T$ [19], where P, T stand for the atmospheric pressure in millibar and a uniform environmental temperature in Kelvin, respectively. In Figure 6.10 (b), a 18K temperature increase would lead to a phase change of about -40π assuming an effective chamber length of ~1m. This agrees reasonable well with the measured maximum phase shift as shown in Figure 6.10 (c). Small differences between calculated and measured phase shifts can be probably attributed to measurement errors regarding the air temperature inside the turbulence chamber.

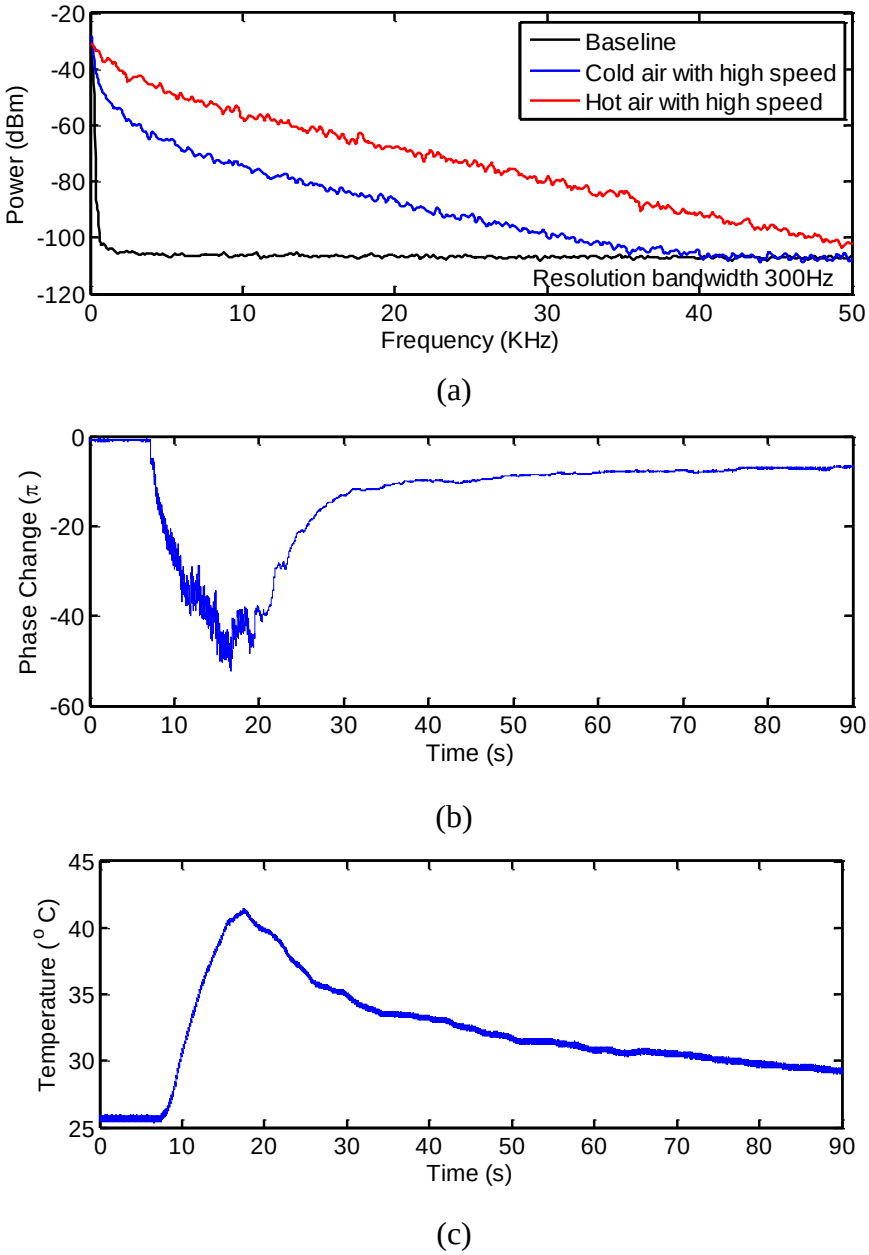

Figure 6.10 (a) Power density spectra of the interference pattern at D1 under different turbulence conditions; (b) phase change in the chamber detected with D1 and D2; (c) temperature evolution of the chamber detected by T2 (Figure 6.2).

6.2 Attenuation Simulation in Atmospheric Turbulence

When using the parameters shown in Table 6.1 and the length for the turbulence chamber of L=90cm in Eqs. (4.14, 4.29, 4.36), the experimentally and theoretically determined

attenuations become comparable as plotted in Figure 6.11. In case of a perfect matching between experiment and theory, the measurement results should reside on the diagonal of the plot shown as dashed line. While for both the IR and the THz signal, a linear correlation between experimental and theoretical values of channel attenuation can be seen. Some divergence from the ideal diagonal line is visible. Likely, the uncertainty in the effective turbulence length is the dominant factor that causes this discrepancy. When assuming an effective turbulence length of about 60cm, theory and experiment match well. Here, the effective turbulence length is different from the chamber length, which is shorter than the chamber length of 90 cm in our experiment. So, if the chamber length is changed from 60cm to longer, the effective turbulence length should be used in our calculation for the attenuation due to atmospheric turbulence. However, if the effective turbulence length is longer than the chamber length, the chamber length should be considered in the calculation.

Table 6.1 Refractive Index Structure Parameter Under Different Turbulence Conditions

Turbulence condition	C_n^2 **(m$^{-2/3}$)**
Cold air, high speed	3.5×10^{-11}
Warm air, low speed	5×10^{-10}
Warm air, high speed	10^{-9}
Hot air, low speed	1.2×10^{-9}
Hot air, high speed	2.3×10^{-9}

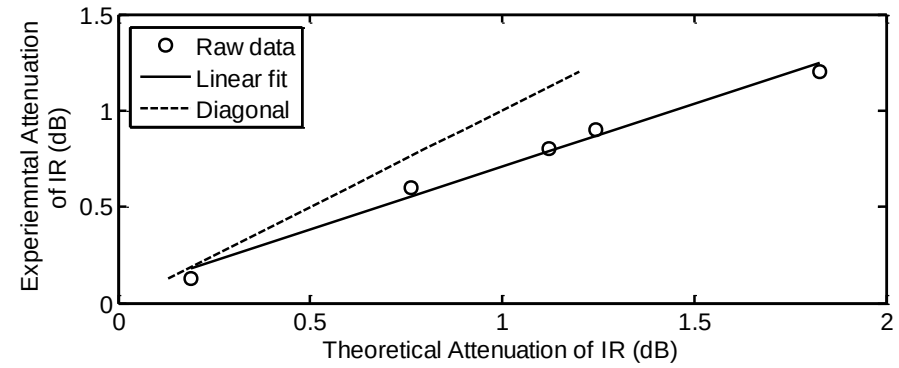

(a)

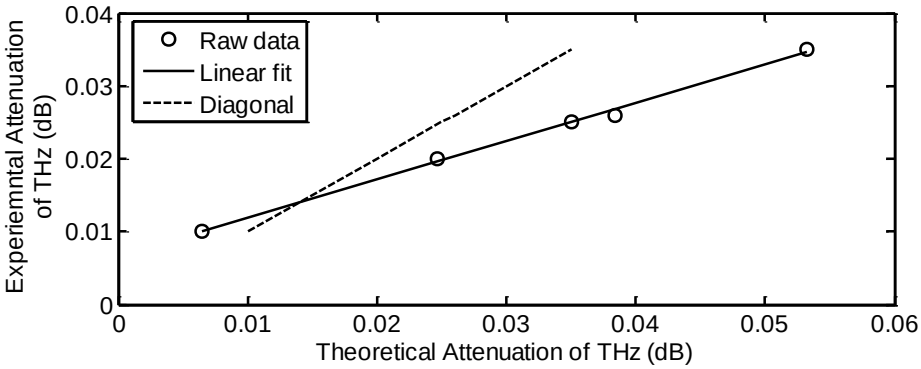

(b)

Figure 6.11 Comparison of experimental and theoretical results of IR (a) and THz (b) attenuations under different turbulence conditions.

The turbulence chamber can realize different turbulence strengths by changing the airspeed and temperature output from the air supplier. However, the turbulence strength can also be changed by changing the position of the turbulence source.

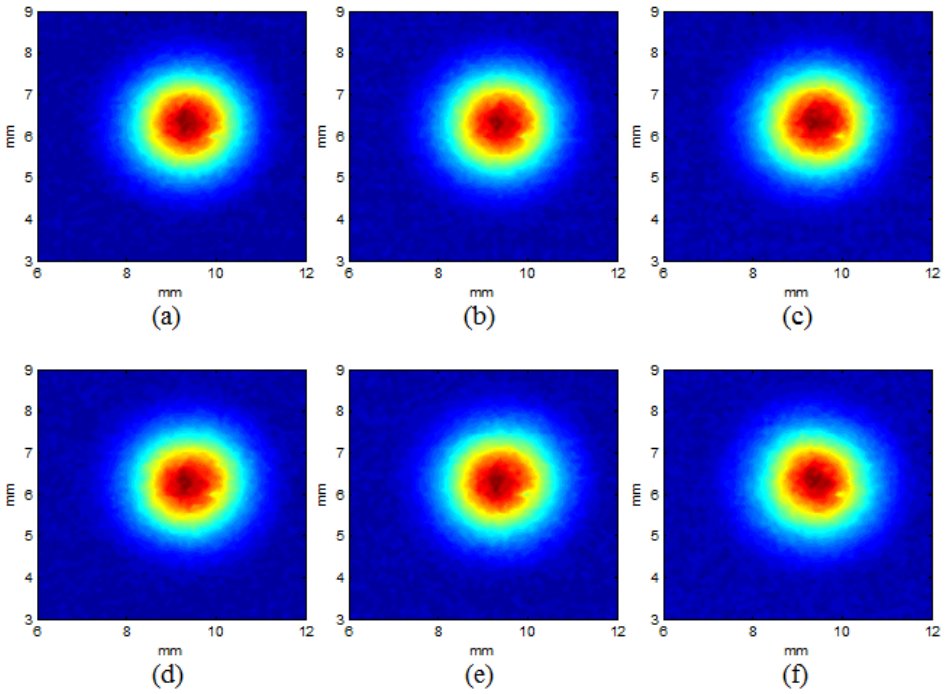

Figure 6.12 (a) no air, (b) cold air with high speed, (c) warm air with low speed, (d) warm air with high speed, (e) hot air with low speed, (f) hot air with high speed.

The beam spreading is recorded by using a commercially available 124×124 pixels Laser Beam Analyzer with 100 μm pixel pitch as shown in Figure 6.12. But the spreading of the beam spot is not visible due to the weak turbulence strength. The Fresnel ratio Λ of beam at the receiver cannot directly be measured in the setup. From Eqs. (4.38, 4.39), one can derive a 1st order functional relationship between the mean intensity and the RISP of the form

$$\left\langle I\left(0,L\right)\right\rangle = \frac{W_0^2}{W_e^2} = \frac{W_0^2}{W^2}\left(1-1.33\sigma_R^2\Lambda^{5/6}\right) \tag{6.1}$$

This relationship suggests that when plotting the measured mean intensity versus the RISP, its values should reside on a straight line with negative slope. Figure 6.13 seems

to indicate this which would support our assumption that the temperature gradient in Eq. (4.2) is a suitable quantity to characterize the turbulence.

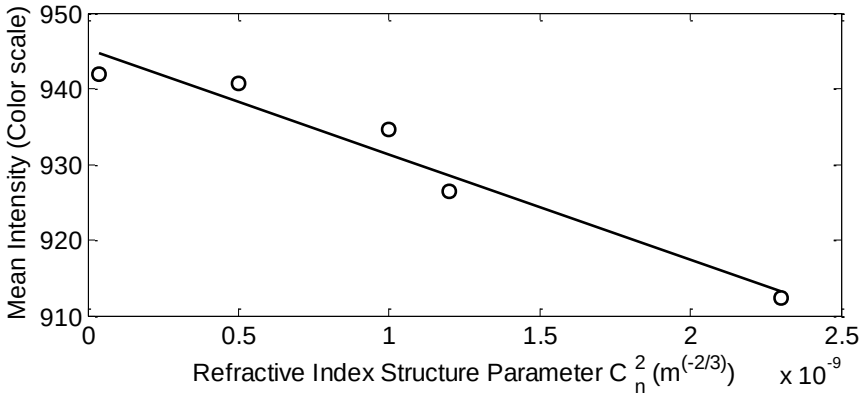

Figure 6.13 Intensity of laser beam at receiver side versus index of refraction structure parameter, a linear fit to the data is shown.

6.3 Summary

When the THz beam is superimposed with IR beam and propagates through the emulated atmospheric turbulence chamber, the signal power attenuation and BER degradations are measured, analyzed and compared. Different air turbulence conditions are emulated in the chamber and signal impairments recorded. Simulated link performance degradations are in agreement with the experimental results. Under identical turbulence conditions the IR signal is significantly more attenuated than the THz signal which shows almost no degradation. As the air temperature and speed become higher, the attenuation becomes more severe in the IR range. However, the impact on THz signal remains minimal. It is found that even for airflows comparable to the speed of hurricanes and temperature enhancements of several tens of degrees Kelvin the attenuation of the THz signal stays

below a tenth of a dB for transmission length in the range of a meter. Experimental observations demonstrate that the observed scintillation effects for the IR and THz signals are mainly caused by temperature fluctuations in the turbulence.

CHAPTER 7

EXPERIMENTAL AND SIMULATING RESULTS IN RAIN

Similar to air turbulence, there are experimental problems in characterizing wireless links in outdoor rain weather conditions, such as long observation time, uncontrollable rain rate and varying rain-drop size distributions. These variables present challenges in measuring and analyzing the attenuation by rain on communication channels. In the experiment a rain chamber which can realize controlled and reproducible lab conditions is designed.

The block diagram of the setup is shown in Figure 7.1. The rain chamber has a dimension of $100 \times 20 \times 20 cm^3$ (L ×W ×H) as shown in Figure 7.1(a). Air and water valves on its top are used to fill and pressurize the chamber. Its bottom plate is machined with 3264 holes and 31 gauge needles are epoxied into each hole as shown in Figure 7.1(b). The chamber is initially filled with distilled water. Pressurizing the chamber with air forces water release through the needles which generate raindrops. The average raindrop diameter, which depends on the radius of the needles, is about 1.9 mm [184]. Its rain rate can be controllably varied from 0 to 500 mm/hr by changing the air pressure in the chamber. The rain rate, used to classify the rain speed, is less than 3.8 mm/hr for light rain and more than 7.6 mm/hr for heavy rain [185]. Some variability in the rain rate at different locations below the rain chamber is observed. To characterize the average rain rate of the chamber, five beakers (opening area of 56.7 cm^2) are positioned underneath the chamber and collect rain for a minimum of 60 s. The total volume of water from the beakers is measured to determine the average rain rate.

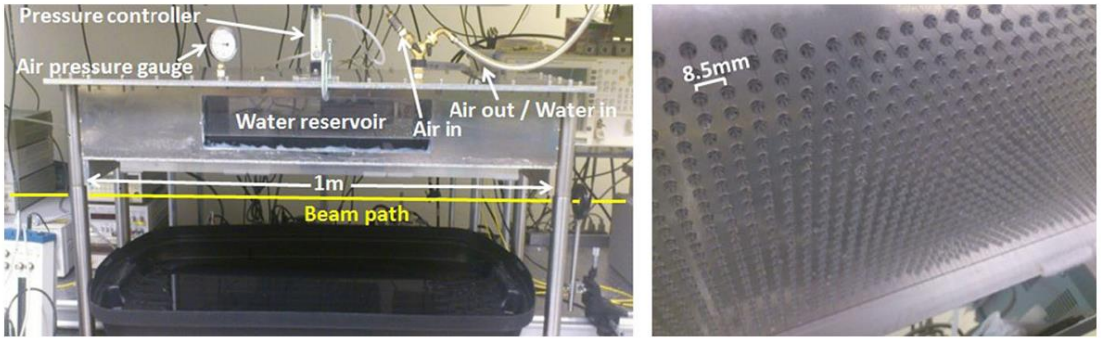

(a) (b)

Figure 7.1 (a) photo of the rain chamber, and (b) photo of needle distribution at the bottom of the rain chamber.

The 1-min averaged rain rate is expressed in units of mm/hr to ease comparisons with other scientific reports [186]. Typically ten measurements of the rain fall are averaged to calculate an average rain rate at a specific pressure. There is a linear relationship between rain rate and pressure as shown in Figure 7.2. So the rain rate can be controllable varied from around 50 mm/hr to about 500 mm/hr by changing the input pressure. Table 7.1 shows the characteristic of rain intensity with respect to rain rate in millimeters per hour based on WMO [187]. Comparing the rates with those occurring in nature, very heavy rain falls can be produced in the laboratory with an effective path length of 4m.

Table 7.1 Rain Intensity Classification by Rain Rate

Rain intensity	Rain rate (mm/hr)
Light	$R < 2.5$
Moderate	$2.5 \leq R < 10$
Heavy	$10 \leq R < 50$
Extreme	$R \geq 50$

Source: [187]

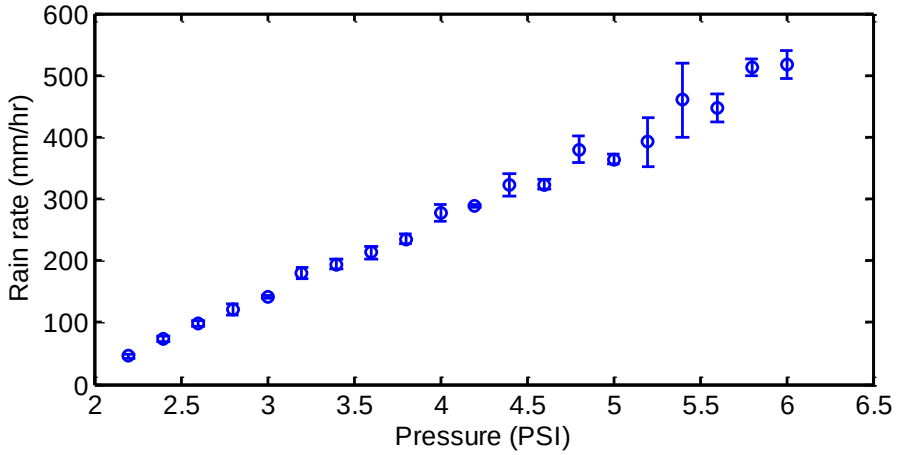

Figure 7.2 Rain rate in mm/hr from the rain chamber with respect to the air pressure in the chamber. The vertical error bars with 95% confidence interval shown in the plot represent the standard deviation of recorded rain rates.

7.1 THz Spectral Analysis of Rain Drops

For the characterization of the size distribution of the rain drops generated from the chamber, still pictures of the rain are acquired when the system is running with a constant pressure. In these pictures, individual rain drops are clearly visible and a ruler is also include in the pictures as a reference for the size measurement of the rain drops. Then using image analysis software (Image J), it is possible to count the pixels of the rain drops. Typically 100 drops are measured at each rain rate. It is observed that the size of the rain drops is independent of the pressure and rain rate of the chamber. The distribution of rain drop sizes is shown in Figure 7.3. In a good approximation, the drop size distribution is approximately follows a Gaussian function with an average diameter of $\bar{D} = 1.9\,\text{mm}$ and a variance of $\sigma^2 = 0.08\,\text{mm}^2$.

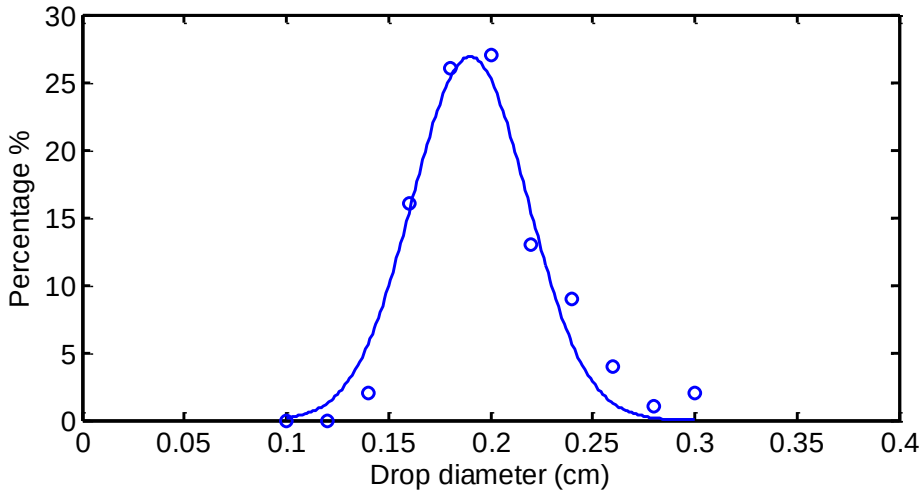

Figure 7.3 Measured rain drop size distribution. A Gaussian fit to the data is shown with 1.9 mm average diameter and 0.4mm distribution width.

The THz-TDS waveform through the rain chamber is measured at a fixed rain rate (fixed air pressure in the rain chamber). To characterize the average rain rate of the chamber, five beakers (opening area of 56.7 cm^2) are positioned underneath the chamber and collect rain for a minimum of 60 s. The total volume of water from the beakers is measured to determine the average rain rate. As a reference measurement, the THz waveform is also measured in the absence of rain. Using the standard Fourier Transform analysis of the time-domain waveforms, the attenuation spectrums of the transmitted THz waveform are measured and shown in Figure 7.4 under rain rates of 226 and 303 mm/hr. The strong peaks at 0.557THz and 0.763THz are artifacts from water vapor lines, which is consistent with Grischkowsky's study [24, 25]. Using the measured attenuation data for different rain rates, the attenuation versus rain rate at a fixed frequency of 625GHz is plotted in Figure 7.5. The relationship between rain rate and attenuation is approximately linear.

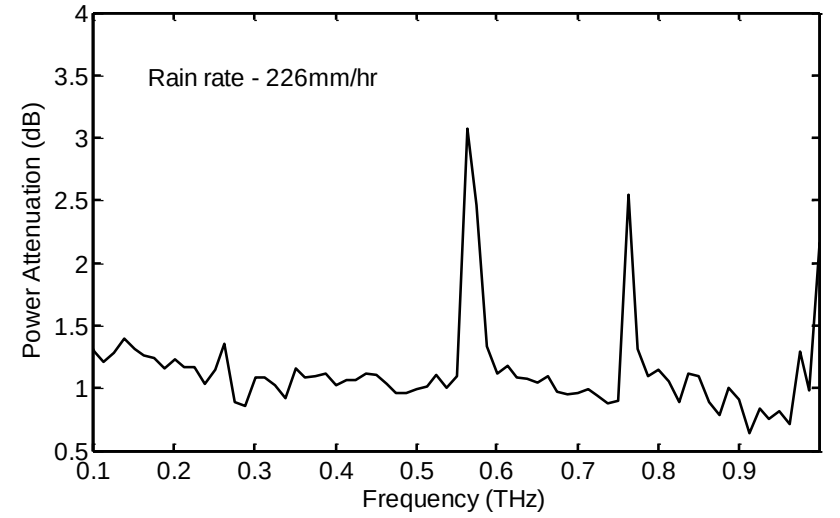

(a)

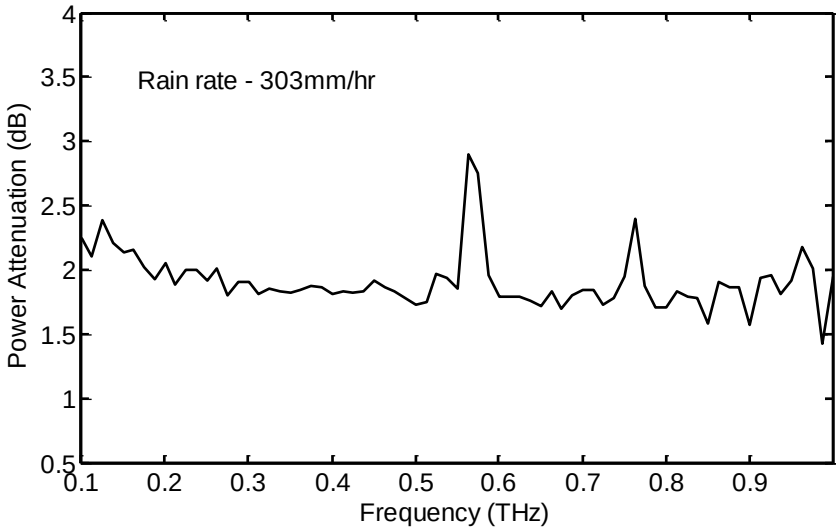

(b)

Figure 7.4 THz power attenuation spectrum under rain rates of (a) 226mm/hr, (b) 303mm/hr.

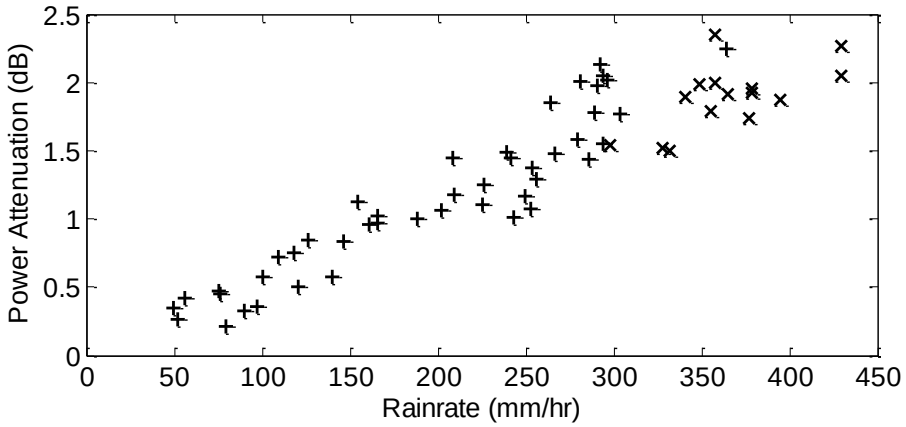

Figure 7.5 Measured attenuations of THz frequency at 625 GHz for different rain rates.

7.2 Experimental Measurements in Rain

To determine the receiver sensitivities, BER dependence of the THz and IR signals on the detected power using a 2^7-1 PRBS (Pseudorandom binary sequence) is measured. The BERT's decision threshold is optimized at a BER = 10^{-6}. Then the power of the THz signal is reduced stepwise by decreasing the iris aperture. Likewise the IR BER performance versus the received power is recorded by adjusting the EDFA output power. The decision thresholds are optimized at a BER= 1×10^{-6}. Different slopes for both sensitivity curves are visible. If both signals and receivers would be ideal, the sensitivity curves would reside on top of each other. But imperfections in the THz signal result in a significant slope change. Eye diagrams of THz and IR signals at BER = 10^{-6} are recorded as shown in Figure 7.6. Timing jitter in the THz link (jitter_RMS : 44.99ps, jitter_p-p : 146.67ps), which is likely introduced by the Frequency Multiplier Chain inside the THz source, is larger than that of the IR signal (RMS : 20.62ps, p-p : 122.22ps) and leads to a significant horizontal eye closure and the decrease slope steepness [188].

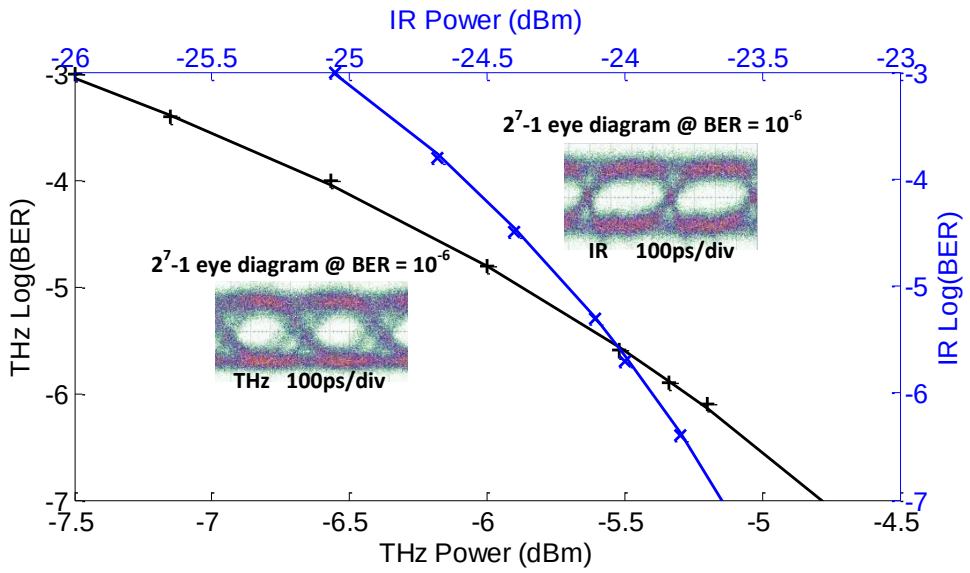

Figure 7.6 Sensitivity curves of THz and IR links. Inset: Eye diagrams of THz and IR signals at BER = 10^{-6}.

7.2.1 Attenuation and BER Performance

After pressurizing the chamber, raindrops are randomly squeezed out from the needles and block temporarily and partially the beam path. A typical evolution of the resulting average attenuations in the THz and IR links shows Figure 7.7 (a). For measuring the IR attenuation the output from the PD_MMF is used. The attenuation of the THz signal can be calculated from the recorded RF power on the receiver side. Twenty seconds after starting the recording, raindrops cross the propagation path of the beams. A time-averaged recording (500 ms integration time) of the THz and IR links is applied. At a rain rate of 213 mm/hr the THz link suffers a little bit higher attenuation (~0.1 dB) compared to the IR link, which is due to the slightly larger extinction cross section of rain drops at THz frequencies [184]. Our THz frequency is sufficiently different from resonant absorption

frequencies of water vapor to minimize resonant absorption [29, 189-192]. After 80 seconds recording time the pressure inside the rain chamber returns to atmospheric pressure and the transmitted THz and IR signal power approach their original level. For both channels, a strong correlation between their attenuation and their time-averaged BER (integration time 1s) is clearly visible. From the comparison between Figure 7.3 (a) and (b), it can be seen that the THz link suffers slightly higher power attenuation, but the IR link suffers higher increase of the BER during the rain fall. This is attributed to the different slopes of BER curves as shown in Figure 7.6, which is caused by the long timing jitter in THz link.

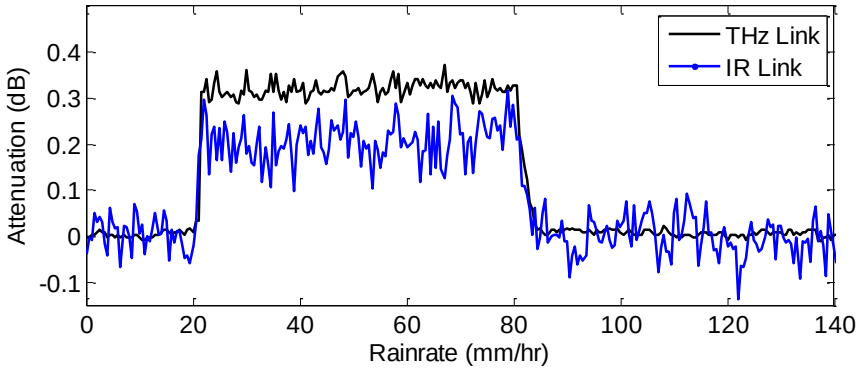

(a)

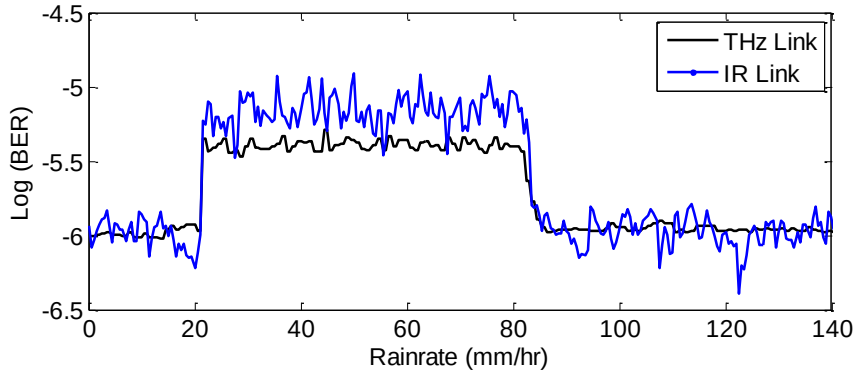

(b)

Figure 7.7 Attenuation (a) and Log(BER) (b) of the THz and IR links as a functions of time. Rain starts at a rate of 213 mm/hr at ~20 s and stops at ~80 s.

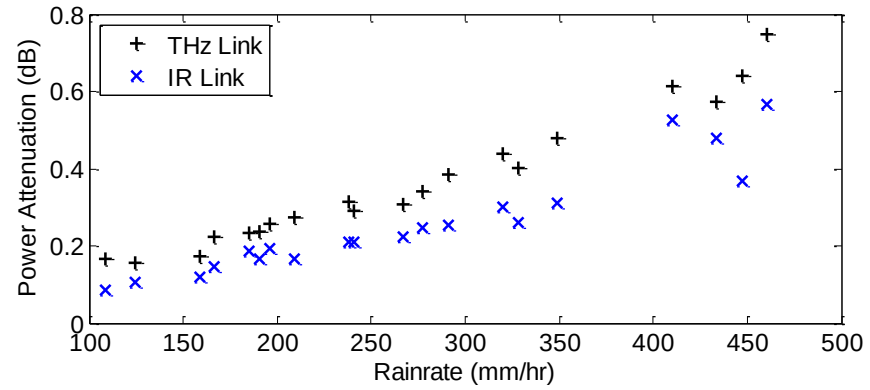

(a)

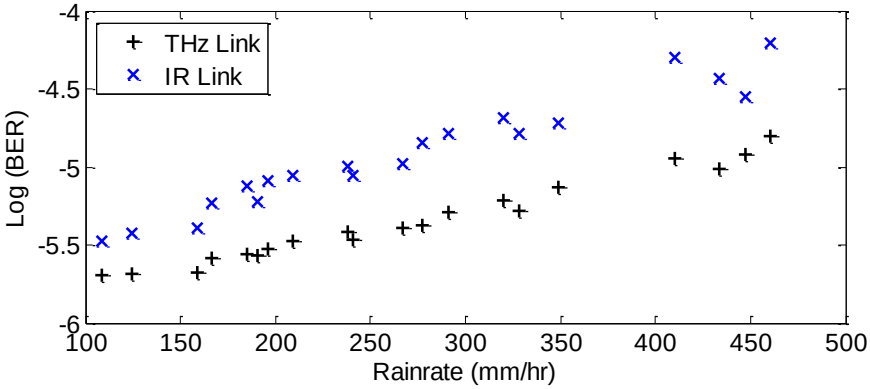

(b)

Figure 7.8 (a) Attenuations of THz and IR links with respect to rain rates and (b) their corresponding BERs.

A series of experiments were conducted for which the chamber operated at different rain rates. The attenuation of the THz and IR signals as a function of rain rates is plotted in Figure 7.8 (a). In this study, the rain rate is calculated by averaging 1-min rain rate measurements at 5 different positions and is expressed in mm/hr to ease comparisons with other technical reports [170]. Similar to Figure 7.7 (a), the THz signal suffers a slightly higher attenuation because of its slightly larger extinction cross section at THz frequencies where Mie scattering is dominant form of interaction. Figure 7.8 (b) shows that the THz link performs independent of the rain rate at better BER than IR link even though it shows higher attenuation. This is consistent with the results shown in Figure 7.3

for a single rain rate.

7.2.2 Scintillation Effect Study

Besides the power decay caused by beam blocking through rain, scintillation is another phenomenon that can lead to severe power fluctuations on the receiver side and has been extensively studied for free-space communications at IR and visible wavelengths [24, 25]. The ensemble of raindrops inside the beams causes local refraction index variations, which leads to speckle effects in the receiver plane. The smaller the receiver aperture, the more likely that spatial averaging is less effective which results in a detection of relatively large power level fluctuations. If scintillations were to occur, more pronounced variations would be observed in the output of PD_SSMF with small aperture compared to that of PD_FS with a large area detector. Apparently in Figure 7.9, the variations of the IR power coupled into PD_SSMF are stronger compared to those of PD_FS indicating the presence of scintillations. All recordings were done with a sampling rate of 10 kHz.

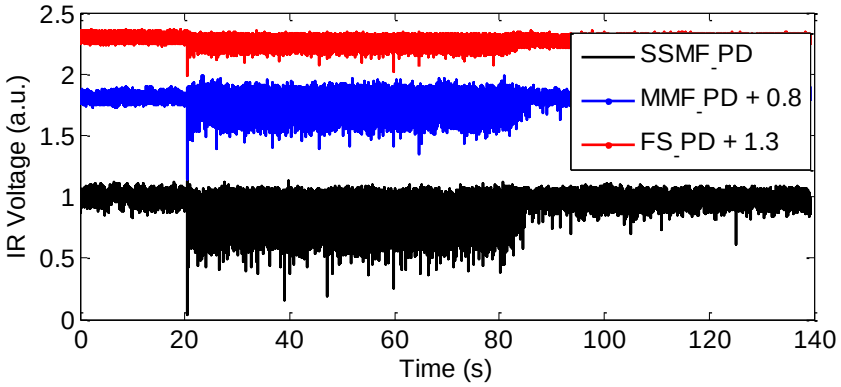

Figure 7.9 Normalized output power of the PD_SSMF, PD_MMF, and PD_FS at 158 mm/hr rain rate.

7.3 Performance Simulation

Raindrop-size distribution plays an important role in estimating the attenuation by rain. Several types of raindrop-size distributions are known and a specific attenuation model recommended by the ITU-R is usually being used for attenuation calculation [34, 80, 82, 156, 162-165, 188, 194, 195]. However, they are not fully suitable for describing the artificial rain conditions which obeys a different raindrop size distribution. In the rain chamber, the raindrop size follows approximately a Gaussian distribution with an average diameter $\bar{D} = 1.9$ mm and a variance $\sigma^2 = 0.4^2/2$ mm^2 .

7.3.1 Simulation of Attenuation

For a given rain, the raindrop concentration as function of the raindrop radius can be estimated using the measured rain rate *R* [196],

$$P(r) = \frac{R}{v_t V_d}, \tag{7.1}$$

where *R* is the rain rate, v_t is the velocity of raindrops inside the beam, and V_d stands for the volume of a raindrop with radius *r*. The attenuation coefficient α in dB/km of the THz and IR channels can be determined by integrating over all the raindrop sizes as

$$\alpha = 3.3429 \int_0^\infty p(r)\,\xi_e(r) \cdot \pi r^2 dr, \tag{7.2}$$

where, $\xi_e(\chi)$ is the extinction efficiency of raindrops which can be derived from Mie scattering theory

$$\xi_e(\chi) = \frac{2}{\chi^2}\sum_{l=1}^{\infty}(2l+1)\,\mathrm{Re}\{a_l + b_l\}, \tag{7.3}$$

where, the dimensionless parameter $\chi = \frac{2\pi r}{\lambda_0}\sqrt{\varepsilon_b^{'}}$. λ_0 is the wavelength of light. $\varepsilon_b^{'}$ is the real part of relative dielectric constant of the background medium. In the experiment, the background medium is air, hence $\varepsilon_b^{'} = 1$ is assumed. a_l and b_l are the Mie coefficients as described in [197], which are functions of χ and the refractive index n. Here a double-debye dielectric model (D3M) is employed to calculate the dielectric constant of water [191]. Its real and imaginary parts refer to the relative permittivity and its dielectric loss factor for the raindrop, respectively. Both, scattering and absorption effects are considered in the extinction efficiency, which are known to be the two main effects for attenuation by rain [198].

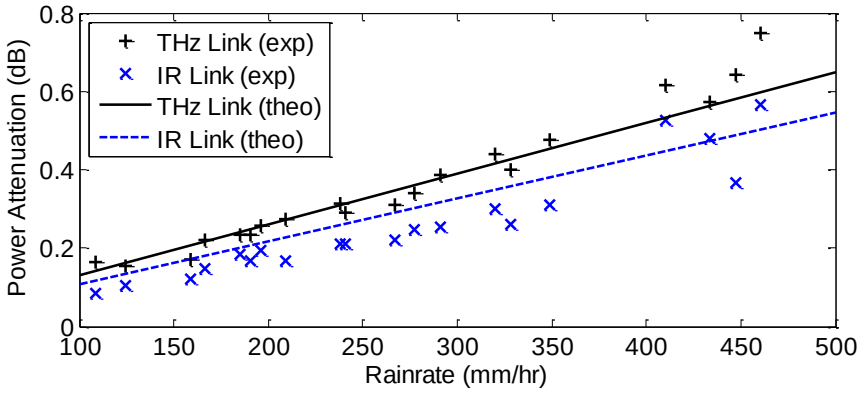

Figure 7.10 Comparison of experimental and theoretical results of THz (black) and IR (blue) attenuations at different rain rates.

The attenuation of THz and IR channels are calculated by using Eq. (7.2). Figure 7.10 shows a comparison of theoretical attenuation and the corresponding experimental results for different rain rates. The experimental attenuations are roughly consistent with

the theory. The small discrepancy between them can likely be attributed to a measurement error of rain rate and drop size. One observes that there is a relatively larger variation in the measured rain attenuation at large rain rates ~450 mm/hr compared to lower rates, which is consistent with other experimental and theoretical results in heavy rain [35].

7.3.2 Simulation of BER Performance

The extinction cross section and average attenuation can be calculated by modeling the stochastic process of rain fall and using the sensitivity BER curve and measured BER performance. For a number of raindrops (N) inside the signal beams, a Poisson distribution is considered

$$\phi_N = \frac{e^{-\overline{N}_b} \cdot \left(\overline{N}_b\right)^N}{N!}, \tag{7.4}$$

where $\overline{N}_b$ is the average raindrop number. For a raindrop count N, the specific attenuations in THz and IR links can be estimated using Eq. (7.2) and corresponding BERs can be obtained from the sensitivity curves in Figure 7.6. The expected average channel BER follows then from weighting the specific raindrop counts with their probability for occurrence using Eq. (7.4)

$$\overline{BER} = \sum_{N=1}^{\infty} BER \cdot \phi_N \ . \tag{7.5}$$

In the experiment, the average *BER* is measured as shown in Figure 7.8(b). The extinction cross section can be calculated by using an inverse procedure that starts from measured average BER values (Figure 7.11). The predicted and rain rate independent

extinction cross sections for THz and IR are $2.32\pi r^2$ and $1.88\pi r^2$ respectively [199], which agrees well with the results from Mie scattering theory. It also confirms that the different slopes of the sensitivity curves (Figure 7.6) are responsible for the somewhat counterintuitive fact that relatively higher attenuation in the THz channel not necessarily leads to lower BER performance than in the IR channel as shown in Figure 7.8 (a) and (b).

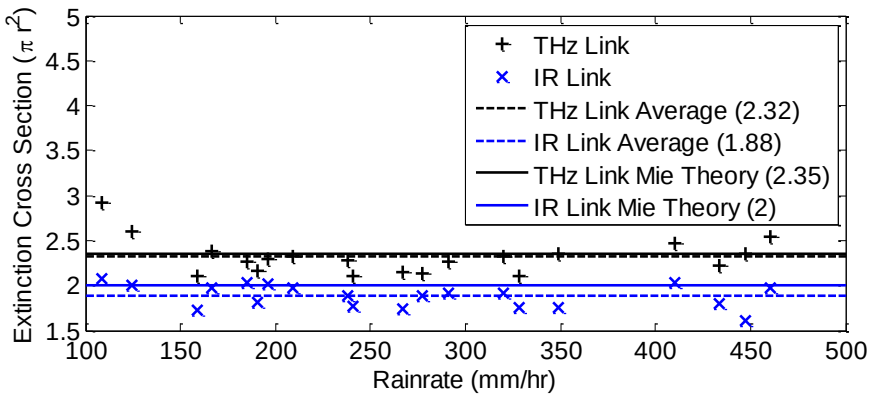

Figure 7.11 Predicted extinction cross sections using a stochastic rain model and measured receiver sensitivities. The average extinction cross sections from our prediction for THz and IR links are 2.32 and 1.88 in unit πr^2.

7.4 Summary

The THz attenuation due to rain over a frequency band ranging from 0.1 to 1 THz over a 4m distance is evaluated A rain chamber is designed which can produce controllable and reproducible rain conditions with rain rates from 50mm/hr to 500mm/hr. The THz power loss is measured by using a THz-TDS system when it propagates through the rain chamber. Theoretical rain attenuation is calculated by employing Mie scattering model and measured Gaussian distribution of rain drop sizes. Calculated results are compared with experimental measurements under the whole rain intensities which can be generated in the rain chamber, and results show that they agree very well with each other. This

confirms that the theoretical model can provide very good fit for the experimental data and will enable prediction of the performance of THz wireless communication links in outdoor weather conditions.

When THz and IR beams carrying the same data load, are superimposed and propagate through emulated rain conditions, the signal attenuation and BER degradation due to rain are measured, compared, and analyzed. Under identical rain rate (raindrop concentration), the THz signal suffers slightly higher attenuation compared to the IR signal due to the slightly larger extinction cross section of raindrops in the THz band. But in the setup, the THz signal performs at better BER than the IR channel, which indicates that the overall performance of a channel is not just dependent on its attenuation. Different rain rates are emulated with the rain chamber to vary the attenuation for the THz and IR channels. It is demonstrated that the IR signal is impaired by both the attenuation and scintillation effects. A theoretical model based on Mie scattering is used to simulate the attenuation in both links and the extinction cross section of raindrops. The results agree well with the experimental observations. In conclusion, for typical rain conditions, the attenuations for THz and IR links are comparable.

CHAPTER 8

CONCLUSIONS AND FUTURE WORK

The research work in this dissertation is summarized and concluded in this chapter. Future word is mentioned and described roughly.

8.1 Conclusions

In order to analyze the impairments of Terahertz (THz) and Infrared (IR) links caused by different weather conditions such as atmospheric turbulence and rain, THz and IR free-space communication links at 625GHz and 1550 nm, respectively, with a maximum data rate of 2.5Gb/s have been developed. A usual non return-to-zero (NRZ) format is applied to modulate the IR channel while a duobinary modulation technique is utilized to driving the multiplier chain based 625GHz source, which enables signaling at high data rate and higher output power. The performance of both channels is analyzed by measuring the power attenuation and bit-error-rates (BERs) in each link.

Temperature and pressure fluctuations in the air lead to the random deviation from the mean value of refractive index. Based on the Kolmogorov spectrum of plane waves, Rytov variance is used to classify the atmospheric turbulence strength. Andrew's method is employed to simulating the power due to turbulence in THz and IR channels. To characterize the phase change in the links caused by turbulence, a Mach-Zehnder interferometer is used to confirm the existence of turbulence induced scintillation effects in IR channel. Due to the relatively larger size of raindrops compared to THz wavelength, Mie scattering theory is applied. The attenuation by rain is modeled using a double-debye dielectric model (D3M) for the water dielectric constant. A Gaussian raindrop size

distribution is utilized based on the fitting of the raindrop distribution. The specific attenuation is predicted according to Beers-Lambert Law and integrating it over all the raindrop sizes. Simulation results of attenuation by atmospheric turbulence and rain in both channels are presented and compared. Due to the relatively small wavelength of IR compared to THz wavelength, one would expect the obvious scintillation effects in IR link. The IR beam at 1550nm carrying the same data rate is superposed with the THz beam (625GHz) and propagates through the same turbulence and rain conditions. An obvious scintillation effect is observed in the IR link, which confirms the presence of scintillation effects.

8.2 Future Work

As shown in this dissertation, THz and IR signaling performance in atmospheric turbulence and rain conditions are studied theoretically and experimentally in our lab. Besides, the performance in fog and dust conditions was also investigated by our group preciously. There are still some topics suggested for future research work.

(1) Communication links in outdoor

In this research work, the performance of THz and IR communication links is measured and analyzed in the controllable laboratory. However, the weather conditions in outdoor are more complicated which cannot be characterized by the methods used in this work. The turbulence generated in the chamber is attributed to the temperature fluctuations introduced by an air supplier. In outdoor, the pressure induced local refractive index changes is relatively small and can be neglected. While the changes due to atmospheric temperature fluctuations are significant and should be considered seriously. This is consistent with the turbulence in our chamber. But these temperature inhomogeneities are

attributed to the influences of tall buildings, plants, air condition, heating machines, and/or others that can lead to temperature changes. So this needs one to consider much more for the characterization of turbulence in outdoor.

Besides, turbulence with only weak strength can be generated and Log-normal distribution model is employed for the simulation in this work. In outdoor, strong and saturated turbulences can be realized for long link length, so the Gamma-Gamma distribution, K-distribution and Negative exponential distribution models can be employed to calculate the link performance.

The rain condition generated in the lab simply follows a Gaussian raindrop size distribution based on the measurements. However, the raindrop size distributions in different sites are different and the mostly used distributions are just empirical expressions So it is a hard work to characterize communication performance when no exact raindrop distribution can be used. But, comparison between experimental and calculated results based on different distributions methods may play a role to get to a suitable model for characterization. For example, Seishiro Ishii from Japan has taken such works by employing Marshall-Palmer (M-P), Best, Polyakova-Shifrin (P-S), Weibull distribution and ITU-R specific attenuation model. Results show that the ITU-R model can provide the best fit for the experimental data.

(2) Steerable THz antennas

Line-of-sight wireless systems with high gain antennas is needed for THz communications due to the high free space path loss caused by water vapor and other molecules, particles in atmosphere. However, such design makes the whole system so directional that links will be broken when objects move into link paths. This can reduce

Qos (quality of service) if the systems. Therefore, steerable antennas are good choices to sole such problems, which can switch the systems to other alternative links intelligently.

In future work, steerable “intelligent” antennas can be employed to improve the performance of communication links.

REFERENCES

[1] Online: http://amazing-space.stsci.edu/resources/explorations/light/star-light-science.html (accessed on November 11th, 2015).

[2] G. K. Kitaeva. "Terahertz generation by means of optical lasers." *Laser Physics Letters* 5, no. 8 (2008): 559-576.

[3] K. L. Vodopyanov. "Terahertz-wave generation with periodically inverted gallium arsenide." *Laser physics* 19, no. 2 (2009): 305-321.

[4] V. Bratman, M. Glyavin, T. Idehara, *et al*. "Review of subterahertz and terahertz gyrodevices at IAP RAS and FIR FU." *IEEE Transactions on Plasma Science* 37, no. 1 (2009): 36-43.

[5] K. Ajito, Y. Ueno. "THz chemical imaging for biological applications." *IEEE Transactions on Terahertz Science and Technology* 1, no. 1 (2011): 293-300.

[6] P. H. Siegel. "Terahertz technology in biology and medicine." *2004 IEEE MTT-S International Microwave Symposium Digest* 3: 1575-1578.

[7] J. F. Federici, R. L. Wample, D. Rodriguez, *et al*. "Application of terahertz Gouy phase shift from curved surfaces for estimation of crop yield." *Applied Optics* 48, no. 7 (2009): 1382-1388.

[8] Y. L. Hor, J. F. Federici, R. L. Wample. "Nondestructive evaluation of cork enclosures using terahertz/millimeter wave spectroscopy and imaging." *Applied Optics* 47, no. 1 (2008): 72-78.

[9] R. Appleby, H. B. Wallace. "Standoff detection of weapons and contraband in the 100 GHz to 1 THz region." *IEEE Transactions on Antennas and Propagation* 55, no. 11 (2007): 2944-2956.

[10] J. Yinon.Counterterrorist detection techniques of explosives. Atlanta, GA: Elsevier, (2011).

[11] A. Sinyukov, I. Zorych, Z. Michalopoulou, *et al*. "Detection of explosives by Terahertz synthetic aperture imaging - focusing and spectral classification." *Comptes Rendus Physique* 9, no. 2 (2008): 248-261.

[12] Y. Christie. "Edholm's law of bandwidth." *IEEE Spectrum* (2004).

[13] IEEE 802.15 WPAN™ Task Group 3d 100 Gbit/s Wireless (TG 3d (100G)) Online: http://www.ieee802.org/15/pub/SG100G.html (accessed on November 11th, 2015).

[14] R. Miles, X. Zhang, H. Eisele, *et al*. Terahertz frequency detection and identification of materials and objects. New Youk, New York: Springer Science & Business Media (2007).

[15] R. Piesiewicz, T Kleine-Ostmann, N Krumbholz, *et al*. "Short-range ultra-broadband terahertz communications: Concepts and perspectives." *IEEE Antennas and Propagation Magazine* 49, no. 6 (2007): 24-39.

[16] J. F. Federici, L. Moeller. "Review of terahertz and subterahertz wireless communications." *Journal of Applied Physics* 107, no. 11 (2010): 111101.

[17] K. Huang, Z. Wang. "Terahertz terabit wireless communication." *IEEE Microwave Magazine* 12, no. 4 (2011): 108-116.

[18] T. Kleine-Ostmann, T. Nagatsuma. "A review on terahertz communications research." *Journal of Infrared, Millimeter, and Terahertz Waves* 32, no. 2 (2011): 143-171.

[19] H. Song, T. Nagatsuma. "Present and future of terahertz communications." *IEEE Transactions on Terahertz Science and Technology* 1, no. 1 (2011): 256-263.

[20] T. Kürner, S. Priebe. "Towards THz communications-status in research, standardization and regulation." *Journal of Infrared, Millimeter, and Terahertz Waves* 35, no. 1 (2014): 53-62.

[21] Z. Pi, F. Khan. "An introduction to millimeter-wave mobile broadband systems." *IEEE Communications Magazine* 49, no. 6 (2011): 101-107.

[22] Y. Kado, T. Nagatsuma. "Exploring sub-THz waves for communications, imaging, and gas sensing," *PIERS Proceedings* (2009).

[23] Online: http://www.thevoltreport.com/faster-internet-is-on-for-the-2020-olympics-and-beyond/ (accessed on November 11th, 2015).

[24] M. J. Fitch, R. Osiander. "Terahertz waves for communications and sensing." *Johns Hopkins APL technical digest* 25, no. 4 (2004): 348-355.

[25] V. Jungnickel, T. Haustein, A. Forck, *et al*. "155 Mbit/s wireless transmission with imaging infrared receiver." *Electronics Letters* 37, no. 5 (2001): 314-315.

[26] IEEE 802.15 WPAN Task Group 3d 100 Gbit/s Wireless (TG 3d (100G)). Online: http://www.ieee802.org/15/pub/SG100G.html (accessed on November 11th, 2015).

[27] Y. Yang, A.Shutler, D. Grischkowsky. "Measurement of the transmission of the atmosphere from 0.2 to 2 THz." *Optics Express* 19, no. 9 (2011): 8830-8838.

[28] T. Nagatsuma, Y.Yoshimizu, Y. Yasuda, *et al*. "30-Gbit/s wireless transmission over 10 meters at 300 GHz." *IEEE 39th International Conference on Infrared, Millimeter, and Terahertz waves (IRMMW-THz)* (2014).

[29] Y. Yang, M. Mandehgar, D. Grischkowsky. "Determination of the water vapor continuum absorption by THz-TDS and Molecular Response Theory." *Optics Express* 22, no. 4 (2014): 4388-4403.

[30] Y. Yang, M. Mandehgar, and D. R. Grischkowsky. "Measurements of broadband THz pulse propagation through dense fog." *CLEO: Science and Innovations* (2014).

[31] Y. Yang, M. Mandehgar, D. R.Grischkowsky. "Broadband THz signals propagate through dense fog." *IEEE Photonics Technology Letters* 27, no. 4 (2015): 383-386.

[32] E. Moon, Tae-In Jeon, D. R. Grischkowsky. "Long-path THz-TDS atmospheric measurements between buildings." *IEEE Transactions on Terahertz Science and Technology* 5, no. 5 (2015): 742-750.

[33] R. Yamaguchi, A. Hirata, T. Kosugi, *et al*. "10-Gbit/s MMIC wireless link exceeding 800 meters." *IEEE Radio and Wireless Symposium* (2008).

[34] I. Seishiro, S. Syuji, K. Toshihisa. "Measurement of rain attenuation in terahertz wave range." *Wireless Engineering and Technology* (2011).

[35] A. Hirata, R.Yamaguchi, H. Takahashi, *et al*. "Effect of rain attenuation for a 10-Gb/s 120-GHz-band millimeter-wave wireless link." *IEEE Transactions on Microwave Theory and Techniques* 57, no. 12 (2009): 3099-3105.

[36] K. Ishigaki, M. Shiraishi, S. Suzuki, et al. "Direct intensity modulation and wireless data transmission characteristics of terahertz-oscillating resonant tunnelling diodes." *Electronics letters* 48, no. 10 (2012): 582-583.

[37] M. Asada, N. Orihashi, S.Suzuki. "Voltage-controlled harmonic oscillation at about 1 THz in resonant tunneling diodes integrated with slot antennas." *Japanese Journal of Applied Physics* 46, no. 5R (2007): 2904.

[38] T. Nagatsuma. "Breakthroughs in photonics 2013: THz communications based on photonics." *IEEE Photonics Journal* 6, no. 2 (2014): 1-5.

[39] T. Nagatsuma, S. Horiguchi, Y. Minamikata, *et al*. "Terahertz wireless communications based on photonics technologies." *Optics Express* 21, no. 20 (2013): 23736-23747.

[40] S. Horiguchi, K. Arakawa, Y. Minamikata, et al. "Error-free 30–50 Gbps wireless transmission at 300 GHz." *IEEE Asia-Pacific Microwave Conference Proceedings (APMC)* (2013).

[41] H. Song, K. Ajito, Y. Muramoto, *et al*. "24 Gbit/s data transmission in 300 GHz band for future terahertz communications." *Electronics Letters* 48, no. 15 (2012): 953-954.

[42] T. Nagatsuma, H. Song, Y. Fujimoto, *et al*. "Giga-bit wireless link using 300-400 GHz bands," *IEEE International Topical Meeting on Microwave Photonics* (2009).

[43] H. Song, K. Ajito, A. Wakatsuki, Y. Muramoto, N. Kukutsu, T. Nagatsuma, and Y. Kado, "Terahertz-wave wireless communications link at 300 GHz," *2010 IEEE Topical Meeting on Microwave Photonics (MWP)* (2011).

[44] T. Nagatsuma, H. Ito, T. Ishibashi. "Hig-power RF photodiodes and their applications." *Laser & Photonics Reviews* 3, no. 1-2 (2009): 123-137.

[45] P. D. Grant, S. R. Laframboise, R. Dudek, *et al*. "Terahertz free space communications demonstration with quantum cascade laser and quantum well photodetector." *Electronics Letters* 45, no. 18 (2009): 952-954.

[46] F. Palma, F. Teppe, A. E. Fatimy, *et al*. "THz communication system based on a THz Quantum Cascade Laser and a Hot Electron Bolometer." *35th International Conference on Infrared Millimeter and Terahertz Waves (IRMMW-THz)* (2010).

[47] Z. Chen, Z. Y. Tan, Y. J. Han, *et al*. "Wireless communication demonstration at 4.1 THz using quantum cascade laser and quantum well photodetector." *Electronics Letters* 47, no. 17 (2011): 1002-1004.

[48] C. Jastrow, S. Priebe, B. Spitschan, *et al*. "Wireless digital data transmission at 300 GHz." *Electronics Letters* 46, no. 9 (2010): 661-663.

[49] S. Takeshi, T. Mukai, M. Kawamura, *et al*. "Giga-bit wireless communication at 300 GHz using resonant tunneling diode detector." *Asia-Pacific Microwave Conference (APMC)* (2011).

[50] T. Nagatsuma, K. Kato. "Photonically-assisted 300-GHz wireless link for real-time 100-Gbit/s transmission." *IEEE MTT-S International Microwave Symposium (IMS)* (2014).

[51] X. Yu, M. Galili, T. Morioka, *et al*. "Towards ultrahigh speed impulse radio THz wireless communications." *IEEE 17th International Conference on Transparent Optical Networks* (2015).

[52] T. Kleine-Ostmann, K. Pierz, G. Hein, *et al*. "Audio signal transmission over THz communication channel using semiconductor modulator." *Electronics Letters* 40, no. 2 (2004): 124-126.

[53] L. Moeller, J. F. Federici, A. Sinyukov, *et al*. "Data encoding on terahertz signals for communication and sensing." *Optics letters* 33, no. 4 (2008): 393-395.

[54] L. Moeller, J. F. Federici, K. Su. “THz wireless communications: 2.5 Gb/s error-free transmission at 625 GHz using a narrow-bandwidth 1 mW THz source.” *IEEE General Assembly and Scientific Symposium* (2011).

[55] C. Jastrow, K. Münter, R. Piesiewicz, *et al*. “300 GHz transmission system.” *Electronics Letters* 44, no. 3 (2008): 213-214.

[56] https://www.iso.org/obp/ui/#iso:std:iso:20473:ed-1:v1:en (accessed on November 11th, 2015).

[57] Y. Nakata, J. Kashio, T. Kojima, et al. “In-house wireless communication system using infrared radiation.” *Proceedings to the Seventh International Conference on Computer Communications* (1984).

[58] M. Kaine-Krolak, M. Novak. “An Introduction to Infrared Technology: applications in the home, classroom, workplace, and beyond.” (1995). Online: http://trace.wisc.edu/docs/ir_intro/ir_intro.htm (accessed on November 11th, 2015).

[59] Kahn, Joseph M., and John R. Barry. “Wireless infrared communications.” *Proceedings of the IEEE* 85, no. 2 (1997): 265-298.

[60] D. P. Edwards. “A general line-by-line atmospheric transmittance and radiance model. Version 3.0 description and users guide.” *National Center for Atmospheric Research* (1992).

[61] B. Mayer, S. Shabdanov, D. Giggembach. “Atmospheric database of atmospheric absorption coefficients.” *German Aerospace Center (DLR)* (2002).

[62] B. Mayer, and A. Kylling. “Technical note: The libRadtran software package for radiative transfer calculations-description and examples of use.” *Atmospheric Chemistry and Physics* 5, no. 7 (2005): 1855-1877.

[63] C. J. Henderson, D. G. Leyva, T. D. Wilkinson. “Free space adaptive optical interconnect at 1.25 Gb/s, with beam steering using a ferroelectric liquid-crystal SLM.” *Journal of Lightwave Technology* 24, no. 5 (2006): 1989.

[64] K. Wang, A. Nirmalathas, C. Lim, *et al*. “High-speed optical wireless communication system for indoor applications.” *IEEE Photonics Technology Letters* 23, no. 8 (2011): 519-521.

[65] C. W. J. Oh, E. Tangdiongga, A. M. J. Koonen. “42.8 Gbit/s indoor optical wireless communication with 2-dimensional optical beam-steering.” *Optical Fiber Communication Conference* (2015).

[66] C. W. Oh, F. M. Huijskens, S. Zou, *et al*. “36.7 Gbps spectrum-efficient indoor optical wireless system with beam-steering.” *The European Conference on Optical Communication (ECOC)* (2014).

[67] D. P. Edwards. “GENLN2: A general line-by-line atmospheric transmittance and radiance model. Version 3.0: Description and users guide.” Unknown 1 (1992).

[68] J. E. A. Selby, F. X. Kneizys, J. H. Chetwyn, et al. “Atmospheric transmittance/radiance: Computer code LOWTRAN 4.” *Air Force Geophysics Lab Hanscom Afb Ma* 1978.

[69] D. S. Waddy, P. Lu, L. Chen, *et al*. “Fast state of polarization changes in aerial fiber under different climatic conditions.” *IEEE Photonics Technology Letters* 13, no. 9 (2001): 1035-1037.

[70] Online: https://www.itu.int/rec/R-REC-P.676 (accessed on November 11th, 2015).

[71] S. Karp, R. M. Gagliardi, S. E. Moran, *et al*. Optical channels: fibers, clouds, water and the atmosphere, Plenum Press New York, 1988.

[72] J. C. Ricklin, S. M. Hammel, F. D. Eaton, et al. “Atmospheric channel effects on free-space laser communication.”*Journal of Optical and Fiber Communications Reports* 3, no. 2 (2006): 111-158.

[73] S. T. Fiorino, R. J. Bartell, M. J. Krizo, et al. “A computational tool for evaluating THz imaging performance in brownout or whiteout conditions at land sites throughout the world.” *SPIE Defense, Security, and Sensing* (2009).

[74] S. Bloom, E. Korevaar, J. Schuster, et al. “Understanding the performance of free-space optics.” *Journal of optical Networking* 2, no. 6 (2003): 178-200.

[75] R. Ramirez-Iniguez, S. M. Idrus, Z. Sun. Optical wireless communications: IR for wireless connectivity. Cleveland, OH: CRC press, 2008.

[76] Z. Hajjarian, M. Kavehrad, J. Fadlullah. “Analysis of wireless optical communications feasibility in presence of clouds using Markov chains.” *IEEE Journal on Selected Areas in Communications* 27, no. 9 (2009): 1526-1534.

[77] C. R. Nave. HyperPhysics - rayleigh scattering (2006). Online: http://hyperphysics.phy-astr.gsu.edu/hbase/atmos/blusky.html#c2 (accessed on November 11th, 2015).

[78] A. Al-habash, K. W. Fischer, C. S. Cornish, et al. “Comparison between experimental and theoretical probability of fade for free space optical communications.” *The Convergence of Information Technologies and Communications* (2002).

[79] Online: http://infrared.pnnl.gov/research/modeling-turbulence.asp (accessed on November 11th, 2015)

[80] T. Utsunomiya, M. Sekine. “Rain attenuation at 103 GHz in millimeter wave ranges.” *International Journal of Infrared and Millimeter Waves* 26, no. 11 (2005): 1651-1660.

[81] Y. S. Babkin, N. N. Zimin, A. O. Izyumov, *et al*. “Measurement of attenuation in rain over 1 km path at a wavelength of 0. 96 mm.” *Radio Engineering and Electronic Physics* 15 (1970): 2164-2166.

[82] S. Ishii. “Rain attenuation at Terahertz.” *Wireless Engineering and Technology*1, no. 02 (2010): 92.

[83] R. A. Bohlander, R.W. McMillan, E. M. Patterson, et al. “Fluctuations in millimeter-wave signals propagated through inclement weather.” *IEEE Transactions on Geoscience and Remote Sensing* 26, no. 3 (1988): 343-354.

[84] S. A. Khan, A. N. Tawfik, C. J. Gibbins, et al. “Extra-high frequency line-of-sight propagation for future urban communications.” *IEEE Transactions on Antennas and Propagation* 51, no. 11 (2003): 3109-3121.

[85] A. Hirata, H. Takahashi, R. Yamaguchi, *et al*. “Transmission characteristics of 120-GHz-band wireless link using radio-on-fiber technologies.” *Journal of Lightwave Technology* 26, no. 15 (2008): 2338-2344.

[86] A. Hirata, T. Nagatsuma, T. Kosugi, et al. “10-Gbit/s wireless communications technology using sub-terahertz waves.” *International Society for Optics and Photonics* (2007).

[87] G. Ducournau, P. Szriftgiser, D. Bacquet, *et al*. “Optically power supplied Gbit/s wireless hotspot using 1.55 μm THz photomixer and heterodyne detection at 200 GHz.” *Electronics Letters* 46, no. 19 (2010): 1349-1351.

[88] K. Su, L. Moeller, R. B. Barat, et al. “Experimental comparison of performance degradation from terahertz and infrared wireless links in fog.” *Journal A: Optics, Image Science, and Vision* 29, no. 2 (2012): 179-184.

[89] H. Shankar. “Duobinary modulation for optical systems.” *IEEE Journal of Lightwave Technology* 23, no. 6 (2006): 11.

[90] L. Moeller, J. Federici, K. Su. “2.5 Gbit/s duobinary signalling with narrow bandwidth 0.625 terahertz source.” *Electronics Letters* 47, no.15 (2011): 856-858.

[91] X. Yang. “A new Mach - Zehnder interferometer to measure light beam dispersion and phase shift.” Chinese Physics Letters 30, no.4 (2013): 040701.

[92] D. Penninckx, M. Chbat, L. Pierre, *et al*. “The phase-shaped binary transmission (PSBT): A new technique to transmit far beyond the chromatic dispersion limit.” *IEEE Photonics Technology Letters* 9, no. 2 (1997): 259-261.

[93] A. Lender. "The duobinary technique for high-speed data transmission." *Transactions of the Communication and Electronics* 82, no. 2 (1963): 214-218.

[94] T. W. Crowe, D. W. Porterfield, J. L. Hesler, *et al*. "Submillimeter-wave and terahertz diodes, components and subsystems." *IEEE 14th International Conference on Infrared, Millimeter and Terahertz Waves* (2006).

[95] B. Sklar. Digital communications. New Jersey: Prentice Hall PTR, 2001.

[96] A. Lender. "Correlative digital communication techniques." *IEEE Transactions on Communication Technology* 12, no. 4 (1964): 128-135.

[97] J. G Proakis. Intersymbol interference in digital communication systems. John Wiley & Sons, Inc., 2001.

[98] W. O. Popoola, Z. Ghassemlooy, C. G. Lee, *et al*. "Scintillation effect on intensity modulated laser communication systems - a laboratory demonstration." *Optics & Laser Technology* 42, no. 4 (2010): 682-692.

[99] X. Zhu, J. M. Kahn. "Free-space optical communication through atmospheric turbulence channels." *IEEE Transactions on Communications* 50, no. 8 (2002): 1293-1300.

[100] J. Zeller, T. Manzur. "Free-space optical communication at 1.55 μm and turbulence measurements in the evaporation layer." *International Society for Optics and Photonics* (2012).

[101] Z. Ghassemlooy, W. Popoola, S. Rajbhandari. Optical wireless communications: system and channel modelling with Matlab®. CRC Press, 2012.

[102] A. Labeyrie, S. G. Lipson, P. Nisenson. An introduction to optical stellar interferometry. Cambridge University Press, 2006.

[103] O. Bouchet. Wireless optical telecommunications. Hoboken, NJ: John Wiley & Sons, 2013.

[104] H. Hemmati. Near-earth laser communications. Cleveland, OH: CRC Press, 2008.

[105] H. E. Nistazakis, T. A. Tsiftsis, G. S. Tombras. "Performance analysis of free-space optical communication systems over atmospheric turbulence channels." *IET communications* 3, no. 8 (2009): 1402-1409.

[106] J. W. Strohbehn. Laser beam propagation in the atmosphere. New York, NY: Springer, 1978.

[107] W. Pratt. Laser communication systems. New York, NY: John Wiley & Sons, 1969.

[108] L. C. Andrews, R. L. Phillips. Laser beam propagation through random media. Bellingham, WA: SPIE, 2005.

[109] F. Fidler, M. Knapek, J. Horwath, *et al*. "Optical communications for high-altitude platforms." *IEEE Journal of Selected Topics in Quantum Electronics* 16, no. 5 (2010): 1058-1070.

[110] X. Tang, Z. Ghassemlooy, S. Rajbhandari, *et al*. "Experimental demonstration of polarisation shift keying in the free space optical turbulence channel." *1st IEEE International Conference on Communications in China Workshops (ICCC)* (2012).

[111] B. Lopez, M. Sarazin. "The ESO atmospheric temporal coherence monitor dedicated to high angular resolution imaging." *Astronomy and Astrophysics* 276 (1993): 320.

[112] P. A. Davidson. Turbulence: an Introduction for scientists and engineers. Oxford, UK: Oxford University Press, 2004.

[113] L. C. Andrews. Field guide to atmospheric optics. Bellingham WA: SPIE press, 2004.

[114] C. Rino. The theory of scintillation with applications in remote sensing. New York, NY: John Wiley & Sons, 2011.

[115] M. A. Al-Habash, L. C. Andrews, R. L. Phillips. "Mathematical model for the irradiance probability density function of a laser beam propagating through turbulent media." *Optical Engineering* 40, no. 8 (2001): 1554-1562.

[116] L. C. Andrews, R. L. Phillips. "I-K distribution as a universal propagation model of laser beams in atmospheric turbulence," *Journal of Optical Society of America A* 2, no. 2 (1985): 160-163.

[117] R. J. Hill, R. G. Frehlich. "Probability distribution of irradiance for the onset of strong scintillation." *Journal of Optical Society of America A* 14, no. 7 (1997): 1530-1540.

[118] J. H. Churnside, R. J. Hill. "Probability density of irradiance scintillations for strong path-integrated refractive turbulence." *Journal of Optical Society of America A* vol. 4, no. 4, (1987): 727-733.

[119] E. Jakeman, P. N. Pusey. "Significance of K distributions in scattering experiments." *Physical Review Letters* 40, no. 9 (1978): 546.

[120] G. Parry, P. N. Pusey. "K distributions in atmospheric propagation of laser light." *Journal of Optical Society of America* 69, no. 5 (1979): 796-798.

[121] J. H. Churnside, R. G. Frehlich. "Experimental evaluation of lognormally modulated Rician and IK models of optical scintillation in the atmosphere," *Journal of Optical Society of America A* 6, no. 11 (1989): 1760-1766.

[122] R. J. Sasiela. Electromagnetic wave propagation in turbulence: evaluation and application of Mellin transforms. New York, NY: Springer Science & Business Media, 2012.

[123] L. Zhang, Z. Wu, Y. Zhang, H. Detian. "Improved maximum likelihood detection for mitigating fading estimation error in free space optical communication." *Optical Engineering* 52, no. 1 (2013): 015004-015004.

[124] H. Le-Minh, Z. Ghassemlooy, M. Ijaz, et al. "Experimental study of bit error rate of free space optics communications in laboratory controlled turbulence." *IEEE InGLOBECOM Workshops (GC Wkshps)* (2010).

[125] S. Karp, R. M. Gagliardi, S. E. Moran, *et al*. Optical channels: fibers, clouds, water and the atmosphere. New York, NY: Plenum Press, 1988.

[126] L. C. Andrews, R. L. Phillips, and C. Y. Hopen, laser beam scintillation with applications: SPIE Press, 2001.

[127] D. M. Forin, G. Incerti, G. T. Beleffi, et al. "Free space optical technologies." INTECH Open Access Publisher, 2010.

[128] Z. Ghassemlooy, W. O. Popoola, E. Leitgeb. "Free-space optical communication using subearrier modulation in gamma-gamma atmospheric turbulence." *IEEE 9th International Conference on Transparent Optical Networks* (2007).

[129] H. E. Nistazakis, E. A. Karagianni, A. D. Tsigopoulos, *et al*. "Average capacity of optical wireless communication systems over atmospheric turbulence channels." *Journal of Lightwave Technology* 27, no. 8 (2009): 974-979.

[130] M. Uysal, J. Li, M. Yu. "Error rate performance analysis of coded free-space optical links over Gamma-Gamma atmospheric turbulence channels." *IEEE Transactions on Wireless Communications* 5, no. 6 (2006): 1229-1233.

[131] L. C. Andrews, R. L. Phillips, C. Y. Hopen, *et al*. "Theory of optical scintillation," *Journal of the Optical Society of America A* 16, no. 6 (1999): 1417-1429.

[132] K. Kiasaleh, A. V. Bagrov, V. P. Lukin, *et al*. "Performance of coherent DPSK free-space optical communication." *IEEE transactions on communications* 54, no. 4 (2006): 604-607.

[133] M. Niu, J. Cheng and J. F. Holzman. "Error rate analysis of M-ary coherent free-space optical communication systems with K-distributed turbulence." *IEEE Transactions on Communications* 59, no. 3 (2011): 664-668.

[134] W. O. Popoola and Z. Ghassemlooy. "BPSK subcarrier intensity modulated free-space optical communications in atmospheric turbulence." *Journal of Lightwave Technology* 27, no. 8 (2009): 967-973.

[135] L. Bao, H. Zhao, G. Zheng, *et al*. "Scintillation of THz transmission by atmospheric turbulence near the ground." IEEE Fifth International Conference on Advanced Computational Intelligence (ICACI) *(2012)*.

[136] R. L. Freeman. Radio system design for telecommunication. Bellingham WA: John Wiley & Sons, 2006.

[137] Q. Bouchet, H. Sizun, C. Boisrobert, *et al*. Free-space optics: propagation and communication. Bellingham WA: John Wiley & Sons, 2010.

[138] X. Tang. "Polarisation shift keying modulated free-space optical communication systems." University of Northumbria at Newcastle, 2012.

[139] J. Vitasek, J. Latal, S. Hejduk, *et al*. "Atmospheric turbulences in free space optics channel." *IEEE 34th International Conference on Telecommunications and Signal Processing* (TSP) (2011).

[140] J. Libich, S. Zvanovec. "Influences of turbulences in near vicinity of buildings on free-space optical links." *Microwaves, Antennas & Propagation* 5, no. 9 (2011): 1039-1044.

[141] H. Weichel. Laser beam propagation in the atmosphere. SPIE press, 1990.

[142] V. I. Tatarski, R. A. Silverman, N. Chako. "Wave propagation in a turbulent medium." *Physics Today* 14, no. 12 (2009): 46-51.

[143] G. Osche. Optical detection theory. New York: Wiley, 2002.

[144] J. W. Goodman, R.L. Haupt. Statistical optics. John Wiley & Sons, 2015.

[145] N. D. Chatzidiamantis, H. G. Sandalidis, G. K. Karagiannidis, *et al*. "Inverse Gaussian modeling of turbulence-induced fading in free-space optical systems." *Journal of Lightwave Technology* 29, no. 10 (2011): 1590-1596.

[146] A. Naboulsi, H. Sizun, F. D. Fornel. "Propagation of optical and infrared waves in the atmosphere." *Proceedings of the union radio scientifique internationale* (2005).

[147] L. Dordova, O. Wilfert. "Calculation and comparison of turbulence attenuation by different methods." *Radio Engineering* 19, no. 1 (2010): 162-167.

[148] O. Wilfert, Z. Kolka. "Statistical model of free-space optical data link." *The SPIE 49th Annual Meeting on Optical Science and Technology* (2004).

[149] M. C. Teich, B. E. A. Saleh. “Fundamentals of photonics.” Canada, Wiley Interscience, 1991.

[150] A. H. Mikesell, A. A. Hoag, J. S. Hall. “The scintillation of starlight.” *Journal of the Optical Society of America A* 41, no. 10 (1951): 689-691.

[151] X. Tang, S. Rajbhandari, W. O. Popoola, *et al*. “Performance of BPSK subcarrier intensity modulation free-space optical communications using a log-normal atmospheric turbulence model.” *IEEE Symposium on Photonics and Optoelectronic (SOPO)* (2010).

[152] T. A.Tsiftsis, H. G. Sandalidis, G. K. Karagiannidis, *et al*. “Optical wireless links with spatial diversity over strong atmospheric turbulence channels.” *IEEE Transactions on Wireless Communications* 8, no. 2 (2009): 951-957.

[153] A. F. Spilhaus. “Raindrop size, shape and falling speed.” *Journal of Meteorology* 5, no. 3 (1948): 108-110.

[154] H. R. Pruppacher, K. V. Beard. “A wind tunnel investigation of the internal circulation and shape of water drops falling at terminal velocity in air.” *Quarterly Journal of the Royal Meteorological Society* 96, no. 408 (1970): 247-256.

[155] H. R. Pruppacher, R. L. Pitter. “A semi-empirical determination of the shape of cloud and rain drops.” *Journal of the Atmospheric Sciences* 28, no. 1 (1971): 86-94.

[156] J. S. Marshall, W. M. K. Palmer. “The distribution of raindrops with size.” *Journal of meteorology* 5, no. 4 (1948): 165-166.

[157] G. Feingold, Z. Levin. “The lognormal fit to raindrop spectra from frontal convective clouds in Israel.” *Journal of Climate and Applied Meteorology* 25, no. 10 (1986): 1346-1363.

[158] C. W. Ulbrich. “Natural variations in the analytical form of the raindrop size distribution.” *Journal of Climate and Applied Meteorology* 22, no. 10 (1983): 1764-1775.

[159] J. Testud, S. Oury, R. A. Black, *et al*. “The concept of “normalized” distribution to describe raindrop spectra: A tool for cloud physics and cloud remote sensing.” *Journal of Applied Meteorology* 40, no. 6 (2001): 1118-1140.

[160] J. O. Laws, D. A. Parsons. “The relation of raindrop‐size to intensity.” *Transactions American Geophysical Union* 24, no. 2 (1943): 452-460.

[161] J. Joss, J. C. Thams, A. Waldvogel. “The variation of rain drop size distribution at Locarno.” *Bulletin of the American Meteorological Society* 49, no. 5 (1968): 2.

[162] I. V. Litovinov. “On the distribution function of particles of rainfall.” *Izvestia AN SSSR, Geophysical Series* 6 (1957): 838-839.

[163] I. V. Litovinov. “Size distribution of raindrops from melting hail.” *Izvestia, Geophysical Series* 6 (1958): 903-912.

[164] N. P. Krasyuk, V. I. Rozenberg, D. A. Chistyakov. “Attenuation and scattering of radar signals by radio with shifrin and Marshall-Palmer drop sze distributions.” *Radio Engineering and Electronic Physics* 13, no. 10 (1968): 1638-1640.

[165] R. W. Rice, P. A. Peebles. Investigation of radar rain clutter cancellation using a polarization method. Tennessee University Knoxville Department of Electrical Engineering, 1975.

[166] P. T. Willis. “Functional fits to some observed drop size distributions and parameterization of rain.” *Journal of the Atmospheric Sciences* 41, no. 9 (1984): 1648-1661.

[167] M. Montopoli, F. S. Marzano, G. Vulpiani. “Analysis and synthesis of raindrop size distribution time series from disdrometer data.” *IEEE Transactions on Geoscience and Remote Sensing* 46, no. 2 (2008): 466-478.

[168] E. A. Baltas, M. A. Mimikou. “The use of the Joss-type disdrometer for the derivation of Z-R relationships.” *Proceedings of ERAD* (2002).

[169] D. Atlas, C. W. Ulbrich. “Path-and area-integrated rainfall measurement by microwave attenuation in the 1-3 cm band.” *Journal of Applied Meteorology* 16, no. 12 (1977): 1322-1331.

[170] ITU-R: Specific attenuation model for rain for use in prediction methods. Rec. P.838, ITU-R, 1999.

[171] S. Okamura, T. Oguchi. “Electromagnetic wave propagation in rain and polarization effects.” *Proceedings of the Japan Academy. Series B, Physical and biological sciences* 86, no. 6 (2010): 539.

[172] T. Oguchi. “Electromagnetic wave propagation and scattering in rain and other hydrometeors.” *Proceedings of the IEEE* 71, no. 9 (1983): 1029-1078.

[173] K. Aydin, Y. Lure. “Millimeter wave scattering and propagation in rain: A computational study at 94 and 140 GHz for oblate spheroidal and spherical raindrops.” *IEEE Transactions on Geoscience and Remote Sensing* 29, no. 4 (1991): 593-601.

[174] P. W. Barber, S. C. Hill. Light scattering by particles: computational methods. world scientific publishing, Singapore, 1990.

[175] Z. Jia, Q. Zhu, F. Ao. "Atmospheric attenuation analysis in the FSO link." *International Conference on Communication Technology* (2006).

[176] G. Mie. "Contributions to the optics of turbid media, especially colloidal metal solutions." *Annals of Physics* 330, No 3 (1908): 377-445.

[177] A. Ishimaru. Electromagnetic wave propagation, radiation, and scattering. Englewood Cliffs, NJ: Prentice Hall, 1991.

[178] F. T. Ulaby. Microwave radar and radiometric remote sensing. University of Michigan Press, 2014.

[179] C. Matzler. Thermal microwave radiation: applications for remote sensing. stevenge, UK: Institute of Engineering and Technology. 2006

[180] T. Mizuochi. "Recent progress in forward error correction and its interplay with transmission impairments." *IEEE Journal of Selected Topics in Quantum Electronics* 12, no. 4 (2006): 544-554.

[181] K. Su, L. Moeller, R. B. Barat, *et al.* "Experimental comparison of terahertz and infrared data signal attenuation in dust clouds." *Journal of the Optical Society of America A* 29, no. 11 (2012): 2360-2366.

[182] N. Perlot. "Evaluation of the scintillation loss for optical communication systems with direct detection." *Optical Engineering* 46, no. 2 (2007): 025003-025003.

[183] W. O. Popoola, Z. Ghassemlooy. "BPSK subcarrier intensity modulated free-space optical communications in atmospheric turbulence." *Journal of Lightwave Technology* 27, no. 8 (2009): 967-973.

[184] J. Ma, F. Vorrius, L. Lamb, *et al*. "Comparison of experimental and theoretical determined terahertz attenuation in controlled rain." *Journal of Infrared, Millimeter, and Terahertz Waves* (2015): 1-8.

[185] S. A. Zabidi, M. R. Islam, W. Al-Khateeb, *et al*. "Analysis of rain effects on terrestrial free space optics based on data measured in tropical climate." *IIUM Engineering Journal* 12, no. 5 (2012).

[186] Y. Kado and T. Nagatsuma. "Exploring sub-THz waves for communications, imaging, and gas sensing." *PIERS Proceedings* (2009).

[187] Online: http://www.thevoltreport.com/faster-internet-is-on-for-the-2020-olympics-and-beyond/ (accessed on November 11th, 2015).

[188] M. Sekine, G. Lind. "Rain attenuation of centimeter, millimeter and submillimeter radio waves." *12th European Microwave Conference* (1982).

[189] D. Deirmendjian. “Far-infrared and submillimeter wave attenuation by clouds and rain,” Rand Corp Santa Monica CA, 1975.

[190] R. Olsen, D. V. Rogers, D. B. Hodge. “The aR^b relation in the calculation of rain attenuation.” *IEEE Transactions on Antennas and Propagation* 26, no. 2 (1978): 318-329.

[191] F. T. Ulaby, D. G. Long. Microwave radar and radiometric remote sensing. Ann Arbor, MI: University of Michigan Press, 2014.

[192] Y. Yang, M. Mandehgar, D. Grischkowsky. “Time domain measurement of the THz refractivity of water vapor.” *Optics Express* 20, no. 24 (2012): 26208-26218.

[193] I. I. Kim, M. Mitchell, E. J. Korevaar. “Measurement of scintillation for free-space laser communication at 785 nm and 1550 nm.” *International Society for Optics and Photonics* (1999).

[194] A. C. Best. “The size distribution of raindrops.” *Quarterly Journal of the Royal Meteorological Society* 76, no. 327 (1950): 16-36.

[195] T. Utsunomiya, M. Sekine. “Rain attenuation at millimeter and submillimeter wavelength.” *International Journal of Infrared and Millimeter Waves* 26, no. 6 (2005): 905-920.

[196] M. Khatib. Contemporary issues in wireless communications. Rijeka, Croatia: InTech, 2014.

[197] K. Su, L. Moeller, R. R. Barat, *et al* “Experimental comparison of terahertz and infrared data signal attenuation in dust clouds.” *Journal of the Optical Society of America A* 29, no. 11 (2012): 2360-2366.

[198] G. Ivanovs, D. Serdega. “Rain intensity influence on to microwave line payback terms.” *Elektronika ir Elektrotechnika* 70, no. 6 (2015): 60-64.

[199] C. C. Chen, “A correction for middleton's visible and infrared radiation extinction coefficients due to rain.” Interim Report RAND Corp., 1974.

[200] H. Cho, K. P. Bowman, G. R. North. “A comparison of gamma and lognormal distributions for characterizing satellite rain rates from the tropical rainfall measuring mission.” *Journal of Applied Meteorology* 43, no. 11 (2004): 1586-1597.

[201] C. Mätzler. Thermal microwave radiation: applications for remote sensing. Herts, UK: Iet, 2006.